

DISCOVERY OF THE HIGGS BOSON AND A SEARCH FOR  
BEYOND THE STANDARD MODEL PHYSICS IN ZZ  
DECAYS USING THE CMS DETECTOR AT THE LHC

*by*

Ian Ross

A dissertation submitted in partial fulfillment of  
the requirements for the degree of

Doctor of Philosophy  
(Physics)

*at the*  
UNIVERSITY OF WISCONSIN – MADISON  
2013

Defended on 8.August.2013

Dissertation approved by the following members of the Final Oral Committee:

Sridhara Dasu · Professor of Physics

Wesley Smith · Bjorn Wiik Professor of Physics

Matt Herndon · Professor of Physics

Vernon Barger · Vilas Professor of Physics

Terry Millar · Professor of Mathematics

## Abstract

A study of the  $pp \rightarrow ZZ \rightarrow \ell\ell\ell\ell$  final state is conducted using  $19.6 \text{ fb}^{-1}$  of 8 TeV proton-proton collisions at the LHC using the CMS detector. The Standard Model  $pp \rightarrow ZZ$  production cross section is measured to be  $7.7_{-0.5}^{+0.5}(\text{stat.})_{-0.5}^{+0.6}(\text{sys.}) \pm 0.3(\text{lumi}) \text{ pb}$ . Evidence of a new Higgs-like boson is observed with a significance of  $6.1\sigma$  at 126 GeV. 95% confidence level upper limits are set on the neutral anomalous triple gauge couplings;  $-0.004 < f_4^Z < 0.004$ ,  $-0.005 < f_4^\gamma < 0.005$ ,  $-0.004 < f_5^Z < 0.004$ , and  $-0.005 < f_5^\gamma < 0.005$ .

## Acknowledgements

Acknowledgement is owed to many, and I deeply apologize for those who I've left off this list (it's not intentional, I promise). Many thanks:

To Sridhara Dasu, Wesley Smith, and Matt Herndon for their endless support, knowledge, and bountiful advice.

To Sascha Savin, for his patience, help, and ideas.

To Evan Friis and Maria Cepeda, for their wisdom and friendship.

To my fellow UW CMS students, past and present, for the support (be it programming, physics, RCT, or life-related), and all the good times. Marc Weinberg, Kira Grogg, Michalis Bachtis, Christos Lazaridis, Mike Anderson, Jeff Klukas, Lindsey Gray, Jessica Leonard, Joshua Swanson, Isobel Ojalvo, Austin Belknap, and all the rest – I owe pieces of this work to each of you.

To my friends, in Madison and beyond, for always being there for me, even when I was an ocean away.

To the HZZ4L Group, whose collective efforts are reflected in my work.

And to my family: my sister, Cameron, and my parents, Doug and Judy, for their support and love. I couldn't have done it without you.

# Contents

|  |     |
|--|-----|
| Abstract . . . . .   | i   |
| Acknowledgements . . . . .                                   | ii  |
| <b>List of Figures</b>                                       | vii |
| <b>List of Tables</b>  | x   |
| <b>1 Introduction</b>  | 1   |
| <b>2 The Standard Model and Beyond</b>                       | 3   |
| 2.1 Overview . . . . .                                       | 3   |
| 2.1.1 Fundamental Particles . . . . .                        | 4   |
| 2.1.2 Fundamental Forces . . . . .                           | 5   |
| 2.1.3 Electroweak Symmetry Breaking . . . . .                | 8   |
| 2.2 Proton-proton collisions . . . . .                       | 9   |
| 2.3 Diboson Production . . . . .                             | 11  |
| 2.4 Shortcomings . . . . .                                   | 14  |
| 2.5 Physics Beyond the Standard Model . . . . .              | 15  |
| 2.5.1 Neutral Triple Gauge Couplings . . . . .               | 16  |
| <b>3 Previous Results</b>                                    | 20  |
| 3.1 Observations and properties of the $Z_0$ boson . . . . . | 20  |

|          |   |           |
|----------|---|-----------|
| 3.2      | Diboson Production . . . . .                          | 21        |
| 3.3      | Higgs Limits . . . . .                                | 22        |
| 3.4      | Higgs Searches at the Large Hadron Collider . . . . . | 22        |
| 3.5      | Searches for neutral triple gauge couplings . . . . . | 23        |
| <b>4</b> | <b>Experimental Overview of the LHC and CMS</b>       | <b>25</b> |
| 4.1      | Definitions of Terminology . . . . .                  | 26        |
| 4.2      | The Large Hadron Collider . . . . .                   | 27        |
| 4.3      | The Compact Muon Solenoid detector . . . . .          | 28        |
| 4.3.1    | Tracker . . . . .                                     | 30        |
| 4.3.2    | Electromagnetic Calorimeter . . . . .                 | 33        |
| 4.3.3    | Hadronic Calorimeter . . . . .                        | 35        |
| 4.3.4    | The Magnet . . . . .                                  | 37        |
| 4.3.5    | Muon chambers . . . . .                               | 38        |
| 4.3.6    | Data Acquisition and Trigger . . . . .                | 41        |
| 4.3.7    | L1 Trigger System . . . . .                           | 42        |
| 4.3.8    | HLT System . . . . .                                  | 44        |
| <b>5</b> | <b>Event Generation and Simulation</b>                | <b>45</b> |
| 5.1      | Monte Carlo Simulation . . . . .                      | 45        |
| 5.2      | Parton Showering . . . . .                            | 47        |
| 5.3      | Pile-up . . . . .                                     | 48        |
| 5.4      | Generator Software . . . . .                          | 49        |
| 5.5      | Samples used . . . . .                                | 49        |
| 5.6      | Detector Simulation . . . . .                         | 50        |
| <b>6</b> | <b>Event Reconstruction</b>                           | <b>53</b> |

|          |   |           |
|----------|---|-----------|
| 6.1      | Vertex and Track Reconstruction . . . . .                   | 53        |
| 6.2      | Electron Reconstruction . . . . .                           | 54        |
| 6.3      | Muon Reconstruction . . . . .                               | 56        |
| 6.4      | Particle Flow . . . . .                                     | 57        |
| <b>7</b> | <b>Analysis Strategy</b>                                    | <b>58</b> |
| 7.1      | Online Selection . . . . .                                  | 58        |
| 7.2      | Lepton Definitions . . . . .                                | 60        |
| 7.2.1    | Isolation . . . . .   | 60        |
| 7.2.2    | Impact Parameter Requirements . . . . .                     | 61        |
| 7.2.3    | Electrons . . . . .   | 62        |
| 7.2.4    | Muons . . . . .   | 65        |
| 7.2.5    | Scale factors . . . . .                                     | 66        |
| 7.3      | Pile-up Reweighting . . . . .                               | 67        |
| 7.4      | Background Estimation . . . . .                             | 69        |
| 7.5      | Final State Radiation Recovery . . . . .                    | 74        |
| 7.6      | Kinematic Discriminant . . . . .                            | 77        |
| 7.7      | Final event selection . . . . .                             | 79        |
| 7.7.1    | Candidate combinatorics and arbitration . . . . .           | 80        |
| 7.7.2    | Signal selection . . . . .                                  | 80        |
| 7.8      | Signal and background modelling . . . . .                   | 81        |
| 7.9      | Systematic Uncertainties . . . . .                          | 83        |
| 7.9.1    | Higgs Signal Simulation . . . . .                           | 83        |
| 7.9.2    | ZZ Simulation . . . . .                                     | 85        |
| 7.9.3    | Systematic Uncertainties on Reducible Backgrounds . . . . . | 86        |
| 7.9.4    | Global Uncertainties in MC-driven estimates . . . . .       | 86        |

|                     |  |            |
|---------------------|--|------------|
| 7.10                | Summary                                    | 86         |
| <b>8</b>            | <b>Results</b>                             | <b>88</b>  |
| 8.1                 | Standard Model ZZ Production               | 88         |
| 8.1.1               | Cross section measurement                  | 90         |
| 8.1.2               | Unfolding                                  | 91         |
| 8.2                 | Search for a Standard Model Higgs Boson    | 99         |
| 8.2.1               | Statistical Analysis                       | 99         |
| 8.3                 | Limits on anomalous triple gauge couplings | 103        |
| <b>9</b>            | <b>Conclusions</b>                         | <b>107</b> |
| 9.1                 | Summary                                    | 107        |
| 9.2                 | Future Outlook                             | 108        |
| <b>Bibliography</b> |  | <b>109</b> |

# List of Figures

|      |   |    |
|------|---|----|
| 2.1  | A quantitative picture of the Higgs potential. . . . .                  | 9  |
| 2.2  | Standard Model ZZ production . . . . .                                  | 11 |
| 2.3  | The SM-forbidden ZZZ (or ZZ $\gamma$ coupling). . . . .                 | 11 |
| 2.4  | Higgs $\rightarrow$ ZZ production. . . . .                              | 12 |
| 2.5  | Higgs decays . . . . .  | 13 |
| 2.6  | Phenomenological effects of aTGCs on boson and lepton $p_T$ . . . . .   | 18 |
| 2.7  | Phenomenological effects of aTGCs on lepton separation. . . . .         | 19 |
| 4.1  | The LHC accelerator chain. . . . .                                      | 28 |
| 4.2  | The amount of intergraled luminosity at the LHC in 2011 and 2012. . . . | 29 |
| 4.3  | Isometric view of CMS . . . . .   | 30 |
| 4.4  | A cutaway slice of the CMS detector. . . . .                            | 30 |
| 4.5  | The geometry of the CMS tracking system. . . . .                        | 31 |
| 4.6  | The geometry of the CMS electromagnetic calorimeter. . . . .            | 34 |
| 4.7  | The geometry of the CMS hadronic calorimeter. . . . .                   | 37 |
| 4.8  | The geometry of the CMS muon system. . . . .                            | 39 |
| 4.9  | A schematic drawing of a drift tube chamber. . . . .                    | 40 |
| 4.10 | Diagram of the information flow through the CMS trigger system. . . . . | 43 |
| 5.1  | A comparison of three different PDF sets. . . . .                       | 47 |

|      |  |    |
|------|--|----|
| 5.2  | Diagrammatic representation of a hadronization process. . . . .  | 48 |
| 6.1  | Diagram of an electron and its signatures . . . . .  | 55 |
| 7.1  | Ratio of lepton efficiencies between data and monte carlo simulations for electrons and muons. . . . .                             | 68 |
| 7.2  | The effects of pile-up corrections on the rectonstructed vertex distribution. . . . .  | 69 |
| 7.3  | Leptonic fake rates used for the background estimation. . . . .  | 71 |
| 7.4  | Background estimation region consisting of a $Z_0$ plus two failed leptons. .  | 72 |
| 7.5  | Background estimation region consisting of a $Z_0$ plus one passed and one failed leptons. . . . .                                 | 73 |
| 7.6  | Background estimation region consisting of a $Z_0$ plus two failed leptons, with the high mass requirement. . . . .                | 74 |
| 7.7  | Background estimation region consisting of a $Z_0$ plus one passed and one failed leptons, with the high mass requirement. . . . . | 75 |
| 7.8  | Diagram depicting the flow of events in the reducible background estimate. .   | 76 |
| 7.9  | A simulated $H \rightarrow 2e2\mu$ ( $m_H = 125GeV$ ) peak, with and without FSR recovery. . . . .                                 | 78 |
| 7.10 | The angular definitions in the ZZ rest frame. . . . .  | 79 |
| 7.11 | Final selection efficiency, as a function of Higgs mass. . . . .   | 82 |
| 8.1  | ZZ invariant mass for the high-mass analysis, across the full considered $M_{\ell\ell\ell\ell}$ range. . . . .                     | 89 |
| 8.2  | Example response matrices used in unfolding. . . . .   | 93 |
| 8.3  | An example of the effects of unfolding. . . . .  | 94 |
| 8.4  | Unfolded distribution of the highest $p_T$ lepton. . . . .   | 95 |
| 8.5  | Unfolded ZZ kinematic variables. . . . .   | 96 |
| 8.6  | Unfolded leading (in $p_T$ ) Z kinematic variables. . . . .  | 97 |

|      |   |     |
|------|---|-----|
| 8.7  | Unfolded distribution of the Z candidate separation. . . . .  | 98  |
| 8.8  | ZZ invariant mass for the low-mass analysis, across the full considered<br>$M_{\ell\ell\ell\ell}$ range. . . . .                    | 100 |
| 8.9  | ZZ invariant mass including the low-mass $ZZ^*$ analysis, zoomed to take<br>a closer look at the excess. . . . .                    | 101 |
| 8.10 | 95% CL Upper Limits on Standard Model Higgs production. . . . .   | 102 |
| 8.11 | p-value scan. . . . .   | 102 |
| 8.12 | Qualitative likelihood scan of the $(f_4^Z, f_4^\gamma)$ coupling space, with a signal<br>injected. . . . .                         | 104 |
| 8.13 | Comparison of the $M_{\ell\ell\ell\ell}$ for Standard Model ZZ production by the LO<br>generator SHERPA and the NLO POWHEG. . . . . | 105 |
| 8.14 | 2D limits on the neutral anomalous triple gauge couplings. . . . .  | 106 |

# List of Tables

|     |  |    |
|-----|--|----|
| 2.1 | Fermions and their properties.   | 5  |
| 2.2 | Bosons and their properties.   | 5  |
| 2.3 | Higgs production cross sections at the LHC.  | 12 |
| 2.4 | ZZ Production cross sections at the LHC.   | 14 |
| 2.5 | Breakdown of decay modes for the $Z_0$ boson.  | 14 |
| 3.1 | Summary of existing 95% C.L for neutral aTGCs.   | 24 |
| 4.1 | Machine specifications for the LHC.  | 28 |
| 5.1 | Summary of Monte Carlo samples used.   | 51 |
| 7.1 | The L1 seeds and HLT triggers used in each final state.  | 59 |
| 7.2 | List of electron variables used in the electron idendification MVA.  | 63 |
| 7.3 | The electron identification criteria.  | 64 |
| 7.4 | Loose lepton definitions.  | 70 |
| 7.5 | Summary of the selection criteria.   | 87 |
| 7.6 | Summary of the systematic uncertainties.   | 87 |
| 8.1 | Final yields per event channel in the high-mass analysis (ZZ Production cross-section and anomalous triple gauge coupling search). | 89 |

|  |     |
|--|-----|
| 8.2 ZZ production cross section measurements for each of the final states considered and combined. . . . . | 91  |
| 8.3 Final yields per event channel in the low-mass analysis (search for the Higgs boson). . . . .          | 99  |
| 8.4 1D limits on the neutral anomalous triple gauge couplings. . . . .                                     | 105 |

# Chapter 1

## Introduction

The theoretical model of particle physics today, known as the Standard Model, is constructed to describe three fundamental forces between two classes of particles. Despite the wide success of this theory, it is, at best, an incomplete picture of the universe. Some of the largest scientific experiments ever have been conducted with two goals in mind: to fill in the lingering unknown pieces of the Standard Model and to explore for new physical phenomena.

This thesis describes the discovery of the Higgs boson, a long-missing piece of the Standard Model, and a search for physics beyond the scope of the Standard Model. These searches were conducted using the Compact Muon Solenoid (CMS) detector at the Large Hadron Collider (LHC), an enormous proton accelerator beneath the French-Swiss border. The LHC is the highest-energy particle accelerator ever built, allowing particle interactions to be probed at an unrivaled scale.

We will begin with an overview of the Standard Model in Chapter 2, exploring the history of the theory, a general overview of its foundations, and its shortcomings. Special attention is paid to the electroweak symmetry breaking process known as the Higgs mechanism, due to its relevance to this thesis and the field as it stands today.

The state of the Standard Model, Higgs physics, and physics beyond the Standard Model is discussed in Chapter 3.

We then move to the Large Hadron Collider and the Compact Muon Solenoid. Both are described in detail in chapter 4. Then the process of event generation and simulation is described in chapter 5.

The journey from detector basics to fully reconstructed and selected event is chronicled in chapters 6 and 7, detailing the way that the detector components combine to deliver the fundamental physics objects (chapter 6, and how these objects are utilized within an analysis flow (chapter 7). Also described in this chapter are the methods for estimating the relevant physics processes which act as background over the processes of interest, estimates of systematic errors, and statistical treatment of the observations.

Finally, results are presented in chapter 8. Results for a Higgs boson-like particle are presented, along with the measurement of ZZ production. Limits are placed on the values of anomalous neutral triple gauge coupling. These results are summarized in chapter 9 before taking a quick glimpse at the results' place in the physics of today and the near future.

# Chapter 2

## The Standard Model and Beyond

The Standard Model, the theoretical framework which describes fundamental particles and their interactions, has a history rooted in the early-to-mid twentieth century. At its core are two basic groups of particles, *fermions* and *bosons*, along with three fundamental forces governing their interactions. Throughout its growth over the last eighty years (as outlined in 2.1), the Standard Model has proven to be an incredibly successful theory, with measurements validating its predictions to a phenomenal accuracy. Despite its unprecedented level of success, the Standard Model presents an incomplete description of the universe, as described in 2.4, and the search continues for physics that falls outside of the realm of this theory (2.5).

### 2.1 Overview

The Standard Model unifies the most basic physical interactions into one overarching framework. The concept of such a unification can be traced back to Einstein and beyond, but it is only in the last sixty years that the effort has really taken shape.

### 2.1.1 Fundamental Particles

There are two types of fundamental particles, *fermions* and *bosons*. Ordinary matter is made up of *fermions*, which carry half-integer spin. Fermions can be further split into two sub-classes: quarks and leptons. Quarks are then classified into three generations of doublets, each generation consisting of an “up-type” quark with charge  $+2/3$  and a “down-type” quark with charge  $-1/3$ . Quarks are never observed ‘alone’ in nature, due to the laws of quantum chromodynamics, as explained in 2.1.2. Quarks are susceptible to all three of the fundamental forces included in the Standard Model – the strong, weak, and electromagnetic forces. Via the strong force, quarks form composite color-neutral particles known as *hadrons*, either in pairs (forming mesons), or in triplets (forming baryons). Protons and neutrons are the most familiar particle in the hadron family and are composed of two up-quarks and a down quark or two down-quarks and an up-quark respectively.

Leptons, the other type of fermion, differ in the fact that leptons carry no color charge. As a result, they do not participate in any strong interactions. However, they do participate in both electromagnetic (if charged) and weak interactions. Like quarks, the lepton family is split into three generations, consisting of the generational type (electron, muon, or tau –  $e^\pm$ ,  $\mu^\pm$ , or  $\tau^\pm$ ) plus the doublet partner neutrino.

Integer- (or zero-) spin particles known as *bosons* are the particles which act as force-carriers, as described in 2.1.2. The most common of these, the photon, is a massless spin-0 particle responsible for governing the electromagnetic interactions between charged particles. The  $W^\pm$  and  $Z_0$  bosons carry the weak force and have charges of  $\pm 1$  and  $0$  respectively. The bosons are summarized in Table 2.2. Gluons, the carriers of the strong force, are, like photons, electrically neutral and massless. Unlike the other force-carriers, however, the gluon carries a unit of color and anti-color, meaning that it is able to self-interact. The implications of this property are

| Generation 1 |                           |                |                |                               |
|--------------|---------------------------|----------------|----------------|-------------------------------|
| Particle     | Mass (eV/c <sup>2</sup> ) | Charge         | T <sup>3</sup> | Forces                        |
| $e^\pm$      | $5.11 \times 10^5$        | $\pm 1$        | $+\frac{1}{2}$ | Electromagnetic, weak         |
| $\nu_e$      | $< 2.2$                   | 0              | $-\frac{1}{2}$ | Weak                          |
| u            | $2.3 \times 10^6$         | $+\frac{2}{3}$ | $+\frac{1}{2}$ | Electromagnetic, weak, strong |
| d            | $4.8 \times 10^6$         | $-\frac{1}{3}$ | $-\frac{1}{2}$ | Electromagnetic, weak, strong |
| Generation 2 |                           |                |                |                               |
| Particle     | Mass (eV/c <sup>2</sup> ) | Charge         | T <sup>3</sup> | Forces                        |
| $\mu^\pm$    | $1.05 \times 10^8$        | $\pm 1$        | $+\frac{1}{2}$ | Electromagnetic, weak         |
| $\nu_\mu$    | $< 1.70 \times 10^5$      | 0              | $-\frac{1}{2}$ | Weak                          |
| c            | $1.3 \times 10^9$         | $+\frac{2}{3}$ | $+\frac{1}{2}$ | Electromagnetic, weak, strong |
| s            | $9.5 \times 10^7$         | $-\frac{1}{3}$ | $-\frac{1}{2}$ | Electromagnetic, weak, strong |
| Generation 3 |                           |                |                |                               |
| Particle     | Mass (eV/c <sup>2</sup> ) | Charge         | T <sup>3</sup> | Forces                        |
| $\tau^\pm$   | $1.77 \times 10^9$        | $\pm 1$        | $+\frac{1}{2}$ | Electromagnetic, weak         |
| $\nu_\tau$   | $< 1.55 \times 10^7$      | 0              | $-\frac{1}{2}$ | Weak                          |
| t            | $1.74 \times 10^{11}$     | $+\frac{2}{3}$ | $+\frac{1}{2}$ | Electromagnetic, weak, strong |
| b            | $4.2 \times 10^9$         | $-\frac{1}{3}$ | $-\frac{1}{2}$ | Electromagnetic, weak, strong |

**Table 2.1:** A summary of the generations of fermions and their mass, charge, weak isospin ( $T^3$ ) and the forces which act on them. Nota bene: all right-handed particles have weak 0 isospin ( $T^3 = 0$ ).

discussed in 2.1.2

| Bosons     |                           |         |                |                 |
|------------|---------------------------|---------|----------------|-----------------|
| Particle   | Mass (eV/c <sup>2</sup> ) | Charge  | T <sup>3</sup> | Forces          |
| $Z_0$      | $91.2 \times 10^9$        | 0       | 0              | Weak            |
| $W^\pm$    | $80.4 \times 10^9$        | $\pm 1$ | $\pm 1$        | Weak            |
| $\gamma_0$ | 0                         | 0       | 0              | Electromagnetic |
| g          | 0                         | 0       | 0              | Strong          |

**Table 2.2:** A list of the force-carrying bosons, their mass, charge, weak isospin, and the force that they mediate.

## 2.1.2 Fundamental Forces

The concept that interactions between fundamental particles can be attributed to mathematical constructs called fields extends to Maxwell's formalism of electromag-

netism, but it was Feynman, Tomanaga, and Schwinger who first extended this formalism to the quantum world. In his theory of quantum electrodynamics (QED, [1]), he successfully described the electromagnetic interactions between charged particles as an exchange of massless particles called photons.

The weak force, carried by  $W^\pm$  and  $Z_0$  bosons, is responsible for those interactions between fermions that involve charge and flavor changing (such as a nucleus undergoing  $\beta^-$  decay through the  $W^-$ -mediated decay

$$d \rightarrow u + e^- + \bar{\nu}_e$$

Both the weak and electromagnetic forces have interactions which are governed by probability amplitudes of the form:

$$\frac{g^4}{(q^2 c^2 - m^2 c^4)^2}$$

where  $g$  is the force's coupling constant,  $q$  the momentum transfer of the interaction, and  $m$  the mediating boson's mass. At higher energies (of the order of  $\sim 100$  GeV, where the mass of the force-carrying bosons is dwarfed by the momenta of the particles), the form of the two forces become identical (and their relative strengths approach equality), suggesting a unification should be possible between the two.

Sheldon Glashow, Abdus Salam, and Steven Weinberg [2] provided a mathematical basis to this idea, restructuring the forces into an  $SU(2)_L \times U(1)_Y$  algebra. Within this algebraic structure, the  $SU(2)$  operations act only upon the fermions with left-handed *chirality*, while the  $U(1)$  operations act on those particles which carry hypercharge,  $Y$ . This quantum number relates to the electrical charge,  $Q$ , and  $T^3$  isospin component through the relation

$$Y = 2(Q - T^3)$$

This  $SU(2)_L \times U(1)_Y$  algebra describes four physical fields: three vector fields  $W_\mu$  which couple to the weak isospin current (with strength  $g$ ) and one vector field,

$B_\mu$  which couples to the weak hypercharge current with strength proportional to  $g'$ . Superposed, these fields describe the physical bosons:

$$W_\mu^\pm = \sqrt{\frac{1}{2}} (W_\mu^1 \mp i W_\mu^2) \quad (2.1)$$

$$Z_\mu = -B_\mu \sin \theta_W + W_\mu^3 \cos \theta_W \quad (2.2)$$

$$A_\mu = B_\mu \cos \theta_W + W_\mu^3 \sin \theta_W \quad (2.3)$$

Where 2.1 describes the weak charged current-carrying  $W^\pm$ , 2.2 describes the weak neutral current-carrying  $Z_0$ , and 2.3 describes the electromagnetic force-carrying photon.  $\theta_W$ , known as the Weinberg angle, carries information about the relative coupling strengths in the form

$$\tan \theta_W = g'/g \quad (2.4)$$

The third fundamental force, the strong force, describes the interactions between *quarks* and *gluons*. These are the fundamental particles (further described in 2.1.1) which make up nuclear matter. The theory of these interactions, known as quantum chromodynamics, was formulated in the 1960s.

Because of the gluons' ability to interact with itself, the strong force is unique in a number of respects. Most notably, the strong force grows stronger as separation distance between color-charged particles increases. When a quark sufficiently separates from another, the resulting energy is enough for other quark-antiquark pairs to pop into existence from the vacuum. The original quark then combines with these particles. This process, called hadronization, is driven by *asymptotic freedom* and restricts quarks from being observed in an unbound state in nature.

In the algebraic formulation of the Standard Model, the strong force is represented by a  $SU(3)_C$  algebra, where C is indicative of the three color charges (red, green, and blue). In any strong interaction, color must be conserved, either through adding color

and anticolor or one each of the red- blue- and green- type particles (or anti-red, anti-blue, and anti-green-).

### 2.1.3 Electroweak Symmetry Breaking

The natural question, giving the unification between the electromagnetic and weak forces at higher energies is: what causes the two to separate into distinct forces at lower energies? It is clear that the difference is in the masses of the force-carrying bosons, but there must be some physical process which gives rise to the masses of the  $W^\pm$  and  $Z_0$  bosons, breaking the symmetries apparent in the unified electroweak structure.

The mechanism for this symmetry breaking was proposed independently by Higgs [3], Englert and Brout [4], and Guralnik, Hagen, and Kibble [5]. The mechanism adds a Higgs doublet to the electroweak model

$$\phi \equiv \begin{pmatrix} \phi^+ \\ \phi^0 \end{pmatrix}$$

Adding to the potential terms of the form

$$V(\phi) = \mu^2 \phi^\dagger \phi + \frac{\lambda^2}{2} (\phi^\dagger \phi)^2$$

For  $\mu^2 < 0$ , this potential produces a degenerate set of minimal values (see a quantitative picture in Figure 2.1) and gives the Higgs field  $\phi$  a non-zero vacuum expectation value. This non-zero vacuum expectation value results in mass terms in the Lagrangian corresponding to the  $W^\pm$  and  $Z_0$  boson.

Although this mechanism neatly explains how mass arises in certain aspects of the electroweak structure, it is only very recently that a particle resembling the Higgs boson has been observed ([6], [7]), and it has yet to be conclusively shown whether the observed boson is the Standard Model Higgs or if it is a Standard Model-like

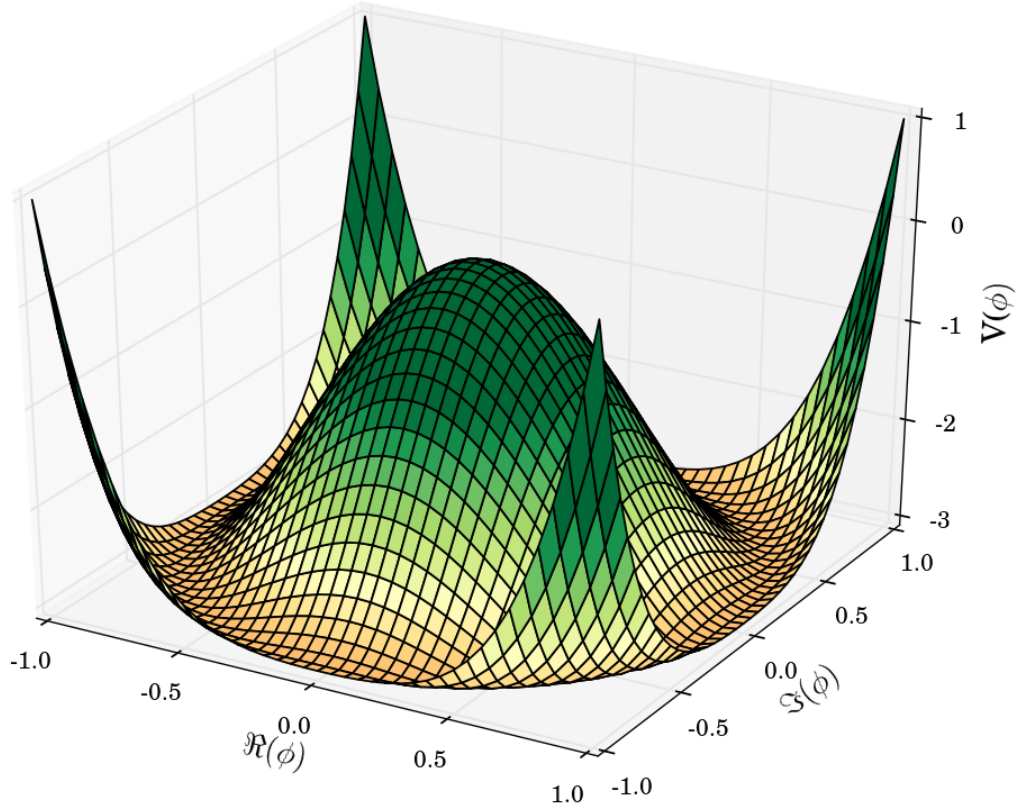


**Figure 2.1:** A quantitative picture of the Higgs potential, with a ring of degenerate minima.

piece of another model. And, as explained in 2.4 there are certain aspects of the Higgs mechanism that are left wanting.

## 2.2 Proton-proton collisions

The Large Hadron Collider (LHC) was built with the Higgs boson in mind. The compositeness of the proton imparts the collisions with in non-trivial physical ways. The *uud* quark structure of the proton does not accurately describe the way that the protons interact, as these *valence* quarks are not the objects that dictate the

interactions. As the protons involved in the collisions get higher and higher in energy, a larger fraction of the protons' momenta is tied up in the so-called *sea quarks*. These quarks, which can be of any generation, arise spontaneously as  $q\bar{q}$  pairs pop into existence from gluons exchanged between the valence quarks. As a result, the LHC has a rich field of possible initial states;  $qq$ ,  $q\bar{q}$ ,  $qg$ , and  $gg$  processes are all possible in the proton-proton collisions.

Within the Standard Model, the final products in these interactions are governed by the physical laws of the electroweak and QCD theories. The probability of a given process occurring is typically expressed in terms of a *cross section*. The cross section,  $\sigma$ , is expressed in units of area<sup>1</sup> and can be calculated within the Standard Model (or another relevant quantum field theory).

These calculations, while often non-trivial, have been conducted for years and have a well-established methodology. The most general form for a cross section calculation at the LHC is:

$$\sigma(pp \rightarrow P + X) = \frac{1}{3} \sum_{q,q'} \int dx_1 dx_2 f_1(x_1, Q^2) f_2(x_2, Q^2) \sigma_P(\hat{s}, \hat{t}, \hat{u}), \quad (2.5)$$

where  $f_1$  and  $f_2$  are parton distribution functions and  $\sigma_P$  is the parton-level cross section arising from the matrix element for the process of interest,  $P$ . These matrix elements are themselves calculated based on the rules of the theory (specifically EWK in this analysis). The production cross section of a physical process is heavily dependent upon the forces, particles, and energies involved. In general, at the energies probed at the LHC, particles arising via QCD interactions are the most common (due to the high value of  $\alpha_s$ , the size of the strong force coupling).

The cross section provides an easy way to predict the relative rate of physical

---

<sup>1</sup>The standard in particle physics is the *barn*, defined as  $1 \text{ barn} = 10^{-24} \text{ cm}^2$

processes:

$$\text{rate} = \frac{dN}{dt} = \sigma \cdot \mathcal{L} \quad (2.6)$$

Where  $N$  is the number of events produced and  $\mathcal{L}$  is the *instantaneous luminosity* of the proton beam collisions, explained further in Section 4.2.

## 2.3 Diboson Production

Within the Standard Model, a pair of  $Z$  bosons can be produced at the LHC either through quark-antiquark interactions or through gluon interactions (involving a quark loop) 2.2. Because the standard model prohibits  $ZZZ$  (or  $ZZ\gamma$ ) vertices, there is no s-channel contribution to the  $ZZ$  production process of the type diagrammed in 2.3. The quark-antiquark production mode is the dominant contribution, with the gluon-gluon mode representing roughly 10% of the overall cross section [8].

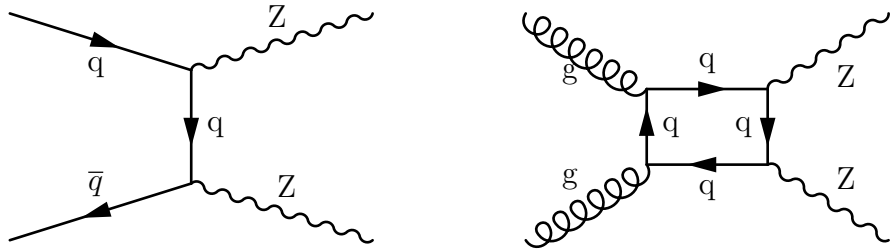


**Figure 2.2:** Production of a  $ZZ$  diboson system in the LHC, through  $qq$  (left) and  $gg$  production (right)

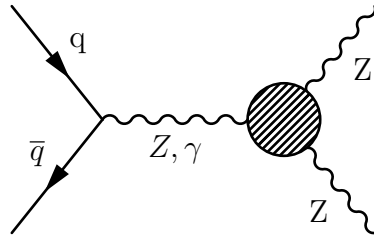


**Figure 2.3:** The SM-forbidden neutral triple vertex.

Additionally, a pair of Z bosons may be produced as the decay product of a Higgs boson. The Higgs boson can be produced in a number of ways, but the dominant methods are through gluon-gluon fusion and vector boson fusion (colloquially called the gg and VBF production mechanisms). Additionally, it may be produced in association with a vector boson (with final state VH) or through  $t\bar{t}$  fusion. Because the branching ratio of the final states considered in this thesis are so small, the contributions from these two mechanisms are considered negligible. Of the two sizable production modes, the  $gg$  production is the dominant mode at the LHC, due to the energies and properties of the protons involved. The dominant Higgs production mechanisms (with decays to a ZZ pair) is shown in Figure 2.4, with cross sections defined in Table 2.3.

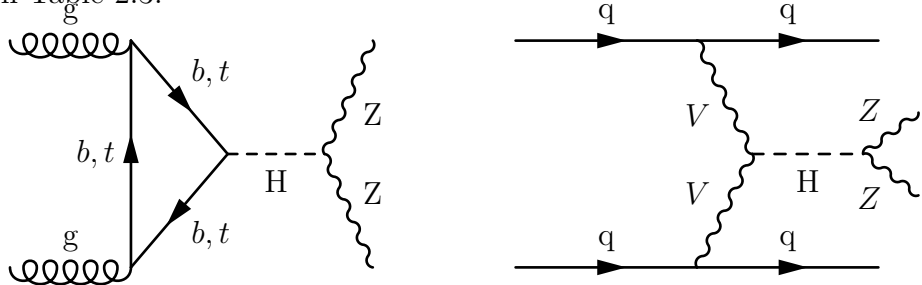


**Figure 2.4:** The production mechanism of a ZZ system, from a Higgs boson. The  $gg$  (vector boson) fusion is depicted on the left (right).

| Production Mode    | $\sigma_{8 \text{ TeV}} (\text{pb})$ | $\sigma_{7 \text{ TeV}} (\text{pb})$ |
|--------------------|--------------------------------------|--------------------------------------|
| $gg \rightarrow H$ | 19.22                                | 15.08                                |
| VBF                | 1.568                                | 1.211                                |
| WH                 | 0.6782                               | 0.5576                               |
| ZH                 | 0.3843                               | 0.3077                               |
| $t\bar{t}$         | 0.1271                               | 0.0843                               |

**Table 2.3:** Higgs boson production cross sections at 7 and 8 TeV for a mass of 126 GeV.

The Higgs boson has well-defined decay characteristics within the Standard Model (Fig. 2.5). At the mass of the observed Higgs-like boson ( $\sim 126$  GeV), the leading

decay mode is to a  $b\bar{b}$  pair, accounting for approximately 56% of Higgs decays. ZZ decays represent less than 3% of total Higgs decays, and only 1% of those decay into four leptons. However, given the high resolution with which the electrons and muons can be reconstructed and the unmatchably clean signature of four leptons, the  $H \rightarrow ZZ \rightarrow \ell\ell\ell'\ell'$  represents a critical channel in Higgs searches.

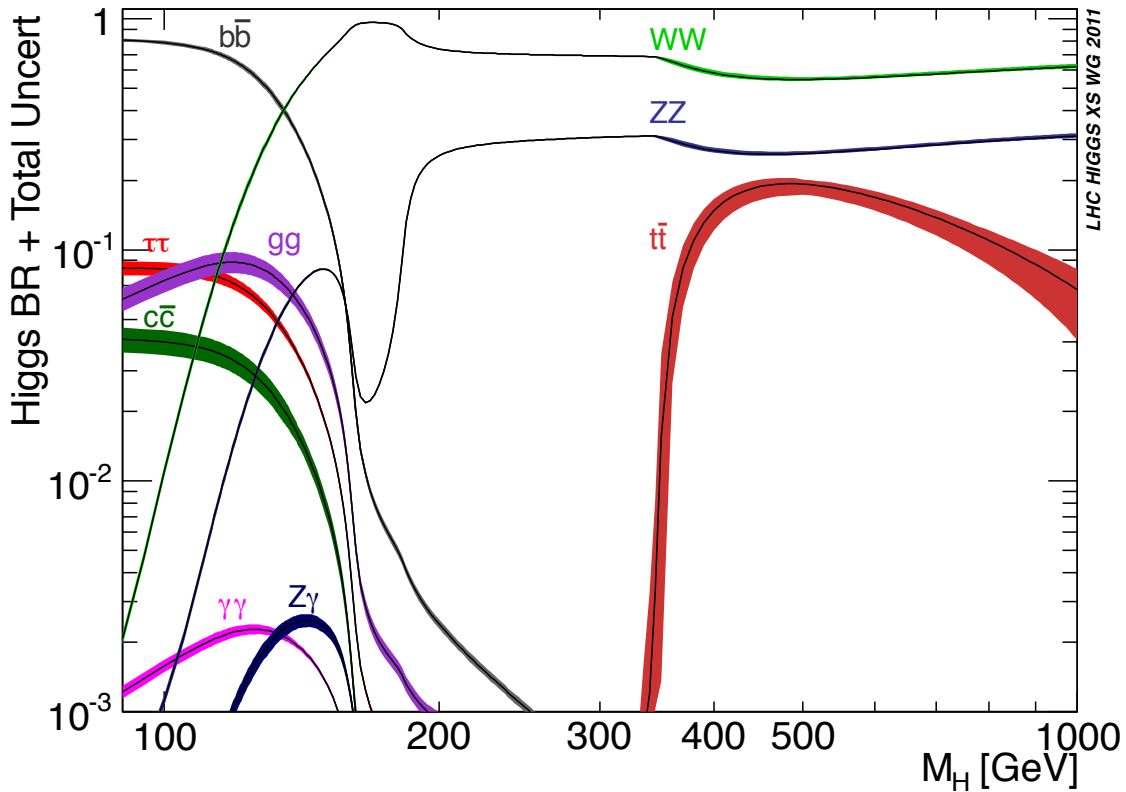


**Figure 2.5:** Higgs decays

The cross sections for each of these ZZ production mechanisms is displayed in Table 2.4

$Z_0$  bosons are unstable particles and decay into fermion-antifermion pairs. The majority of these decays are into quarks which immediately decay hadronically. The next leading Z decay is the decay mode to neutrino pairs, which escape the detector

| Production Mode                             | $\sigma_{8 \text{ TeV}} (\text{pb})$ | $\sigma_{7 \text{ TeV}} (\text{pb})$ |
|---|--------------------------------------|--------------------------------------|
| $qq \rightarrow ZZ + gg \rightarrow ZZ$     | 7.92                                 | 6.46                                 |
| $H(125 \text{ GeV}) \rightarrow ZZ$ (total) | 0.637                                | 0.500                                |

**Table 2.4:** ZZ Production cross sections at 7 and 8 TeV. The Higgs production mechanism includes all contributions (including associated production and  $t\bar{t}$  fusion).

without interaction. The third, and most relevant within the context of this thesis, are the decays into lepton pairs. These decays represent roughly 10% of all Z decays, as demonstrated in Table 2.5.

| Decay Mode     | Fraction (%)      |
|----------------|-------------------|
| $e^+e^-$       | $3.363 \pm 0.004$ |
| $\mu^+\mu^-$   | $3.366 \pm 0.007$ |
| $\tau^+\tau^-$ | $3.370 \pm 0.008$ |
| Invisible      | $20.0 \pm 0.06$   |
| Hadrons        | $69.91 \pm 0.06$  |

**Table 2.5:** The branching ratios of the most common decay modes of the  $Z_0$  boson. Roughly 10% of all created  $Z_0$  bosons decay leptonically, which is the mode of interest in this thesis.

## 2.4 Shortcomings

Despite its great successes, the Standard Model is known to be at best an incomplete theory. Pieces of the theory carry a conspicuously ad-hoc nature, as the physical constants left floating must be adjusted in a fine balance in order to cancel divergences in the theory. Similarly, the mechanism of electroweak symmetry breaking has a non-zero vacuum expectation value only if the  $\mu^2$  parameter is negative, which has no physical motivation.

The Standard Model also falls short at being a perfectly unified theory, as it has little to say about the fourth fundamental force: gravity. Attempts to unify the Standard Model as it stands today with gravitational forces prove incredibly difficult,

as the scale of the gravitational force is many orders of magnitude smaller than the others, even at the high energy scales of unification.

Experimental evidence is mounting ( [9–11]) which indicates that neutrinos have mass, while the Standard Model in its form presented here contains massless neutrinos.

The Standard Model, to some extent, seems to provide tension with today’s cosmological theories. It has no components explaining the cosmological phenomena *dark matter* and *dark energy*. These objects, which compose 23% and 72% of the universe’s energy content, respectively, have not been accounted for. There is also no explanation as to why the matter in the universe is composed of ‘ordinary’ matter, as opposed to antimatter. The two are suspected to have existed initially in equal mixing, though only ordinary matter is seen today.

Finally, there’s no indication of where the structures and classifications come from. Why, for example, are there three generations of leptons and quarks instead of four? Is the current mix of forces ‘final,’ or is it possible to unite all three forces into one?

## 2.5 Physics Beyond the Standard Model

Several attempts have been made to answer these some (or all) of these questions, from the extensions of Supersymmetry, technical to a fully reimagined grand unified theories, like string theory. These theories largely fall outside of the scope of this thesis, but theories which predict new particles with ZZ decays (such as those that predict a  $Z'$  boson) or neutral triple gauge couplings have ramifications explained below.

### 2.5.1 Neutral Triple Gauge Couplings

In the SM, ZZ production proceeds via the  $t$ - and  $u$ -channel  $q\bar{q}$  scattering diagrams, and via gluon-gluon fusion. The presence of anomalous neutral trilinear couplings (aTGCs)  $ZZZ$  and  $ZZ\gamma$  would lead to a sizable enhancement of ZZ final states via  $s$ -channel  $q\bar{q}$  scattering as in 2.3. A model featuring such couplings can be constructed by means of an effective Lagrangian [12]. In this parametrization, two  $ZZZ$  couplings and two  $ZZ\gamma$  couplings are allowed by electromagnetic gauge invariance and Lorentz invariance for on-shell Z bosons. The form of the vertex function may be written as:

$$\Gamma_V^{\alpha,\beta,\mu} = \frac{\hat{s} - m_V^2}{m_Z^2} \left( i f_4^V (P^\alpha g^{\mu\beta}) + i f_5^V \epsilon^{\mu\alpha\beta\rho} (q_1 - q_2)_\rho \right) \quad (2.7)$$

. The couplings are parametrized by two CP-violating ( $f_4^{Z,\gamma}$ ) and two CP-conserving ( $f_5^{Z,\gamma}$ ) complex parameters, all of which are zero at tree level in the Standard Model (as  $f_5^{Z,\gamma}$  breaks parity conservation).

In general, these couplings do not necessarily conserve partial wave unitarity at high center-of-mass energies (due to their dependence on  $\hat{s}$ ). In previous literature, the  $\hat{s}$  dependence is treated using a form factor,

$$f_i^V(\hat{s}) = \frac{f_{i0}^V}{\left(1 + \frac{\hat{s}}{\Lambda_{NP}^2}\right)^n}$$

where  $\Lambda_{NP}$  is the energy scale at which the new physics manifests itself and  $f_{i0}^V$  is the bare value of the coupling. However, the coupling values being considered ( $\sim 0.06$ ) are unitarity safe through our sensitive region ( $m_{4l} < 1.5$  TeV [13]), and, as a result, no form factor is assumed. The limits presented in this analysis can thus be interpreted as restrictions on the ‘bare’  $f_{i0}^V$  couplings.

## Observable manifestations of aTGCs

Any indications that these couplings are non-zero are an immediate signal of physics beyond the standard model. The phenomenological effects are well described by theorists (for example, [14]). The most immediate effect of anomalous couplings is an increase in the ZZ production cross section, which would result in a higher-than-anticipated number of observed events. Additionally, the coupling effects shape the kinematics of the event, becoming especially pronounced at higher energies. Within the context of this thesis, the most relevant manifestations are the broad increases in the system's invariant mass, increases in the  $Z_0$  transverse momenta, and increased lepton transverse momenta. The effects on the boson and lepton are exemplified in figure 2.6, reproduced from [14].

Because the effects of the couplings  $f_4^{Z,\gamma}$  and  $f_5^{Z,\gamma}$  enter the matrix elements identically, it is impossible to distinguish the two based solely on the effects explained above. However, it is feasible to comb out some more distinction between the various couplings given their differing impact on helicity amplitudes. Specifically, the  $f_5^{Z,\gamma}$  couplings produce terms that interfere with the helicity amplitudes produced by Standard Model couplings. Finally, if evidence of these couplings were to be found, separation between the leptons coming from a Z boson (both in the spatial separation and the azimuthal angle between them) can provide subtle clues to the type (and possibly sign) of the coupling. The effects can be seen in figure 2.7, reproduced from [14].

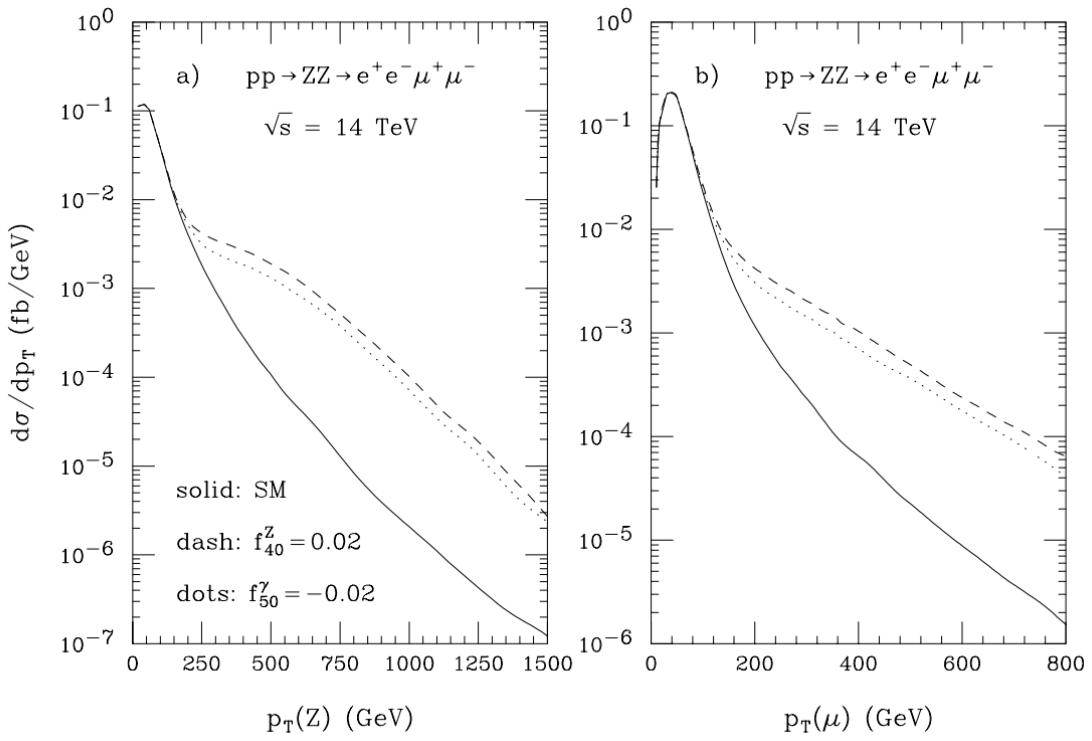


**Figure 2.6:** Phenomenological effects of aTGCs on boson and lepton  $p_T$ , reproduced from [14]. Note especially the pronounced high-energy tails produced by the anomalous couplings.

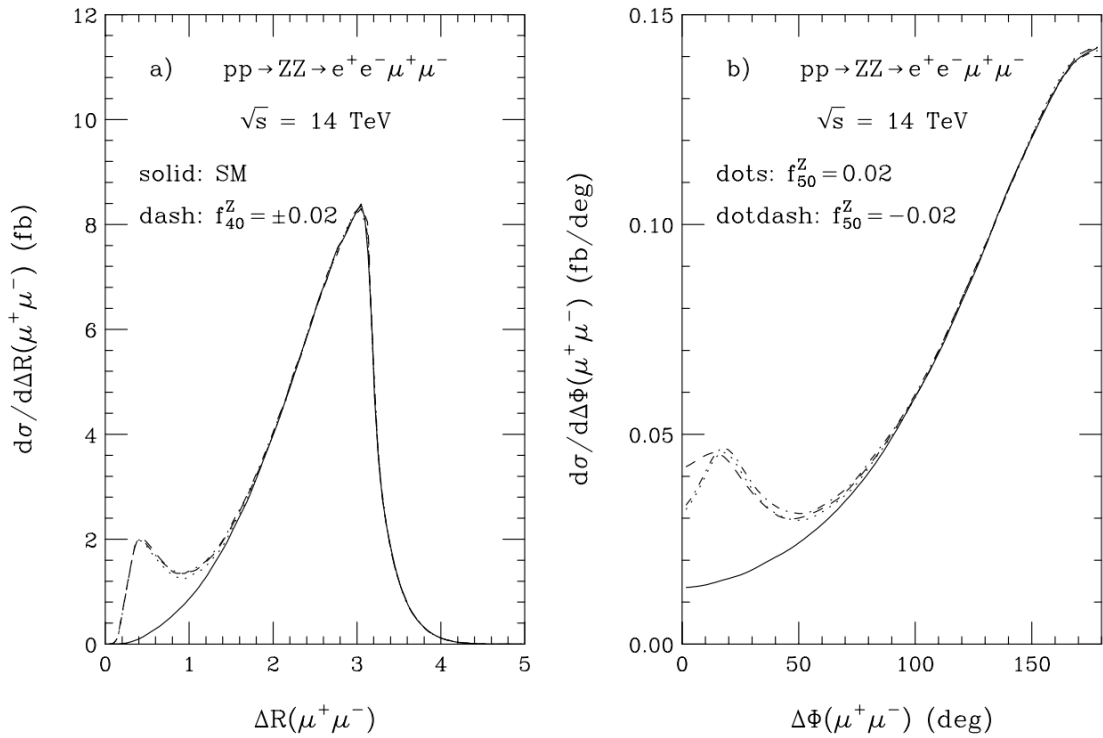


**Figure 2.7:** Phenomenological effects of aTGCs on the separation between leptons, reproduced from [14]. The type, size, and sign of the coupling create slight differences in the azimuthal angle distribution. Reproduced from [14].

# Chapter 3

## Previous Results

### 3.1 Observations and properties of the $Z_0$ boson

The first indirect experimental evidence for the  $Z_0$  boson was first observed at the Gargamelle detector at CERN [15] in 1973. The experiment consisted of passing a neutrino beam through a liquid bubble chamber and looking for evidence of neutral currents in the form of electron-neutrino scattering:

$$\bar{\nu}_\mu + e^- \rightarrow \bar{\nu}_\mu + e^-$$

$$\nu_\mu + e^- \rightarrow \nu_\mu + e^-$$

Of the 735,000 pictures analyzed, one was characteristic of a neutral current interaction, and is regarded as the first experimental evidence of the  $Z_0$  boson.

The first direct evidence of the particle came almost a full 10 years later, in 1983, at CERN's Super Proton Synchrotron (SPS). The UA1 experiment observed four events indicative of a  $Z_0 \rightarrow e^+e^-$  decay and one  $Z_0 \rightarrow \mu^+\mu^-$  event, with invariant masses consistent with the SM prediction of 91.2 GeV [16]. The UA2 experiment corroborated the discovery soon after.

Although the experiments at the SPS were able to provide the first evidence of the  $Z_0$  boson, it was not until the clean collisions recorded by the experiments at CERN’s Large Electron-Positron (LEP) collider that accurate measurements of the boson’s properties could be made in 1990. The energy of the collider, combined with the clean environment of electron-positron collisions, made the experiments at LEP a veritable factor of weak bosons. When coupled with data from the SLAC Large Detector (SLD) at the Stanford Linear Collider, the electroweak sector was fleshed out in intricate detail. Unparalleled measurements of mass, total and partial decay widths, coupling constants, and searches for new decay modes and anomalous coupling modes were conducted at the LEP and SLAC experiments. The results were superb validations of the Standard Model predictions, with mass measurement and widths measured with per-mil accuracy. [17]:

$$m_Z = 91.91875 \pm 0.0021 GeV$$

$$\Gamma_Z = 2.4952 \pm 0.0023 GeV$$

$$\sin^2\theta_W = 0.23153 \pm 0.00016$$

Experiments the Tevatron (especially during its Run II phase from 2001 to 2011) repeated these measurements within the context of 1.96 GeV  $p\bar{p}$  collisions, with cross-section and weak-mixing angles fully consistent with Standard Model expectations [18, 19]

## 3.2 Diboson Production

$ZZ$  diboson events were first observable at the LEP experiments when the  $e^+e^-$  center of mass energy exceeded the  $ZZ$  kinematic threshold. ALEPH, DELPHI, L3, and

OPAL reported  $ZZ$  production cross sections fully consistent with Standard Model Expectations [20–23].

Because the  $ZZ \rightarrow 4\ell$  final state has such a low branching ratio, previous experiments have observed a statistically limited sample of  $4\ell$  events. The latest Tevatron results include only a handful in each detector [24, 25].

### 3.3 Higgs Limits

Experiments have been keen to observe the Higgs boson since its inception in the 1950s [3–5]. While the evidence remained elusive until the summer of 2012, the regions of possible Higgs mass were constrained to ever-tighter regions of phase space.

After running from 1989-2000, the experiments at the Large Electron-Positron (LEP) at CERN combined their direct searches to set a lower bound on the Higgs Mass of 114.4 GeV [26] at 95% Confidence level (CL).

Using the combined data from the LEP, SLC, and Tevatron experiments, a combined fit to electroweak parameters was able to set an upper mass limit of 158 GeV [27].

Direct searches at the Tevatron ruled out  $100 < m_H < 103$  GeV and  $147 < m_H < 180$  GeV at the 95% confidence level, while reporting a broad access of with a  $2.9\sigma$  significance [28].

### 3.4 Higgs Searches at the Large Hadron Collider

The LHC was built with the Higgs boson in mind. As mentioned in 2.2, the proton-proton collisions provide an enhanced rate of Higgs production, with expectations of either discovering the Higgs boson at any mass, should it exist, or ruling out the

mechanism entirely.

, with capability to produce Higgs boson, if it exists, in sufficient quantity for any mass enabling a discovery or excluding the mechanism itself.

Data taken at 7 TeV collision energy in the first two years of running left only a small section of mass space for the Higgs boson. The first  $5 \text{ fb}^{-1}$  of data collected at 7 TeV allowed both the ATLAS and CMS experiments to carve out a large portion of mass exclusion. ATLAS ruled out (at 95% CL) the masses between 111.4-116.6, 119.4-122.1, and 129.2-541 GeV. CMS excluded from 127-600 GeV. By the time that the LHC was turned on again in 2012 (at 8 TeV center-of-mass energy), only masses between 122.1 and 127 GeV had not been ruled out at the 95% CL. By the middle of the summer of 2012, the experiments had gathered an additional  $5 \text{ fb}^{-1}$  at the higher energy and were able to announce, on July 4, statistically significant evidence of a new boson [?, ?]. Running through the end of 2012 produced another  $15 \text{ fb}^{-1}$  for the experiments, allowing each to begin to characterize the particle. By all standards, the discovery does indeed look to be the revered Higgs boson [29, 30].

### 3.5 Searches for neutral triple gauge couplings

Searches for anomalous neutral triple gauge couplings have been performed at LEP2 [31–35], the Tevatron [36, 37], and the LHC [38–40]. Since no direct evidence has been observed, all results are quoted as upper limits. The most stringent limits to date were set by the author and the CMS collaboration [40]. The limits on each of the couplings are summarized in 3.1.

| Experiment  | $f_4^Z$        | $f_4^\gamma$   | $f_5^Z$        | $f_5^\gamma$   | Comments   |
|-------------|----------------|----------------|----------------|----------------|--|
| ALEPH [31]  | [-0.60;0.61]   | [-0.40;0.36]   | [-1.22;1.10]   | [-0.81;0.79]   | 2D fit results                                     |
| DELPHI [32] | [-0.40;0.42]   | [-0.23;0.25]   | [-0.38;0.62]   | [-0.52;0.58]   |  |
| L3 [35]     | [-1.9;1.9]     | [-1.1;1.2]     | [-5.0;4.5]     | [-3.0;2.9]     | $\sqrt{s} = 189$ GeV                               |
| OPAL [33]   | [-0.45;0.58]   | [-0.32;0.33]   | [-0.94;0.25]   | [-0.71;0.59]   |  |
| LEP WG [34] | [-0.30;0.30]   | [-0.17;0.19]   | [-0.34;0.38]   | [-0.32;0.36]   | LEP combination                                    |
| CDF [37]    | [-0.12;0.12]   | [-0.10;0.10]   | [-0.13;0.12]   | [-0.11;0.11]   | $\Lambda=1.2$ TeV                                  |
| D0 [36]     | [-0.28;0.28]   | [-0.26;0.26]   | [-0.31;0.29]   | [-0.20;0.28]   | $\sim 1 \text{ fb}^{-1}$ ,<br>$\Lambda=1.2$ TeV    |
| ATLAS [38]  | [-0.12;0.12]   | [-0.15;0.15]   | [-0.13;0.13]   | [-0.13;0.13]   | $\sim 1 \text{ fb}^{-1}$ ,<br>$\Lambda=2$ TeV      |
| ATLAS [38]  | [-0.07;0.07]   | [-0.08;0.08]   | [-0.07;0.07]   | [-0.08;0.08]   | $\sim 1 \text{ fb}^{-1}$ ,<br>$\Lambda=\text{inf}$ |
| ATLAS [39]  | [-0.019,0.019] | [-0.022,0.023] | [-0.020,0.019] | [-0.023,0.023] | $4.6 \text{ fb}^{-1}$ ,<br>$\Lambda=3$ TeV         |
| ATLAS [39]  | [-0.013,0.013] | [-0.015,0.015] | [-0.013,0.013] | [-0.016,0.015] | $4.6 \text{ fb}^{-1}$ ,<br>$\Lambda=\text{inf}$    |
| CMS [40]    | [-0.011;0.012] | [-0.013;0.015] | [-0.012;0.012] | [-0.014;0.014] | $\sim 5 \text{ fb}^{-1}$ ,<br>$\Lambda=\text{inf}$ |

**Table 3.1:** Summary of existing 95% C.L. intervals for the neutral aTGC  $f_4^Z$ ,  $f_4^\gamma$ ,  $f_5^Z$  and  $f_5^\gamma$ .

## Chapter 4

# Experimental Overview of the LHC and CMS

The Large Hadron Collider (LHC) is the latest (and most powerful) collider built to date. It sits beneath the French-Swiss border outside of Geneva, in the tunnels that were originally used to house LEP. It was designed for proton-proton collisions, with designed center-of-mass energies of up to 14 TeV. These design center of mass energies will not be reached until after a series of hardware updates which are currently underway. This thesis uses instead the collision data collected at 7 and 8 TeV center-of-mass energies.

The LHC houses 4 major detectors, in addition to a handful of secondary experiments. The Compact Muon Solenoid (CMS) and A Toroidal LHC Apparatus (ATLAS) are general-purpose detectors that sit roughly across from each other on the main proton ring. LHCb is a detector specializing in b-physics (the physics of mesons containing bottom quarks). The fourth major experiment is the A Lead Ion Collider Experiment, or ALICE. This detector is designed for primary operation during the LHC's heavy ion collision mode. Additional experiments, such as TOTEM

and LHCf, are smaller in scale, but aim for important measurements (these in particular aim, respectively, for total pp cross section measurements and forward neutral pion measurements).

The operation of the LHC is outlined in Section 4.2, while CMS and its subcomponents are explained in detail in Section 4.3.

## 4.1 Definitions of Terminology

The geometry of the CMS detector is defined such that the  $\hat{x}$ -axis points toward the center of the ring, and the  $\hat{y}$ -axis points upward. The  $\hat{z}$ -axis, then, points in the direction of the proton beam circulating counterclockwise around the ring (when viewed from above). The angle  $\phi$  is measured up from the  $\hat{x}$ -axis in the xy plane, while the polar angle  $\theta$  is measured up from the  $\hat{z}$ -axis. The polar angle is often used to describe the particle's *pseudo-rapidity*,  $\eta$ , defined as:

$$\eta = -\ln \left( \tan\left(\frac{\theta}{2}\right) \right)$$

The rate of particles per unit area available for collisions is called the *instantaneous luminosity*,  $\mathcal{L}$ :

$$\mathcal{L} = \frac{f_{rev} n_b N_b^2 \gamma_r}{4\pi \epsilon_n \beta_*} F \quad (4.1)$$

where  $f_{rev}$  is the frequency of the particles' revolution,  $n_b$  is the number of bunches present in the beam chain,  $N_b$  is the number of particles in each bunch,  $F$  is a geometric factor resulting from the crossing angle of the beams,  $\gamma_r$  is the relativistic gamma factor, and  $\epsilon_n$  is the normalized beam emittance in the transverse direction. These beam parameters are set by the machine's operating abilities, with the denominator interpretable as how tightly squeezed the beam is in the x-y plane (as it travels along a z-axis).

## 4.2 The Large Hadron Collider

The proton beams which feed the collisions in the LHC start in a modest hydrogen tank at the beginning of the Linac2 linear accelerator. The hydrogen atoms are stripped of their electrons, becoming protons that are accelerated along the linear accelerator up to an energy of 50 MeV. The protons are then injected into the Proton Synchrotron Booster (PSB), where they are further boosted to 1.4 GeV. The next step are the Proton Synchrotron (PS) and Super Proton Synchrotron (SPS), which accelerate them to 25 and 450 GeV respectively.

After the SPS, the proton beams are injected into the LHC ring, with beams circulating in opposite directions through the 27 kilometer circumference ring. Here they are accelerated to their final energy, stored, and steered toward collision. The accelerator chain is depicted in Figure 4.1. The acceleration of the protons at each stage is done using RF (radio frequency) cavities. Inside of these cavities, the carefully time oscillations of electromagnetic fields ‘push’ the proton bunches to accelerate them. The timing of these oscillations also help keep the bunches together, as protons lagging slightly behind the majority receive a larger relative boost than protons in the bulk. There are sixteen of these cavities in the LHC ring, with eight being used for each of the beams. The operating frequency of 40 MHz is driven by the nominal LHC bunch spacing, allowing for bunch spacings of 25 ns.

The beams are steered using a series of 1232 superconducting dipole magnets, with magnetic fields of up to 8.3 Tesla. Because there are two proton beams within the LHC ring circulating in opposite directions, the dipoles have a twin-bore design. In this setup, there are two beam pipes, with each pipe having its own set of coils to produce the steering field. In addition to the dipoles, there are 400 quadrupole magnets which focus the proton bunches.

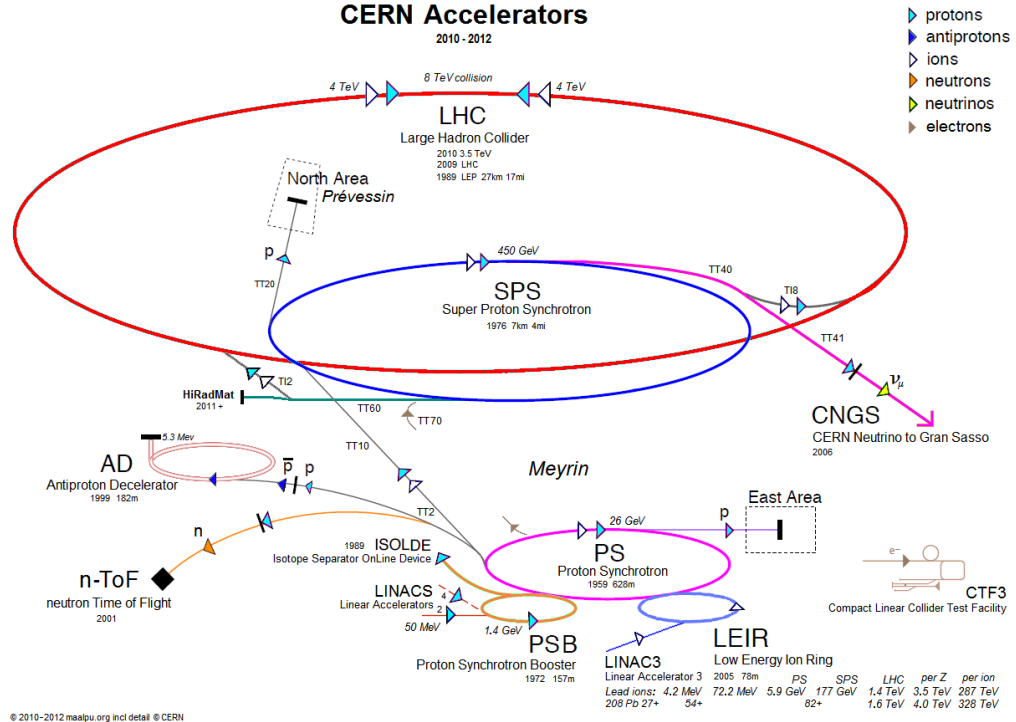


**Figure 4.1:** The LHC acceleration chain. Protons start in the Linac2 accelerator (bottom, center), are accelerated through the PSB, PS, and SPS before being injected into the LHC ring.

|                                       | 2011            | 2012            | Design |
|---------------------------------------|-----------------|-----------------|--------|
| Center of mass collision energy (TeV) | 7               | 8               | 14     |
| Peak Inst. Lumi. ( $cm^{-2} s^{-1}$ ) | 3.54            | 7.67            | 1.0    |
| Peak Colliding Bunches                | 1331            | 1380            | 2808   |
| Maximum pileup                        | 16.15           | 34.55           | 19.02  |
| Maximum recorded data, single fill    | 118.0 $pb^{-1}$ | 238.9 $pb^{-1}$ | -      |

**Table 4.1:** Peak Machine Specifications for 2011 and 2012 proton-proton collisions at the LHC.

### 4.3 The Compact Muon Solenoid detector

The Compact Muon Solenoid, or CMS, is one of the two multi-purpose detectors on the LHC experiment. It is immense, both in size and scope. It is 21.6 meters long, 14.6 m in diameter, and weighs in at about 12,500 t. The various components were primarily built on the surface before being lowered into the detector cavern, 100 m

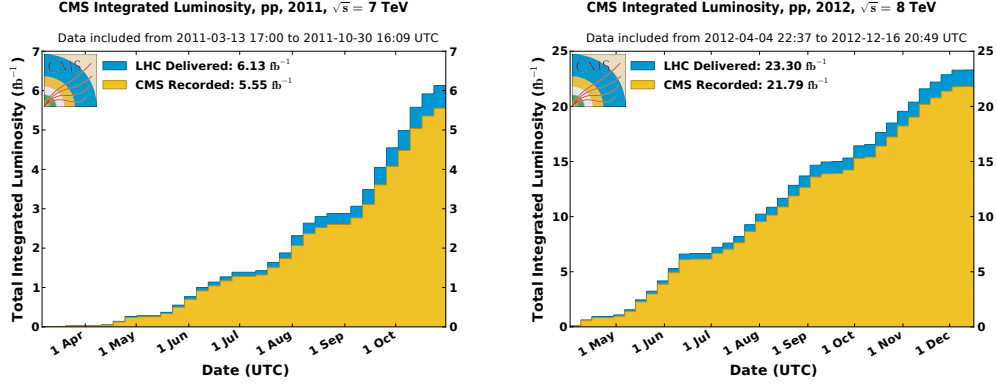


**Figure 4.2:** The amount of integrated luminosity delivered by the LHC and recorded by the CMS detector in each week of 2011 (left) and 2012 (right).

below ground. CMS sits at the LHC “Point 5,” located near the French town of Cessy, roughly on the opposite side of the ring from ATLAS and the main CERN campus.

Like many detectors, CMS features an inner tracking system (for determining the momenta of charged particles), a magnetic solenoid (in order to bend the trajectory of charged leptons for accurate momenta measurements), electromagnetic and hadronic calorimeters (for measurements of particle energy), an outer muon system (for detection of muons, which tend to pass through the inner components without significant interaction). CMS is unique in the placement of the magnet outside of the calorimetric elements: the ‘compact’-edness of the tracker and calorimeter allow these components to fit inside the magnet. In traditional detectors, the magnet is placed immediately outside of the tracking system, meaning that particles can interact (and lose energy) in the material of the magnet before reaching the calorimeters.

An isometric diagram of the detector is shown in figure 4.3, while a cutaway showing a fraction of the xy-plane of the detector with a simulated collision interaction is shown in figure 4.4

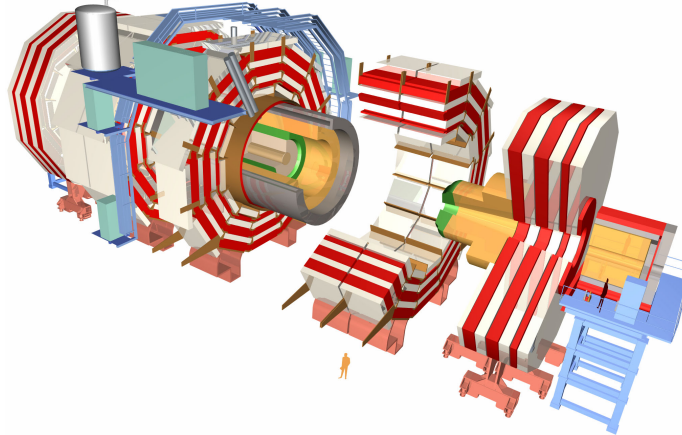


**Figure 4.3:** An exploded isometric view of the CMS detector, showing the overall geometry and layering of the components.

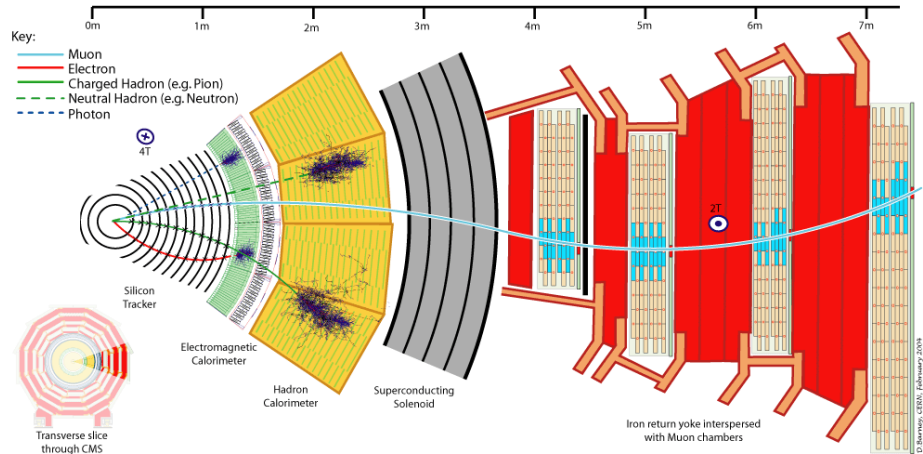


**Figure 4.4:** A diagrammed slice of the CMS detector, showing the components' nesting and the interactions of different particle types with the subcomponents.

### 4.3.1 Tracker

The innermost component of the CMS detector is the silicon tracking system. Its role in particle detection is twofold: to provide accurate spatial measurements for primary and secondary vertices and to accurately measure the curved trajectories from the charged particles. The tracker system sits just outside the beampipe, with detecting area starting at a radius of 4.4 cm, extending to radial distance of 1.1 meters. The

system is 5.8 m in length, with disks at either end of the cylinder to provide coverage in the pseudorapidity range  $|\eta| < 2.5$ . The system is made of two subcomponents: the *pixel detector* and the *silicon strip detector*. In both systems, the primary technology used for particle detection is reverse-biased np silicon junction. As charged particles pass through the silicon, ionization deposits in the substrate cause a depletion current which is read out electronically. The use of this silicon technology allows very thin sensors to be used, minimizing particles' interaction with non-detection material while providing the extremely quick detection response times required by the high collision rates provided by the LHC. The layout of the tracker is provided in Figure 4.5.

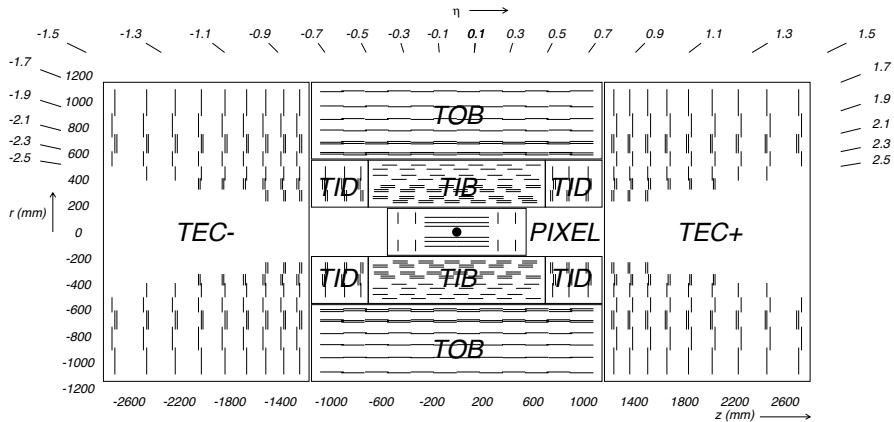


**Figure 4.5:** The geometry of the inner tracking system of CMS. There are three innermost layers compose the so-called pixel detector, consisting of  $100 \times 150 \mu\text{m}^2$  silicon pixels. These pixels provide excellent spatial granularity in the most densely occupied region. The primary purpose of these pixel layers are to provide very fine position measurements in all three dimensions. The pixels provide measurements in the  $r-\phi$  plane with a resolution on the order of  $10\mu\text{m}$  and in the  $r-z$  plane to about  $20\mu\text{m}$ . This fine granularity provides the ability to pinpoint, in three dimensions, the location of primary and secondary vertices. Secondary vertices are the

The three innermost layers compose the so-called pixel detector, consisting of  $100 \times 150 \mu\text{m}^2$  silicon pixels. These pixels provide excellent spatial granularity in the most densely occupied region. The primary purpose of these pixel layers are to provide very fine position measurements in all three dimensions. The pixels provide measurements in the  $r-\phi$  plane with a resolution on the order of  $10\mu\text{m}$  and in the  $r-z$  plane to about  $20\mu\text{m}$ . This fine granularity provides the ability to pinpoint, in three dimensions, the location of primary and secondary vertices. Secondary vertices are the

result of decays of short-lived particles that are born in the primary interaction (such as a b-quark traveling a short distance before hadronizing into a jet). In total, there are 66 million pixels, providing about  $1m^2$  of detecting area. The position resolution provides CMS with the ability to accurately locate primary collision vertices, critical both in momenta measurements of curved tracks and pile-up rejection. Both of these benefits are discussed in further detail in later chapters of this thesis.

The next 10 layers of the tracking system are covered by the silicon strip detector, extending to an outer radius of 1.1 m. Because of the lower track occupancy in this region, the detecting components are not designed to have as fine a granularity along the  $\hat{z}$ -direction. The strips located in the barrel region measure  $10cm \times 180\mu m$  in the inner four layers, known as the tracker inner barrel (*TIB*), and  $25cm \times 180\mu m$  in the outer six layers (the tracker outer barrel, or *TOB*). The strip detector subsystem is completed in the more forward endcap regions by the tracker inner disks (*TID*) and tracker endcaps (*TEC*).

The information from the pixel and strip detectors are combined to recreate the path of the charged particles. Because the tracker sits inside of a 3.8 T magnetic field, the particle paths are curved, allowing measurements of the momenta through the Lorentz equation:

$$p = qBR \quad (4.2)$$

where  $q$  is the particle's charge,  $B$  is the strength of the magnetic field, and  $R$  is the radius of curvature. Particles with higher momenta have less visible curvature within the detector and as a result have a larger momenta resolution:

$$\frac{\sigma(p_T)}{p_T} = p_T \cdot 0.015\% \oplus 0.5\%, (|\eta| < 1.6) \quad (4.3)$$

$$\frac{\sigma(p_T)}{p_T} = p_T \cdot 0.05\% \oplus 0.5\%, (1.6 < |\eta| < 2.5) \quad (4.4)$$

The charged particles in this analysis are typically in the 10-50 GeV range, giving them resolutions on the at the sub-percent level (or a few percent in the more forward regions).

### 4.3.2 Electromagnetic Calorimeter

The next detector component that a particle encounters on its journey outward through the detector is the electromagnetic calorimeter (*ECAL*). This detector is designed to capture all of the energy of the electrons and photons produced in the collisions (or subsequent decays).

The calorimeter is composed of over 76,000 lead tungstate ( $\text{PbWO}_4$ ) crystals. As electromagnetic particles pass through these crystals, they produce electromagnetic showers. The light from these showers is amplified and collected by avalanche photodiodes in the barrel region and vacuum phototriodes in the endcap regions. The use of  $\text{PbWO}_4$  crystals was motivated by their radiative resistance, light response, density, and the resulting compactedness of the calorimeter as a whole. The dense crystals ( $8.28\text{g}/\text{cm}^3$ ) result in an extremely short radiation length of  $0.89\text{cm}$  and a very small Moliere radius ( $2.2\text{cm}$ ). The geometry of the crystals is designed to utilize these characteristics, with typical sizes being  $22 \times 22\text{mm}$  at the front face,  $26 \times 26\text{mm}$  at the rear face, and  $230\text{mm}$  in length. As a result, particles are almost guaranteed to interact somewhere along the crystal length (traversing roughly 26 radiation lengths), with the resulting EM showers leaking minimally out of one or two crystals. In addition to the excellent spatial gains of the crystals, they are additionally very quick. The scintillation decay time is sufficiently short so that roughly 80% of the light is emitted within the 25 ns corresponding to the nominal LHC bunch cross rate.

The crystals are bundled into submodules, which are grouped into modules which vary in makeup in order to optimize the uniformity of the crystal coverage. These

modules are then grouped into supermodules, which consist of 1700 crystals, with a 20 crystal coverage in  $\phi$  and an 85 crystal coverage in  $\eta$ .

The ECAL is composed of three primary subcomponents: the barrel (*EB*), the endcap (*EE*), and the preshower (*ES*). The *EB* covers the area within  $|\eta| < 1.479$  and contains the bulk (61,200) of the PbWO<sub>4</sub> crystals. The *EE* covers the forward regions, with a pseudorapidity coverage of  $1.56 < |\eta| < 3.0$  and contains 7234 PbWO<sub>4</sub> in each endcap. The crystals in the endcaps are slightly larger than those in the *EB*, with a front face of  $28.62 \times 28.62\text{mm}$  and a rear face of  $30 \times 30\text{mm}$  with a length of 220 mm. The *ES* sits just in front of the endcap crystals, providing an  $|\eta|$  coverage from 1.653 to 2.6. It is composed of a layer of lead radiators to produce electromagnetic showers, with silicon strip detectors behind to measure the deposits. The purpose of the *ES* is primarily to detect forward neutral pions, in order to distinguish the neutral mesons from photons. The layout of the ECAL is pictured in Fig. 4.6.

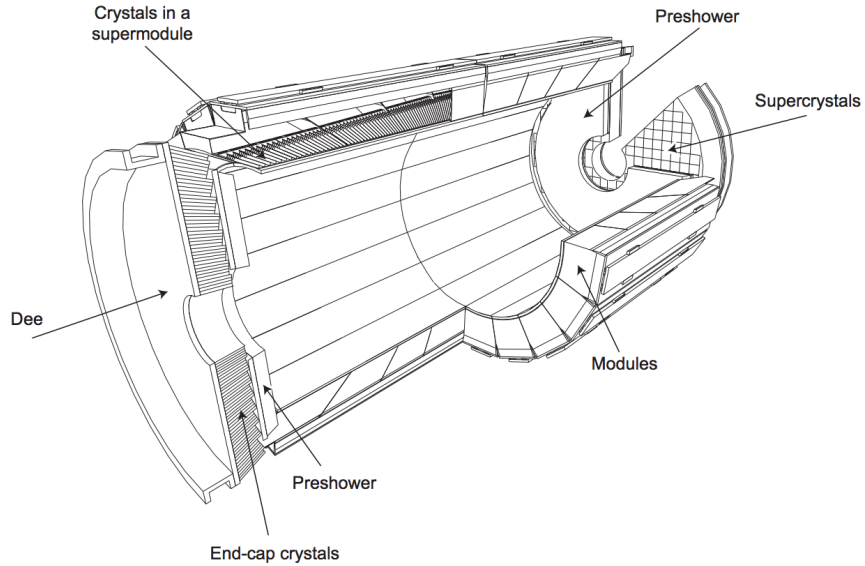


**Figure 4.6:** The geometry of the CMS Electromagnetic Calorimeter, diagramming the crystals, modular structure, and overall layout of the *EB*, *EE*, and *ES* subcomponents.

Because of the high granularity, the ECAL provides excellent spatial resolution for a calorimeter. However, the crystals' beam-facing orientation combined with the lack of a segmented depth setup means that there is no information provided about the angle of the particles as they enter the calorimeter. Thus, the positional information is limited to the size of the crystals themselves.

The radiation due to the large flux of particles through the detector has the effect of harming the overall transparency of the crystals. As a result, the energy measurements tend to drift over time, resulting in systematic deviations of energy measurements (and larger variations in response from crystal to crystal).. This is handled using a laser calibration system, which provides a set of corrections and calibrations which evolve over the length of a run.

The energy measurement of the ECAL is energy-dependent:

$$\left(\frac{\sigma(E)}{E}\right)^2 = \left(\frac{2.8\%}{\sqrt{E}}\right)^2 + \left(\frac{0.12}{E}\right)^2 + (0.30\%)^2 \quad (4.5)$$

with the energy is provided in GeV. The first term is due to the inherent statistical nature of the EM showering processes, while the second is due to electronic noise. The third term is due to non-uniformity in the geometric layout of the detector and calibration uncertainties.

### 4.3.3 Hadronic Calorimeter

The Hadronic Calorimeter (or *HCAL*), which sits outside of the ECAL, is built with the intent to measure the energy of the hadronic jets. It is important in the measurements of missing transverse energy, which is energy carried away by non-interacting particles (such as neutrinos or some kinds of exotic particles). In addition to providing key measurements of hadronic energy, the HCAL also provides a useful layer of discrimination for potentially fake electromagnetic particles. If an ECAL deposit

is associated with an HCAL deposit, there is a good chance that the particle was a hadron which interacted with a nucleus in the ECAL (since truly electromagnetic particles like the electron will deposit 100% of their energy in the ECAL).

In addition to its inherent value to jet studies and missing transverse energy  $ME_T$  calculations, the HCAL is also key in measuring the amount of pileup present in a collision. As most analyses are sensitive to the number of soft interactions underlying their events of interest, it is important to account and correct for the energies and compositions of these pileup events. The HCAL, with its wide coverage in  $|\eta|$  provides measurements critical in these corrections.

The HCAL is a sampling calorimeter, meaning the shower-inducing and energy measurement components are physically separate media. Like the ECAL, it is split into barrel and endcap regions (commonly called the HB and HE subcomponents). In addition, there is a forward hadronic calorimeter (HF), which sits 11 m forward of the interaction point. Radially, the HCAL fits snugly between the ECAL and the solenoid, extending from a radius of 1.77 m to 2.95 m. The HB coverage extends to  $|\eta| < 1.305$ , while the HE covers  $1.305 < \eta < 3.0$ . The HF covers the most forward regions of the detector, covering  $3.0 < \eta < 5.0$ . The geometry of the hadronic calorimeter is diagrammed in figure 4.7.

The HB and HE subcomponents use interspersed sections of brass (to induce hadronic showering) and scintillator to measure the resulting energy. In the more forward HF, where the radiation is a much great concern, the sampling is done using steel plates coupled with quartz fibers. The interaction length,  $\lambda_i$ , of the brass material is 16.42 cm, meaning that a hadronic jet will be reduced to 1/e of its energy for each 16.42 cm of brass it traverses. The amount of material increases with the azimuthal angle so that the number of interaction lengths through the entire HCAL increases from  $5.82 \lambda_i$  to  $10.6 \lambda_i$  at an  $|\eta|$  of 1.3. The HE has similar coverage, with

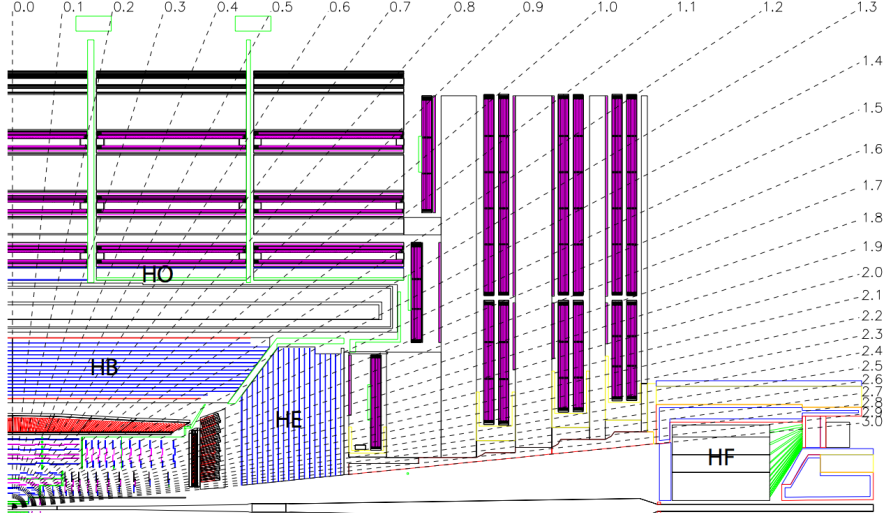


**Figure 4.7:** The geometry of a fraction of the CMS hadronic calorimeter. The HB provides coverage to  $|\eta| < 1.3$ , the HE covers  $1.3 < |\eta| < 3.0$ , and the HF covers  $3.0 < |\eta| < 5.0$ . The dashed lines indicate equal intervals in  $\eta$ .

about  $10 \lambda_i$  of total material.

The energy resolution for the HCAL is given by:

$$\left( \frac{\sigma(E)}{E} \right)^2 = \left( \frac{90\%}{\sqrt{E}} \right)^2 + (4.5\%)^2, HB/HE \quad (4.6)$$

$$\left( \frac{\sigma(E)}{E} \right)^2 = \left( \frac{172\%}{\sqrt{E}} \right)^2 + (9.0\%)^2, HF \quad (4.7)$$

where the first term is due to the statistical fluctuations of the hadronic showering and the second term arises from geometric variations and calibration uncertainties.

#### 4.3.4 The Magnet

The most striking feature of CMS is the object that gives the detector its name: the solenoid. The magnet is 6 m in diameter, 12.5 m long, and weighs 220 tonnes. The superconducting solenoid, consists of 4 layers of NbTi coiling, capable of producing the 18 kA necessary for the desired 3.8 T magnetic field. This magnetic field is responsible

for causing the trajectory of the charged particles to bend within the tracker, allowing accurate momenta measurements. An iron yoke is staggered with layers of the muon chambers, providing the detector with structural support in addition to feeding a 2 T return field. This return field allows additional curvature for the muon momenta measurements.

### 4.3.5 Muon chambers

The outermost component of the CMS detector is the muon system. As suggested by the name, these subsystems are designed to identify and measure muons. In addition to the spatial accuracy, it is also critical for the muon systems to be relatively fast, in order to efficiently trigger on muons within a certain bunch crossing (as described in 4.3.6). Because muons are so much heavier than electrons, they largely escape the inner detector components (where the electrons lose their energy through bremsstrahlung radiation). As mentioned in 4.3.4, the central portions of the muon system sit in the  $\sim 2$  T return field of the solenoid. The field strength, combined with the radial size of the muon system, allow accurate muon momenta measurements across a wide spread of energies.

The muon system utilizes three different technologies to achieve its goals of precise and quick muon measurements. Drift tubes (DTs) are precise, but relatively slow. This makes them ideal for the barrel region ( $|\eta| < 1.2$ ), where particle rate is expected to be lower. The cathode strip chambers (CSCs) are used in the more forward regions ( $0.9 < |\eta| < 2.4$ ), where the increased particle rate requires a quicker technology. Finally, the resistive plate chambers (RPCs) cover out to  $|\eta| < 1.6$ . RPCs are the quickest technology, but provide coarser position measurements than either the DTs or CSCs. They are used primarily for triggering and for resolving ambiguously reconstructed tracks from other chambers. An overview of the muon system

geometry is provided in Figure 4.8.

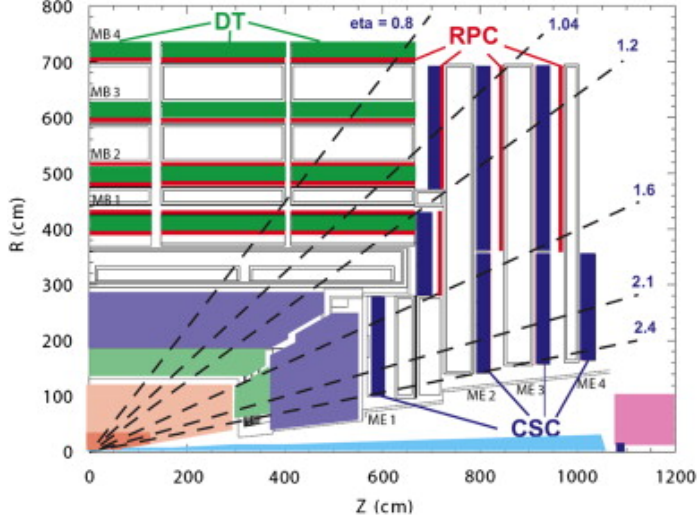


**Figure 4.8:** The geometry of the muon system, composed of the drift tubes (DTs), cathode strip chambers (CSCs), and resistive plate chambers (RPCs).

The DT system that covers the barrel area consists of four nested stations. The inner three systems are composed of 60 drift chambers each, while the outermost station contains an additional 10 chambers (70 total). The chambers themselves are filled with a mix of argon and CO<sub>2</sub>. As the muon passes through the gas, it causes a cascade of ionization. In each cell of the DT chambers is a long wire under a high voltage. The electrons knocked off of the gas are pulled to the wires, resulting in a detectable pulse. The time it takes these electrons to drift to the wire is known as the drift time, and is roughly 380 ns in this gas mixture. The well-known drift time allows for precise position measurements, but because it is much larger than the 25 ns spacing between bunch crossings, the drift tube technology can only be applied in the central area, where occupancy is sufficiently low. The spatial resolution of the DT system is excellent, providing measurements to an accuracy of 100  $\mu\text{m}$  in the  $r - \phi$  plane and 150  $\mu\text{m}$  in the  $\hat{z}$ - direction. A schematic of a drift tube chamber is provided in Figure 4.9. The half-cell staggering between cell layers provides the

system with a timing resolution of 3.8 ns, allowing precise identification which bunch-crossing birthed the muon.

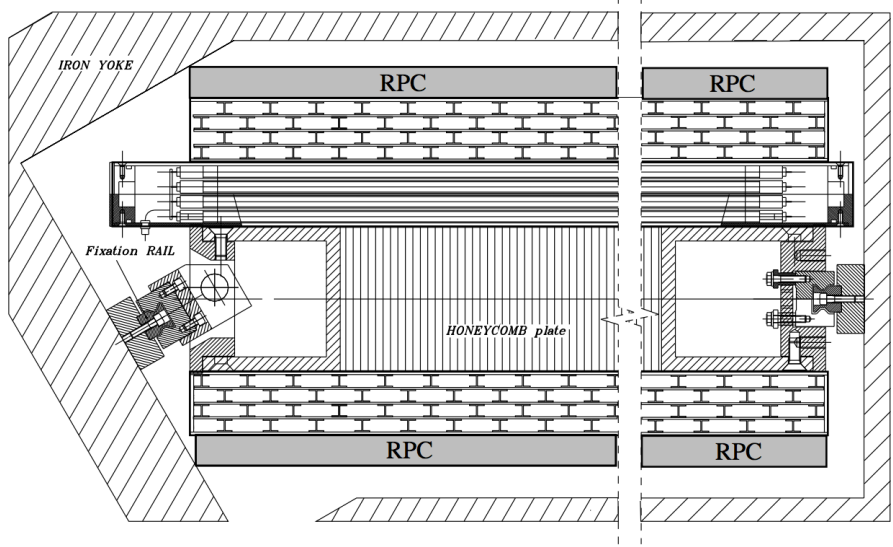


**Figure 4.9:** A schematic of a drift tube chamber, in the  $r - \phi$  plane. Visible are two cells running parallel to the beamline (immediately above and below the RPCs) and one cell perpendicular to the beam (above the honeycomb plate).

The CSCs are used in the endcap regions, where the higher flux of particles and non-uniformity of the magnetic field make the drift tubes suboptimal. They consist of a weave of copper cathode strips and anode wires placed within a volume of gas. Each chamber contains 7 of the cathodes, with 6 planes of wires running perpendicular across them. The chambers cover 10 or  $20^\circ$  of  $\phi$  and are staggered in placement to provide full coverage. Similar to the DTs, particles moving through the gas result in ionization. The positive ions produced are pulled toward the negatively charged copper cathodes while the negatively charged ions are attracted to the positively-charged wires. As a result of the fine perpendicular ‘grid’ spacing between the strips and the wires, the CSCs have a quicker response time than the DTs (CSC pulses last  $\sim 150\text{ ns}$ , compared to the  $\sim 380\text{ ns}$  drift time), while maintaining similar levels of spatial resolution. The overall timing resolution of the CSC is 7 ns (when utilizing

the entire chamber), and its position measurements are accurate to the  $100\ \mu\text{m}$  level.

The RPCs are the quickest technology of the muon systems, but provide the poorest spatial measurements. The chambers consist of two highly resistant plates separated by a gap filled with gas. An electric field is set up in such a way that the chambers work in a so-called “avalanche mode”—when the gas is ionized by a particle passing through, a cascade of further ionizations occur. Each RPC detecting element consists of two gaps joined with a common readout strips between them. The total signal is the combined effect of the two gaps, providing a higher detection efficiency and lower voltage requirements than a single-gap setup. Though the spatial resolution of the RPCs is poor in comparison to the DTs and CSCs (at the 1 cm level), the RPCs have a much faster response time than the other muon systems, with a time resolution down to the order of 1 ns. As a result, the RPCs are able to precisely tag which bunch crossing a given muon came from, making it invaluable in the triggering process.

#### 4.3.6 Data Acquisition and Trigger

The 25 ns design bunch separation means that beam collisions occur with at the rate of 40 MHz. Because the full detector readout produces on the order of 1 MB of data per bunch crossing, some 40 TB of potential data is produced in each second of operation. As it is obviously impossible to store (or readout) such an enormous amount of data, CMS was designed with a two-stage trigger system to reduce the rate of stored collisions to a more reasonable (sub-kHz) level. The filtering must be done in such a way that those events which contain physically interesting processes are kept, while the uninteresting events are removed. The Level-1 (L1) trigger is a hardware system that is designed to reduce event rate to the order of 100 kHz. This subset of the events is then sent to the High-Level Trigger (HLT), which is a

software system implemented on a computing farm of commercial CPUs. The HLT uses a fuller event reconstruction in order to make much more involved decisions on the event, resulting in the final filtered event rate of  $\sim 1$  kHz.

### 4.3.7 L1 Trigger System

The L1 Trigger system is a hardware system utilizing a mix of FPGAs and ASICs. The L1 chain begins locally, where muon chamber track segments or calorimeter deposits are used to produce Trigger Primitives (TPs). The TPs are then utilized in a regional calculation, which covers a subsection of the detector. From the regional stage, a sorted list of objects is passed to the global trigger subsystems (either the Global Muon Trigger or the Global Calorimeter Trigger), which determine the highest rank objects from the muon and calorimeter systems. These are then passed to the Global Trigger (GT), where the final decision (accept/reject) is made. The accepted events are then passed to the HLT for further processing. A diagram of the flow through the L1 Trigger system is depicted in Figure 4.10

#### Calorimeter Trigger

The basic unit in the calorimeter trigger is the trigger tower, corresponding spatially to a  $5 \times 5$  grouping of ECAL crystal plus the similarly size HCAL cell behind it. The energies in each trigger tower are summed by the Trigger Primitive Generators (TPGs) and passed to the Regional Calorimeter Trigger (*RCT*) for further processing. The RCT is made of 18 electronics crates, each one housing 7 receiver cards and 7 electron identification cards (each of which provides coverage for two  $4 \times 4$  regions of trigger towers) and one jet/summary card. The RCT decompresses the energies reported by the calorimeter TPGs, and finds the most energetic electron/photon candidates (no distinction between them is made at this level) within each regions.

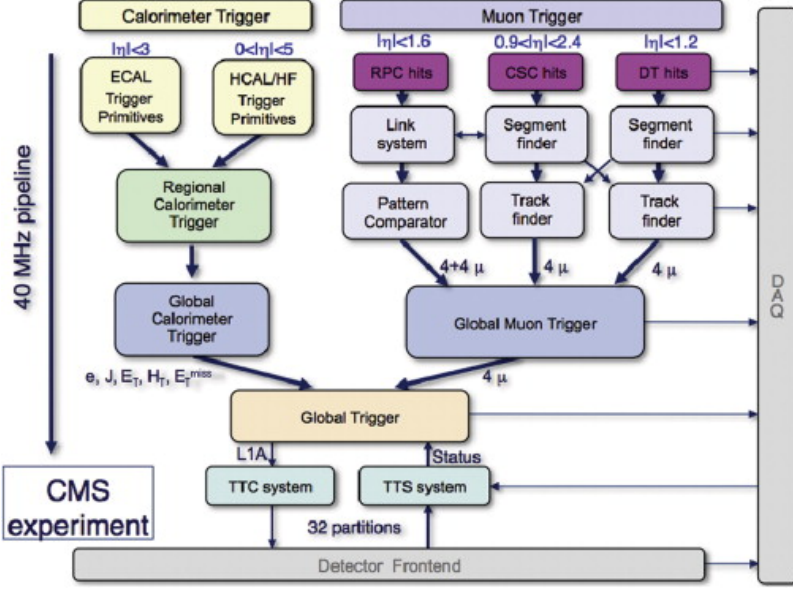


**Figure 4.10:** Diagram of the information flow through the CMS trigger system.

There are, in addition, checks to see whether each of these candidates is isolated or not. The RCT passes the four highest non-isolated candidates, the four highest energy isolated highest candidates, and the energy sums from each region on to the Global Calorimeter Trigger (GCT).

As the name suggests, the GCT is the first level at which calorimeter information is processed for the entire calorimeter trigger geometry. It uses this information to compute a number of event-level properties, such as jet multiplicities, missing transverse energy ( $ME_T$ ), and the scalar jet energy sum ( $H_T$ ). In addition, it finds the highest energy electron/photon candidates (both isolated and not) and identifies hadronic jets within the calorimeter. These values are all passed to GT.

## Muon trigger

The L1 muon trigger system uses information from all three muon subsystems in order to maximize the efficiency and background rejection. The CSC and DTs provide local track segments, which are then combined into regional muon tracks by their Track

Finder systems (CSCTFs and DTTFs). The DT provides coverage in the barrel region, up to  $|\eta| < 1.2$ , while the CSCs cover the more forward regions,  $0.9 < |\eta| < 2.4$ . The RPC also provide regional track candidates (with excellent timing resolution) with an  $|\eta|$  coverage up to 1.6. The DT and CSC systems each pass 4 muon candidates to the GMT, while the RPCs pass a total of 8 (4 from the barrel region and 4 from the endcap region). Matching between CSC+RPC and DT+RPC candidates ensure that the spatial, momentum, and timing measurements are optimally efficient for triggering. This information, consisting primarily of  $p_T$ , charge, position, and quality of measurement, is passed to the GT which, in combination with the information from the GCT, makes a trigger decision based on the event as a whole.

#### 4.3.8 HLT System

After an event is accepted at the L1 level by the GT, it is passed to the HLT for further processing. Within the HLT, the event goes through well-defined reconstruction paths, in order to most quickly comb out those events which contain potentially interesting physics. Because the event rate coming through the HLT is still immense (on the order of 100 kHz), the HLT does not necessarily run a complete event reconstruction—instead it just unpacks and utilizes the pertinent information, governed by the events’ triggers at the L1 level. Because the HLT can utilize more complete snapshots of the event topology, especially information from the tracker system, it has the ability to reject a significant subset of events (with fake lepton signals or noisy QCD jet events), outputting roughly 400 Hz of events for storage. The triggers utilized in this analysis involve finding two (or more) isolated leptons above a certain  $p_T$  threshold. These are explained in more detail in Chapter 7.

# Chapter 5

## Event Generation and Simulation

In order to guide an analysis (whether the goal is to search for a new particle or to measure the strength of a physical coupling), it is important to understand how the physical aspects will manifest themselves within the context of the LHC and CMS. For optimizing analysis strategies, physicists utilize an extensive method of simulation, based on the Monte Carlo methodology [41]. From the interactions between quarks, the kinematics of intermediate particles, the decay into final products, and the final interaction of final-state particles with the CMS detector, these simulations are designed to paint a full picture of the physical event.

### 5.1 Monte Carlo Simulation

The basis of the simulations lies in the Monte Carlo method, which uses randomization to sample an integration space and, if numerous enough, will converge to a known underlying distribution. In this way, it is possible to create enormous samples of simulated events which follow the underlying equations governing the fundamental interactions.

The first step in the simulation process is to calculate the *matrix element* of an process. The matrix element corresponds to the probability of some physical process, typically visualized with Feynman diagrams like those from Chapter 2. In order to provide a suitably robust set of simulation events, events are generated by sampling the matrix element *phase space* (the allowed kinematic regime of a process). For each point sampled, a weight is calculated, based roughly on how likely an event in that region of phasespace would be. Once a full sample is produced, the events are then ‘unweighted’. In this process, these weights are normalized to the maximum value. Then, for each event, a random number is thrown and, if the random number is larger than the normalized weight, the event is rejected. In this way, the final collection of events each have an equal weight, but are composed of a properly distributed population.

Because of the complex structure of the collisions at the LHC, it is impossible to measure (and tune) the momenta of the constituents involved in the processes. As a result, these matrix elements are also dependent on the *parton distribution functions* (PDFs). These are probabilistic functions which define the relative amounts of momentum carried by each of the constituents in the protons involved in the collision. Due to the energy scales of the interactions involved, these probabilities are beyond the scope of current QCD calculations, so as a result, the PDFs are derived based on previous experimental probings of the partonic structure [42–44]. A comparison of the three PDF sets used within this analysis is shown in Figure 5.1, reproduced from [45].

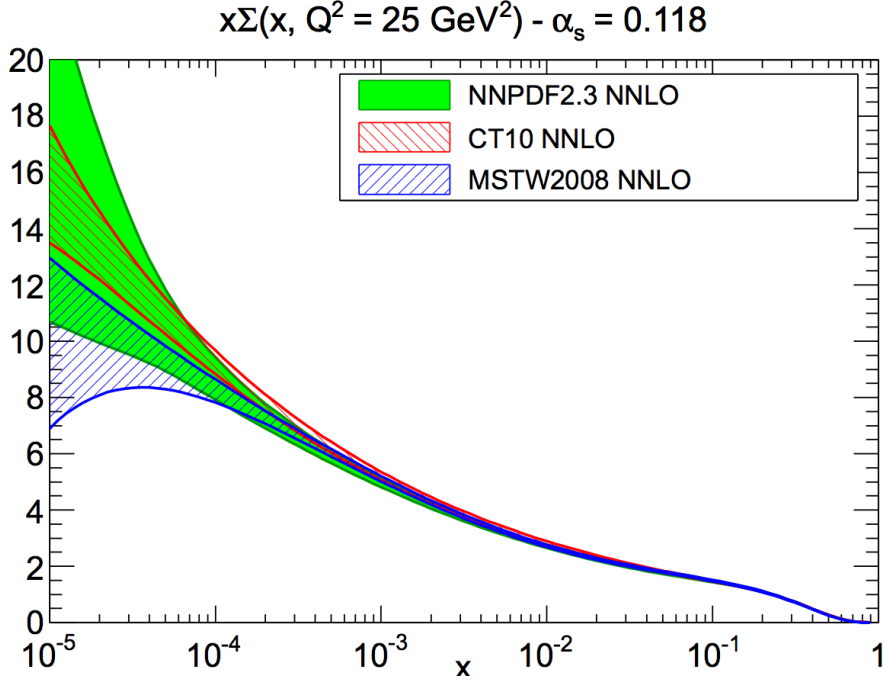


**Figure 5.1:** A comparison of the PDF sets NNPDF [44], CT10 [43], and MSTW08 [42], reproduced from [45].

## 5.2 Parton Showering

Although the matrix element method outlined in Section 5.1 simulates the hard (high-momentum transfer) of event, it does not provide any simulation of any of the hadronic showering in the event. As mentioned in Chapter 2, individual partons cannot be observed, instead forming a cascade of hadrons which shower the detector. This hadronic activity can arise through the hard interactions directly (for example, a  $Z_0$  boson decaying hadronically), radiated from an initial or final state, or from the *underlying event*. The underlying event is a result of QCD's color conservation—as the partons in the proton interact in the hard process, the partons that remain in the proton must themselves form into colorless states.

Because of the low energies involved in the soft interactions, it is difficult (or impossible) to apply the standard tools of QCD calculations to the hadronization

process. Instead, a purely phenomenological approach is taken, known as the Lund string model [46]. In this model, the partons are attached with a gluon ‘string’. As the string stretches (meaning the partons move apart), its energy increases until it can create new quark/antiquark pairs, at which point it ‘snaps’. Quarks and antiquarks from nearby sprays can combine into mesons, or the quark cascade can continue, as diagrammed in Fig. 5.2.

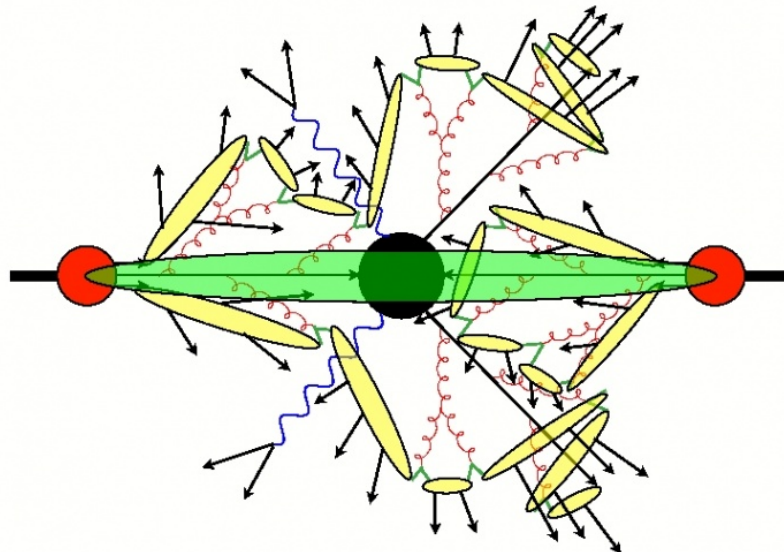


**Figure 5.2:** A diagram depicting the hadronization process [47]. The hard process is highlighted in green, while the various hadronizations are in yellow.

### 5.3 Pile-up

In addition to the simulation of the hard process and the partonic showering, simulated physics events also require a description of the *pile-up*. Pile-up events are interactions which occur between other protons within the bunch crossing. In order to simulate the effect that these events have on the hard process, *minimum bias*

(soft events) are superimposed on top of the event of interest. The number of these events added is assigned randomly so that the overall distribution of the amount of pileup per event matches the data as closely as possible. Because of the long timeline involved in generating MC samples, it is necessary to apply corrections in order to properly represent the distribution in data. These corrections are further explained in Chapter 7).

## 5.4 Generator Software

There are many different software packages that have been written for MC event generation. They primarily differ in the order of the calculation. Some, such as Sherpa and Pythia, involve only leading order perturbative QCD calculations. Other generators, such as POWHEG BOX, MADGRAPH, MC@NLO, and MCFM include next-order effects in the calculations. Typically, the LO MC generators include the full chain from initial state to final detectable objects. The NLO generators, are typically interfaced with a second program (commonly PYTHIA) in order to handle the hadron showering processes.

## 5.5 Samples used

This analysis utilizes both NLO and LO matrix element generators, while relying on Pythia [48] for all showering, hadronization, and underlying event generation.

The primary Higgs boson signal samples are generated using POWHEG [49], covering both the gluon-gluon fusion and vector boson fusion production mechanisms at NLO. These samples are weighted to NNLO calculations (VBF) or NNLO+NNLL (gg) ([50]). Although the generated Higgs  $p_T$  spectra does not match that of the

NLO+NNLL calculations, the effects of this difference were found to be negligible to the analysis as a whole.

Two different matrix element generators are used in production of the Standard Model ZZ samples.  $q\bar{q} \rightarrow ZZ \rightarrow \ell\ell\ell\ell$  samples are produced with POWHEG at NLO, while  $gg \rightarrow ZZ$  production is handled at LO via gg2zz [51].

Samples with anomalous triple gauge couplings were all produced with the LO generator SHERPA [52], as it is the only ME generator which has the requisite couplings modelled. Although only a LO generator, an extensive study indicated that the generator well reproduces the four-lepton invariant mass

MADGRAPH [53] is used to produce the simulated sample of  $Z_0 \rightarrow \ell\ell$  plus hadronic jet activity, which is the largest reducible background. The use of MADGRAPH in these samples is important, as the accurate modelling of the jets is especially critical, given that this background enters the signal region through the hadronic jets faking a signal-like lepton. This sample is weighted to the calculated NNLO cross section.

More specific information about the samples used in this analysis are in Tables 5.1.

## 5.6 Detector Simulation

Once the physics events are generated, their interactions with the material composing CMS (and their resulting detection) must also be simulated via GEANT4 [54]. At its core, this software suite simulates the stochastic interactions between the particles created in the collision and the matter of CMS (both detecting and non-detecting). GEANT4 contains an in-depth geometrical model of CMS, from the specifications of the detecting components to the material budget of the non-detecting portions (such as structural support and readout electronics). GEANT4 also provides simulation

| 8 TeV Samples   |           |               |  |  |  |
|---|-----------|---------------|--|--|--|
| Sample  | Generator | $\sigma$ (pb) |  | Fiducial cuts                          |  |
| ZZTo4L_8TeV-powheg-pythia6/Summer12                       | POWHEG    | 0.07691       |  | $m_{\ell\ell} > 4GeV$ , $l=e,\mu,\tau$ |  |
| ZZTo2L2L_8TeV-powheg-pythia6/Summer12                     | POWHEG    | 0.1767        |  | $m_{\ell\ell} > 4GeV$ , $l=e,\mu,\tau$ |  |
| GluGluToZZTo4L_8TeV-gg2zz-pythia6/Summer12                | gg2ZZ     | 0.0048        |  | $m_{\ell\ell} > 4GeV$                  |  |
| GluGluToZZTo2L2L_TuneZ2star_8TeV-gg2zz-pythia6/Summer12   | gg2ZZ     | 0.01208       |  | $m_{\ell\ell} < 4GeV$                  |  |
| DYJetsToLL_M-50_TuneZ2Star_8TeV-madgraph-tarball/Summer12 | MADGRAPH  | 3503.71       |  | $m_{\ell\ell} > 50GeV$                 |  |
| DYJetsToLL_M-10To50filter_8TeV-madgraph/Summer12          | MADGRAPH  | 915           |  | $10 < m_{\ell\ell} < 50GeV$            |  |
| TTTo2L2Nu2B_8TeV-powheg-pythia6/Summer12                  | POWHEG    | 23.64         |  |  |  |
| GluGluToHToZZTo4L_M-*_8TeV-powheg-pythia6/Summer12        | POWHEG    | *             |  |  |  |
| VBF_HToZZTo4L_M-*_8TeV-powheg-pythia6/Summer12            | POWHEG    | *             |  |  |  |
| WH_ZH_TTH_HToZZ_M-*_8TeV-pythia6/Summer12                 | POWHEG    | *             |  |  |  |
| ZZTo4L with aTGCs   | SHERPA    | 0.057-0.064** |  | $m_{\ell\ell} > 12GeV$ , $e/\mu$ only  |  |

**Table 5.1:** A list of the samples utilized in the 8 TeV portion of this analysis, the generator used, and the sample cross-section. A \* denotes the fact that there was a wide range of Higgs masses used, while a \*\* means that there was a number of different coupling values used. Full details for each are explained in Chapter 7.

of the effects of the solenoid, calculating trajectories based on actual magnetic field measurements.

GEANT4 provides a picture of how the particles interact with the detector components, but one final stage remains in the event simulation chain. In order to be fully comparable to experimental data, the events must pass through a simulated version of the electronic detector readout. Each subcomponent of the detector provides an electronics simulation, so that effects of electronic noise and timing are represented in the simulated samples. At the end of this simulation chain, the MC samples exist in the same raw format as the data when read out by the CMS detector. As a result, both simulation and real data can be passed through the same *reconstruction* process, allowing direct head-to-head comparisons between the two.

# Chapter 6

## Event Reconstruction

The data (and the Monte Carlo simulations) come out of the detector (or its emulated counterpart) in similar collections of raw measurements. At this stage, only information about tracker hits, muon chamber hits, and calorimeter deposits exist. In order to be useful in a physics setting, these detector signatures must be translated into their physics counterparts. The process of running the raw data through complex algorithms designed to pick out the myriad particles in the event is called *reconstruction*. A full description of the reconstruction algorithms utilized in this analysis follows.

### 6.1 Vertex and Track Reconstruction

The first step in reconstructing the physics content of an event is mapping hits in the silicon tracker systems to a particle. This is done using a *Kalman Filter*, which starts at an inner tracking ‘seed’ point and adds successive hits to each potential track. As it adds hits to the potential tracks, it propagates a likely position for a next hit forward, giving the algorithm a place to look for the next contribution. After the

track is built, the process is repeated, building a track from the outermost hits to the inner regions. This has the effect of smoothing the overall track and minimizing the measuring errors at the vertex origin [55].

Because each event is accompanied by a large number of pile-up events (up to 35 in 2012 running), it is important to be able to distinguish each particles' tracks along with where, with respect to the interaction point, they originated from. These places of origin, known as vertices, are reconstructed in two phases. First is the *track finding* algorithms, which associate the measured tracks with a potential vertex. This is done via *deterministic annealing*, a machine learning algorithm which models the tracks as a thermodynamic system, clustering the tracks by minimizing the effective free energy of the system [56, 57]. Vertex fitting, on the other hand, is the process of measuring a vertex's properties (especially its position and associated errors). Once a vertex is found and fit, the tracks are again recalculated, using the vertex as an additional position in the track fit algorithm [58]. In order to separate the vertices associated with pileup events with the interaction of interest, each event is given a *primary vertex*, defined to be the one with the highest sum of squared track transverse momenta.

## 6.2 Electron Reconstruction

Electron reconstruction at CMS comprises of combining tracks with matching *superclusters*, large groups of associated clusters in the ECAL (see Fig. 6.1). In supercluster construction, the smaller clusters are collected in such a way as to capture both the primary ECAL deposit and the deposits spread in  $\phi$  that result from bremsstrahlung radiation as the electron travels its helical course through the detector.

Basic electron reconstruction can be done in one of two ways. An electron can

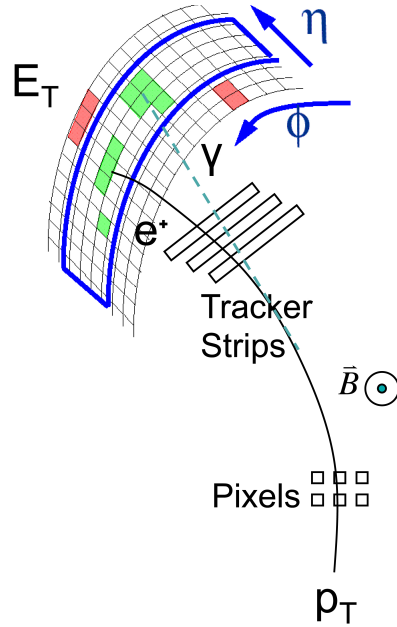


**Figure 6.1:** Diagram of an electron travelling through the CMS detector. The electron emits bremsstrahlung radiation as it bends, resulting in a signature in the ECAL consisting of both the electron deposit and the radiated photon energies. The supercluster (blue) is a collection of deposits which capture the electron and associated photon energies.

either be *tracker-driven* or *ECAL-driven*. The tracker-driven approach is most effective for electrons that are low in  $p_T$ , starting with the collection of reconstructed tracks and searching for compatible hits in the ECAL. The ECAL-driven approach, on the other hand, is designed to be more efficient for the higher  $p_T$  electrons, like those utilized in this analysis. It begins with the supercluster collection and matches these to hits in the inner tracker. The full electron trajectories are reproduced using a Gaussian Sum Filter algorithm. This algorithm allows a more robust reconstruction of the electron track when compared to the Kalman Filtering, as it is able to account for the inherent kinks and bends due to the bremsstrahlung processes the electron can undergo on its journey through the tracker [59].

In this analysis, additional quality requirements are placed upon the electrons, as outlined in Chapter 7.

## 6.3 Muon Reconstruction

Muons in CMS are reconstructed using a combination of tracks, independently reconstructed in the inner tracker and muon systems (colloquially referred to as tracker tracks and standalone tracks, respectively. Like the electrons, muons also have two possible modes of reconstruction, depending on whether the matching begins from the tracker tracks or the standalone tracks.

*Global muon* reconstruction begins in the muon system, taking the standalone tracks and matching them to tracker tracks that follow a similar propagation path. The global muon track is then built, using the hit information in both systems. *Tracker muon* reconstruction begins with tracker tracks with  $p_T > 0.5 \text{ GeV}$  and total momenta  $p > 2.5 \text{ GeV}$ . These tracks are then treated as potential muons, and their expected paths are extended into the muon system. If matching segments are found near to the extrapolated muon path, the matching muon hits are added to the track hits in order to create the muon object.

Although the inner tracker has greater resolving power in making track momenta measurements, the muon system provides invaluable information for high  $p_T$  ( $\sim 100 \text{ GeV}$ ) muons. Because these muons bend only slightly while traveling through the tracker system, the additional hits in the muon system help to resolve the momenta of these objects.

It is possible for tracks to be reconstructed in multiple muon candidates, as more than one inner tracks can be geometrically close to the backwards-extrapolated standalone tracks. These so-called ‘ghost’ muons result in a non-physical doubling of muon candidates. In order to treat this effect, which becomes more pronounced in higher pile-up scenarios, the ghost muon pairs are arbitrated. If two muons are nearby and share more than half of their segments, the worse of the pair is discarded (as de-

fined by a suite of criteria based on the track quality measurements and, if needed, additional identification criteria).

## 6.4 Particle Flow

Unique in CMS is the so-called *particle flow* process, a suite of reconstruction algorithms designed to fully reconstruct and identify all the stable particles created in an event. More specifically, the algorithms are designed to pick out all of the individual electrons, muons, charged hadrons, neutral hadrons, and photons in an event. This information can be used in a number of different ways, from using the identified objects themselves to recombining the information into jets. Especially relevant to this analysis is the particle flow muon criteria (which help to establish the collection of well-identified muons used in the analysis) and the photon, charged hadron, and neutral hadron collections, which are used to establish how much additional energy is present near the candidate leptons.

Particle flow first lumps tracks, clusters, and muons into “blocks,” which are simply groups of these objects which pass a loose connectedness test. Individual particles are then combed out of each block. The process starts with muons, identifying a particle-flow muon as a global muon with momenta compatible with a tracker muon. The tracks, muons, and calorimeter signature attributed to the found muons are then removed from the block and electrons are identified, using criteria similar to those outline above. Again, associated tracks and calorimeter clusters are removed from the block. Remaining calorimeter clusters are assigned to (well-reconstructed) tracks if the deposits are consistent with a charged-hadron hypothesis, or assigned to neutral hadron or photons, based on whether the energy was deposited in the HCAL or ECAL. This procedure is discussed in greater detail in [60].

# Chapter 7

## Analysis Strategy

The ZZ $\rightarrow 4\ell$  analysis is characterized by having four well-identified, isolated leptons combined into oppositely charged, same flavor pairs. The selection requirements placed on the leptons are relatively loose (as described in section 7.2), in order to maximize the efficiency of successfully selecting all four leptons. Because there are so few physics signals that result in four prompt leptons, the resulting background contributions are slight, even with these loose requirements. The primary reducible background for this signature is a  $Z_0$  boson produced in association with two jets. Each jet has a small probability of faking an isolated lepton, as they can either be tightly collimated (and look like electrons) or can contain a muon itself which passes selection. This background is estimated from data, using the methodology outlined in Section 7.4.

### 7.1 Online Selection

CMS data coming through the data acquisition system is sorted into a number of *primary datasets*, based on which trigger(s) the event passed. Because the signature of

this analysis is four muons, four electrons, or two muons and two electrons, the relevant datasets are the DoubleElectron, DoubleMuon, and Muon+Electron collections. Each of these datasets is used, with overlaps between them explicitly removed. The trigger menus, which define the L1 and HLT trigger requirements, evolved throughout the 2011 and 2012 running. At every stage, the utilized triggers were those with the lowest thresholds which remained unprescaled (meaning that 100% of the events passing that trigger were stored).

The online trigger section of the analysis begins with a requirement of finding two or more leptons at the L1 level, with some loose identification and isolation criteria applied. These trigger objects are used as input to higher level triggers, which do further event unpacking and apply a more refined event selection. The HLT requirements (and their L1 seeds) are summarized in Table 7.1.

| Final State    | L1 Seed                                   | HLT Trigger               |
|----------------|---|---------------------------|
| eeee           | Two electrons, $E > 13, 8$                | CaloTrk, $p_T > 17, 8$    |
|                | Three electrons, $E > 12, 7, 5$           | $p_T > 15, 8, 5$          |
| $\mu\mu\mu\mu$ | Two muons, one with $E > 10$              | $p_T > 17, 8, *$          |
|                | Two muons, one with $E > 10$              | $p_T > 17, 8, **$         |
| $ee\mu\mu$     | Two electrons, $E > 13, 8$                | $p_T > 17, 8$             |
|                | Two muons, one with $E > 10$              | $p_T > 17, 8 *$           |
|                | Two muons, one with $E > 10$              | $p_T > 17, 8 **$          |
|                | One electron $E > 12$ , one muon          | $\mu p_T > 8, e p_T > 17$ |
|                | One electron, $E > 6$ , one muon $E > 12$ | $\mu p_T > 17, e p_T > 8$ |

**Table 7.1:** The L1 seeds and HLT triggers used in each final state. A \* indicates the presence of two globally reconstructed muons, while \*\* indicates the higher  $p_T$  muon is global, while the lower  $p_T$  muon is required only at the tracker level.

The numbers in the HLT paths indicate the  $p_T$  threshold of the trigger object. As the triggers do not reach their peak efficiency until a few GeV above the threshold, in order to not cut into the turn-on curve, offline  $p_T$  requirements of 20 and 10 GeV on separate leptons are enforced (as the HLT requirements on the di-lepton triggers are leptons of 17 and 8 GeV).

Electrons in the di-electron triggers have a set of very loose calorimeter and tracker based isolations applied, along with a tight calorimeter identification criteria and very loose track identification. The tri-electron trigger includes only a loose calorimeter identification criteria on each electron in addition to a very loose track criteria.

## 7.2 Lepton Definitions

### 7.2.1 Isolation

A distinct signal of a prompt lepton (one that comes directly from a relevant physics event) is that it is well-isolated. In general, prompt leptons deposit recognizable signatures in the tracker and calorimeter subdetectors with little accompanying energy. Leptons coming from jets (or jets reconstructed partially as leptons) are often surrounded by additional calorimetric and tracker activities from the spray of particles that accompany the jet.

In this analysis, the *particle flow isolation* variables are used [60]. To calculate a lepton's isolation, a cone of size 0.4 in  $\Delta R = \sqrt{\Delta\phi^2 + \Delta\eta^2}$  is drawn around each lepton. The scalar sum of the  $p_T$  from all the particle flow objects within this cone are summed up:

$$\text{Isolation} = \sum_{\text{charged hadrons}} p_T + \sum_{\text{neutral hadrons}} p_T + \sum_{\text{photons}} p_T \quad (7.1)$$

Because isolation is simply a measure of extra energy near a candidate lepton, it is sensitive to the amount of pile-up present in the event. In order to correct for this extra energy, two changes are made to equation 7.1. First, only the subset of charged hadrons associated with the primary vertex are used, removing all the charged hadrons coming from secondary (pile-up) vertices. This is a standard CMS procedure, colloquially referred to as the PFNoPileup approach. Because the photon and neutral

hadron components do not have track information, they cannot easily be categorized into pile-up and non pile-up contributions. Instead, pile-up effects are accounted for using the so-called  $\rho$ -correction (or *fastjet correction*, [61]). In this approach, the average energy density of all the jet activity in the event is taken as a measurement of pile-up activity. This number is then multiplied by the *effective area* of the lepton, a scaling factor determined by the way the lepton's neutral hadron/photon isolation component and the event's  $\rho$  respond to an increase in pile-up. These effective areas are taken from independent measurements from  $Z_0$  boson production and are provided by the electron and muon Physics Object Groups. The resulting product,  $\rho A_{eff}$  is a measurement of the neutral hadron+photon isolation contribution due solely to pile-up events, and is removed from these components.

$$\text{Isolation} = \sum_{\text{charged hadrons}}^{\text{non-PU}} p_T + \max \left( \sum_{\text{neutral hadrons}} p_T + \sum_{\text{photons}} p_T - \rho A_{eff}, 0.0 \right) \quad (7.2)$$

The final selection criteria for both electrons and muons is that the amount of energy near the lepton does not exceed 40% of the measured  $p_T$  of the lepton itself:

$$\left( \sum_{\text{charged hadrons}}^{\text{non-PU}} p_T + \max \left( \sum_{\text{neutral hadrons}} p_T + \sum_{\text{photons}} p_T - \rho A_{eff}, 0.0 \right) \right) / p_T < 0.40 \quad (7.3)$$

### 7.2.2 Impact Parameter Requirements

A lepton's *impact parameter* can be used help distinguish between prompt and secondary leptons (which occur due to a photon conversion or a similar secondary process). The impact parameter is defined to be the distance of closest approach between the lepton's measured track and the event's primary vertex. In order to guarantee

that all four leptons originate from the primary vertex, there are loose constraints on the impact parameter:

$$d_Z < 1.0$$

$$d_{XY} < 0.5$$

$$SIP = \frac{IP}{\sigma_{IP}} < 4.0 \quad (7.4)$$

Where  $d_Z$  is the distance, along the  $\hat{z}$  direction between the impact parameter and primary vertex,  $d_{XY}$  is the distance between them in the  $\hat{x}\hat{y}$  plane, and SIP is the separation between the impact parameter and primary vertex divided by the error in the measurement.

### 7.2.3 Electrons

Electrons in this analysis begin with the set of reconstructed electrons, as outlined in chapter 6. They then pass through an identification process, in order to increase the purity of the electron collection. The identification is done using a multi-variate analysis (MVA) technique, in which many electron variables are fed into Boosted Decision Trees [62, 63]. This process combines information from all of the variables and, based on training from disparate samples, qualifies the leptons as signal-like or background-like [64, 65]. The variables used in training of the MVA are numerous, but can be split into three categorizations: electron-track matching, calorimetric signatures, and track parameters. A list of variables considered in the MVA, along with brief descriptions of each, are presented in table 7.2.

| Calorimeter-track matching variables   |   |  |
|--|---|--|
| Variable                               | Description   |  |
| $E_{SC}/p_{in}$                        | Total supercluster energy divided by inner track momentum   |  |
| $E_e/p_{out}$                          | Energy of cluster nearest to track divided by momenta at outermost track position.  |  |
| $ \eta_{in} $                          | Difference in $\eta$ between the supercluster and the closest point of the innermost track extrapolation                                    |  |
| $ \phi_{in} $                          | Difference in $\phi$ between the supercluster and the closest point of the innermost track extrapolation                                    |  |
| $ \eta_{out} $                         | Difference in $\eta$ between the extrapolation from the outermost track position and the nearest cluster.                                   |  |
| $\frac{1}{E_{tot}} - \frac{1}{p}$      | Reciprocal difference of supercluster energy and measured momenta.  |  |
| Calorimeter variables                  |   |  |
| Variable                               | Description   |  |
| $E_{HCAL}/E_{tot}$                     | Fraction of supercluster energy found in HCAL.  |  |
| $E_{ES}/E_{tot}$                       | Fraction of supercluster energy found in preshower.   |  |
| $\sigma_{in\eta}$                      | Width (in $\eta$ ) of the primary ECAL cluster.   |  |
| $\sigma_{i\phi \phi}$                  | Width (in $\phi$ ) of the primary ECAL cluster.   |  |
| $\eta$ -width                          | Width (in $\eta$ ) of the supercluster.   |  |
| $\phi$ -width                          | Width (in $\eta$ ) of the supercluster.   |  |
| $(E_{5x5} - E_{5x1})/E_{5x5}$          | Relative difference between the energy in the 5x5 and 5x1 pattern of crystals centered on the seed cluster.                                 |  |
| R9                                     | Energy sum in the 3x3 pattern of crystals centered on the seed divided by the total supercluster energy.                                    |  |
| Tracker variables                      |   |  |
| Variable                               | Description   |  |
| $f_{brem} = (p_{in} - p_{out})/p_{in}$ | Fraction of energy lost, assumed to bremsstrahlung. The difference in measured momenta between the innermost and outermost track positions. |  |
| $\chi^2$                               | Chi-squared value of the GSF track fitting.   |  |
| Hits                                   | Number of measured hits in the Kalman filter track fitting.   |  |
| $\chi^2$ (KF)                          | Chi-squared value of the Kalman Filter track fitting.   |  |

**Table 7.2:** List of electron variables used in the electron identification MVA.

The output of the BDT analysis is a number from -1.0 to 1.0, with signal-like electrons having values closest to 1.0. [64] The training of the MVA and the resulting selection is applied in six separate electron classifications, split in  $p_T$  and  $\eta$ . In order to pass the selection, the electron must have an MVA value above the value outlined in Table 7.3.

| $5 < p_T < 10\text{GeV}$    |       |
|-----------------------------|-------|
| $0 <  \eta_{SC}  < 0.8$     | 0.47  |
| $0.8 <  \eta_{SC}  < 1.479$ | 0.004 |
| $1.479 <  \eta_{SC} $       | 0.295 |
| $10\text{GeV} < p_T$        |       |
| $0 <  \eta_{SC}  < 0.8$     | 0.5   |
| $0.8 <  \eta_{SC}  < 1.479$ | 0.12  |
| $1.479 <  \eta_{SC} $       | 0.60  |

**Table 7.3:** The electron identification criteria. An electron passes the identification stage if the output of its MVA is greater than the indicated value.

The momenta of the electrons is corrected using simulation by applying an energy smearing technique in order to reproduce the calorimeter resolution conditions observed in data. Additionally, the energy scale of the electron superclusters in the data is corrected to match those observed in a Monte Carlo sample by applying corrections in electrons in  $(\eta, R9)$  bins. The mismeasurement is slight, but time dependent, so the corrections are applied in a run-range dependent manner.

Additionally, the ECAL energy measurement is corrected using a multivariate regression technique designed original for the  $H \rightarrow \gamma\gamma$  analysis [66]. The regression is based on Boosted Decision Trees, implemented in the TMVA toolset [62, 63, 67]. Training is done using a Drell-Yan Monte Carlo sample, splitting barrel and endcap electrons into two separate training categories. A wide variety of ECAL variables are used in the process, from shower shape variables and cluster shapes to energy, momenta, and location measurements. The regression is designed to correct the

simulated electrons' ECAL energy back to their generated values, from either the raw supercluster energy (in the barrel) or the supercluster plus preshower energies (in the endcap). The net effect is an increase in the invariant mass resolution, especially when one or both electrons are located in the endcaps [65].

All electrons are required to have a fully corrected  $p_T > 7 \text{ GeV}$  and to fall within  $|\eta| < 2.5$ .

#### 7.2.4 Muons

The muons utilized in this analysis are selected using a highly efficient set of criteria, as the risk of fake muons is much lower than that of fake electrons. As a result, only loose criteria are required to choose real muons while eliminating a large fraction of the fakes. The muons are required to be reconstructed via the Global or Tracker reconstruction algorithms (as described in Chapter 6). In addition, the muons are required to be identified as muons within the particle flow algorithm [60]. Within this algorithm, a tiered approach to muon identification is taken to ensure that both prompt and secondary (from a jet) muons are identified with high efficiency. Different criteria are placed on the muon identification based on whether or not the muon is isolated or non-isolated. The classification is based on an isolation value calculated by summing the transverse energy and energy from the tracks and calorimeter deposits around the muon, within a cone of  $\Delta R \leq 0.3$ . If the total amount of energy within this cone is less than 10% of the muon  $p_T$ , the loosest criteria are applied to their identification. To be classified as a PF-muon, there must exist only a valid fit between the tracks in the muon and inner tracking systems. The muons used in this analysis are expected to be well isolated, and should in general fall into this category. However, less isolated prompt muons can still be identified through the so-called PF-loose or PF-tight criteria. These rely on measurements on the number of muon chamber hits,

pattern matching between tracks and calorimeter deposits, and compatibility between tracker and muon tracks [68].

Momentum scale of the muons is calibrated using the *Rochester correction* method [69]. In this method, corrections are applied to both data and simulated events, so that the average value of  $1/p_T$  matches that of a Z decay as observed by a perfectly aligned CMS. These corrections are applied in bins of  $(Q, \eta, \phi)$ , to remove the effects of poorly modeled magnetic field or incorrect chamber alignments.

Muons are required to have a corrected  $p_T > 5 \text{ GeV}$  and to fall within  $|\eta| < 2.4$ .

### 7.2.5 Scale factors

Lepton reconstruction, identification, and isolation efficiencies differ slightly between data and MC simulation, due to slight inherent differences between real and simulated detector performance. In order to correct for these slight differences, the lepton efficiencies are measured in both, compared, and corrected in the MC samples. The efficiency measurements are done using the *tag and probe* method. In this method, an independent sample of Z bosons is selected, by finding opposite sign, same flavor leptons with invariant mass consistent with that of a  $Z_0$  boson. One lepton (called the *tag*) is required to pass a tight selection criteria, helping to ensure the purity of the  $Z_0$  sample. The other leg, called the *probe* is initially selected using only a loose criteria. This leg is then passed through the various selection criteria (the identification, isolation, and SIP requirements especially). After each cut is applied, the candidates are sorted into passing and failing collections, the Z peak (and the small amount of QCD background) are fit, and the resulting efficiencies are extracted. The process is done in both data and Monte Carlo samples, and the ratios (as a function of  $p_T$  and  $\eta$ ) are shown in figure 7.1 (reproduced from [70]). The Monte Carlo simulations are corrected in scale by applying, for each lepton, the data/MC weight factor for

the associated  $(p_T, \eta)$  bin. In general, agreement between the simulations and the observed leptons is excellent, differing only at the percent level.

The dominant systematic uncertainties on the tag in probe method lie in how the background and Z peak are modelled. Because the efficiency values are extracted via a background-subtracted fit, these tails can have a considerable effect on the final values. A conservative systematic is evaluated by scaling the number of events in the tails up and down by a factor of two, recalculating the efficiency, and taking the difference from the central value as the systematic uncertainty. Additionally, a 1% effect is added in quadrature to account for the shape of the  $Z_0$  pole. The size of these uncertainties is summarized in section 7.9.

### 7.3 Pile-up Reweighting

Because the simulated samples were produced with a pile-up scenario (which does not match the overall scenario in the final data samples), the simulated samples must be reweighted. By giving the simulated events a slightly higher or lower weight factor in the final distributions, it is possible to create a simulated sample whose net pile-up closely resembles that which is observed in the data.

The distributions of the reconstructed vertices, while a good indicator of pile up activity, are susceptible to biases coming from the trigger and vertex finding algorithms. As a result, the “true” number of pile-up interactions are used. In the Monte Carlo simulation, this number is immediately accessible. In the data, it comes from instantaneous luminosity measurements, stored in per-bunch-crossing per-luminosity section intervals. This measurement, combined with the total pp cross-section, is used to determine the pile-up distribution, as observed by CMS, as it evolves in time. The ratio between the observed and simulated pile-up distributions

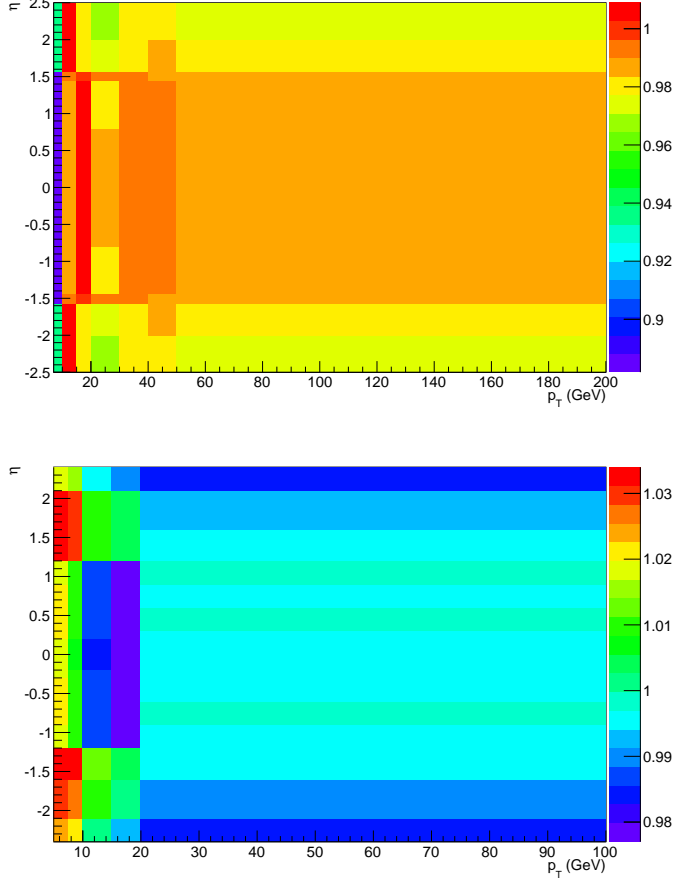


**Figure 7.1:** Ratio of lepton efficiencies between data and Monte Carlo simulations for electrons (top) and muons (bottom). Results are reproduced from [70].

for each bin in the simulated distribution tells how those events must be weighted in order to match the observed.

To test the effectiveness of using the “true” pileup variables described, one can easily check the effect on the reconstructed vertex distribution. The results can be seen in figure 7.2. After corrections, the MC sample successfully reproduces the pile-up scenario observed in data.

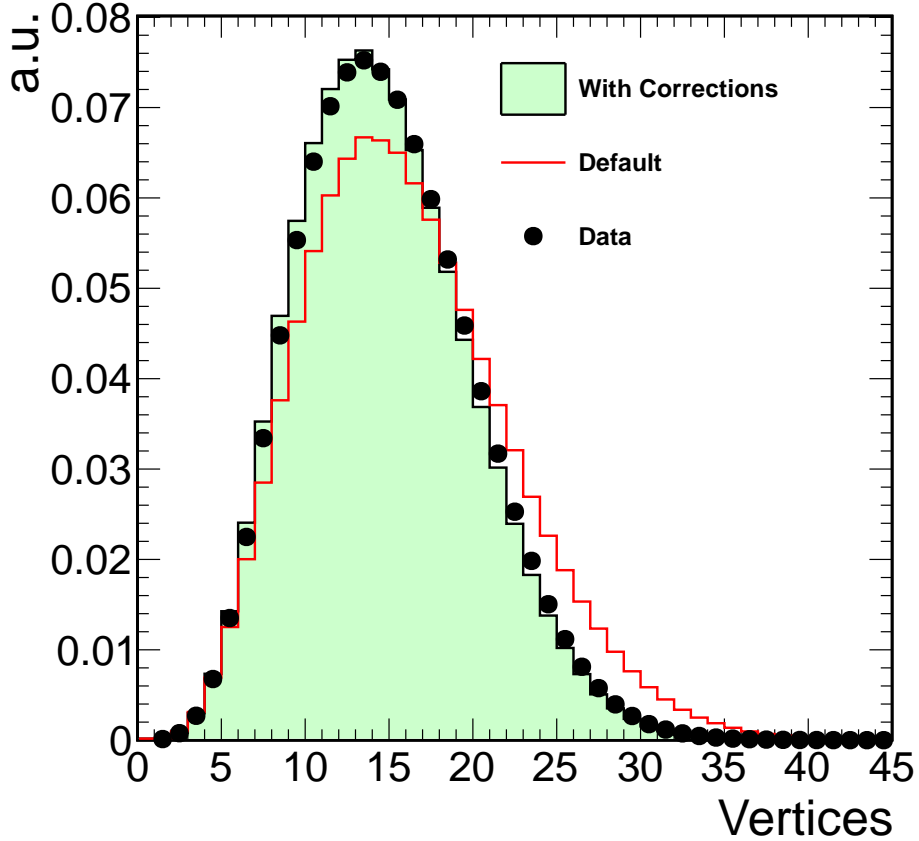


**Figure 7.2:** The effects of pile-up corrections, as described in the text, on the reconstructed vertex distribution. There is a significant improvement in the MC-data agreement when the corrections are applied.

## 7.4 Background Estimation

To estimate the reducible background contribution (coming primarily from a Z+jets signature with a much smaller contribution from the W/Z+jet production), a data-driven “fake-rate method” is utilized. In this approach, the probability for a loosely identified lepton (interpreted physically as a jet) to pass the full lepton selection is calculated. This fake rate is then applied to the population of a number of subregions which are dominated by these background physics events. This gives an estimate of the number of these events which are expected to pass the final selection criteria.

The first step is measuring the leptonic fake rates. This is done using in a “ $Z_0 + 1\ell$ ” region, where one  $Z_0$  boson is fully selected and there is exactly one additional loose lepton found in the event. These leptons have the requirements from Table 7.4 applied, with an additional event-level requirement of less than 20 GeV of missing transverse energy (in order to cut down contamination from WZ production).

|           |   |
|-----------|---|
| Electrons | $p_T > 7 \text{ GeV}$<br>$ \eta  < 2.5$<br>$< 2$ missing inner tracker hits<br>$ d_{XY}  < 0.5 \text{ cm}$<br>$ d_Z  < 1.0 \text{ cm}$                  |
| Muons     | $p_T > 5 \text{ GeV}$<br>$ \eta  < 2.4$<br>Global OR Tracker (with $\geq 1$ segment matched)<br>$ d_{XY}  < 0.5 \text{ cm}$<br>$ d_Z  < 1.0 \text{ cm}$ |

**Table 7.4:** The criteria placed on the loose lepton objects.

The leptonic fake rates are then measured as the number of loose leptons which pass final lepton selection (as defined in sections 7.2.3 and 7.2.4).

$$f = \frac{\text{Passing full selection}}{\text{Passing loose criteria}} \quad (7.5)$$

These fake rates, as a function of lepton  $p_T$ , are depicted in figure 7.3. The dependence on  $p_T$  is slight, and the fake rates are applied in a  $p_T$  independent manner.

In order to estimate the total background contributions due to fakes, potential backgrounds are split into two separate regions. The first region is composed of events which contain a fully selected  $Z$ , one lepton passing full selection, and one loose lepton which fails the final selection criteria ( $Z+1P1F$ ). These regions are dominated by  $Z_0$  boson production in association with two jets, where one of the jets ‘fakes’ a prompt lepton. In addition, there is a small contribution of W/Z+1 jet production in this

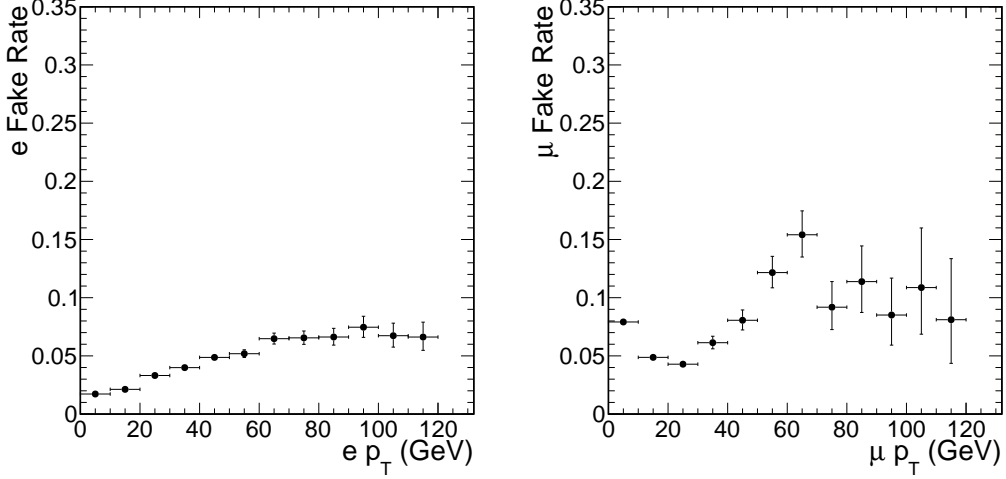


**Figure 7.3:** The leptonic fake rates, as a function of  $p_T$  for the electrons (left) and muons (right).

region (though the smaller cross section restricts its impact). The second region is composed of events with a fully reconstructed  $Z_0$  boson plus two additional loose leptons, both of which fail the final selection criteria ( $Z+2F$ ). This region is composed almost entirely of  $Z_0$  boson production. There is a negligible contamination of ZZ in each of these regions. The population for these regions for each of the final states (plus the combination) is shown in figures 7.4 and 7.5. The statistics in the simulated Drell-Yan sample has limited statistics when an on-shell Z is required (as seen in figures 7.6 and 7.7). However, the overall successful modelling of these control regions with the looser mass requirements (Figures 7.4 and 7.5) gives confidence in the method, as the expected physics processes are the same regardless of the mass requirement.

In general,  $N_F$  background-like events fail the final selection while  $N_P$  background-like events pass the final selection, and the fake rate can be written as

$$f = \frac{N_P}{N_P + N_F} \quad (7.6)$$

As a result, the population of background events passing the signal selection can be

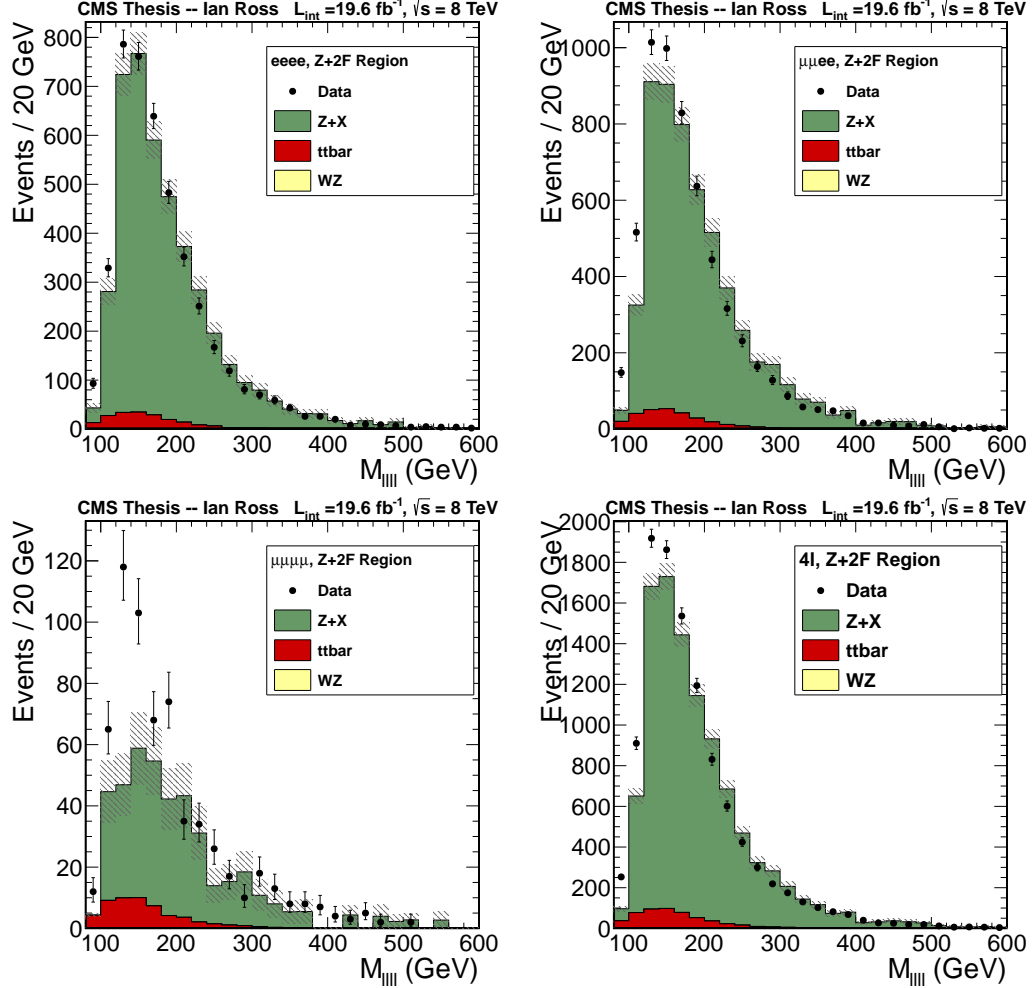


**Figure 7.4:** Background estimation region consisting of a  $Z_0$  plus two failed leptons. Counter clockwise from top right is the  $eeee$ ,  $\mu\mu ee$ ,  $\mu\mu\mu\mu$ , and summed final states.

written as:

$$N_P = N_F \frac{f}{1-f} \quad (7.7)$$

If one assumes the fake rates of Equations 7.5 and 7.7 are the same, then the final background is estimated by applying the measured fake rate to the regions as follows:

$$\text{Estimated Background} = \frac{f}{1-f} N_{1P1F} - \frac{f^2}{(1-f)^2} N_{2F}$$

where  $N_{1P1F}$  is the number of events in the  $Z+1P1F$  region, with the MC-driven expectation of ZZ contamination removed and  $N_{2F}$  is the  $Z+2F$  equivalent. The

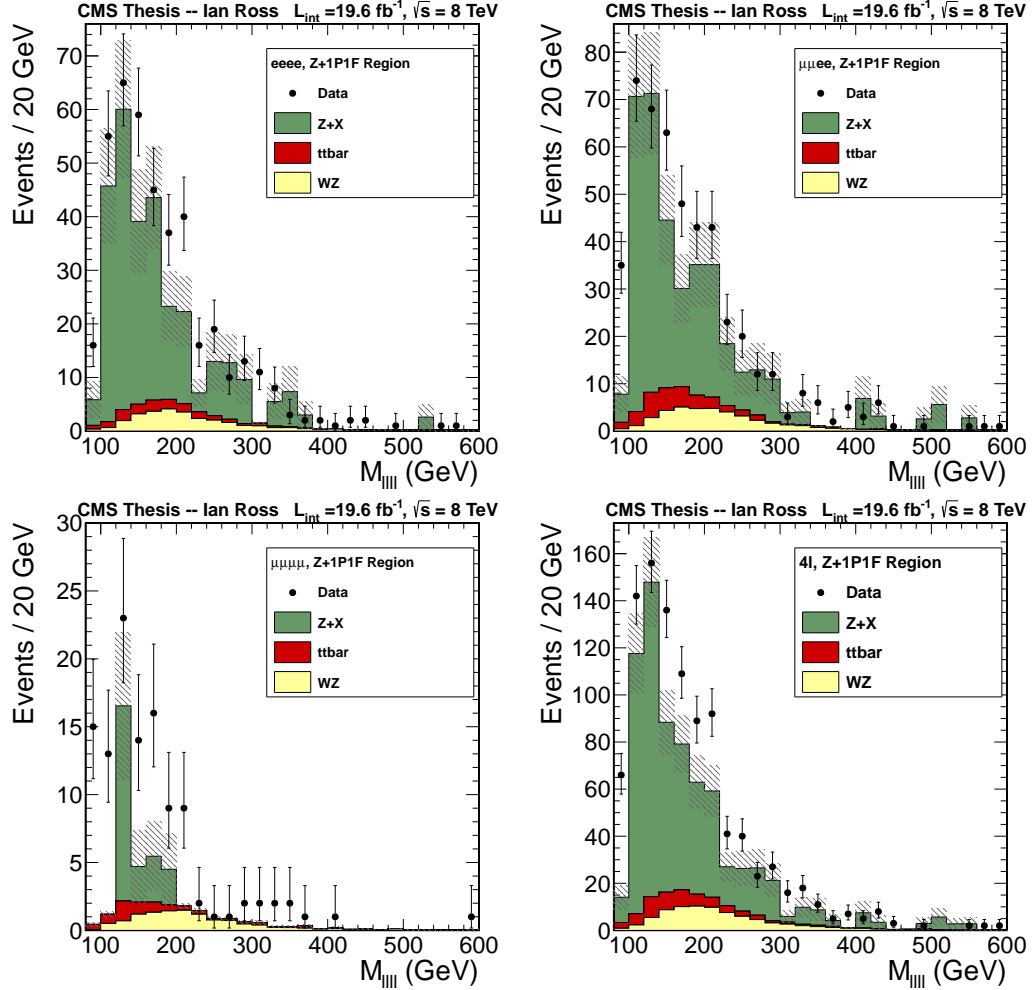


**Figure 7.5:** Background estimation region consisting of a  $Z_0$  plus one passed and one failed leptons. Counter clockwise from top right is the  $eeee$ ,  $\mu\mu ee$ ,  $\mu\mu\mu\mu$ , and summed final states.

removal of the  $Z+2F$  contribution is required due to the fact that these events are doubly represented in the  $Z+1P1F$  region, as the population here already contains  $Z+2jet$  events that underwent a  $\binom{2}{1}$  migration, as there are two selected lepton ‘slots’ for a jet to fake. The flow of these events is diagrammed in 7.8.

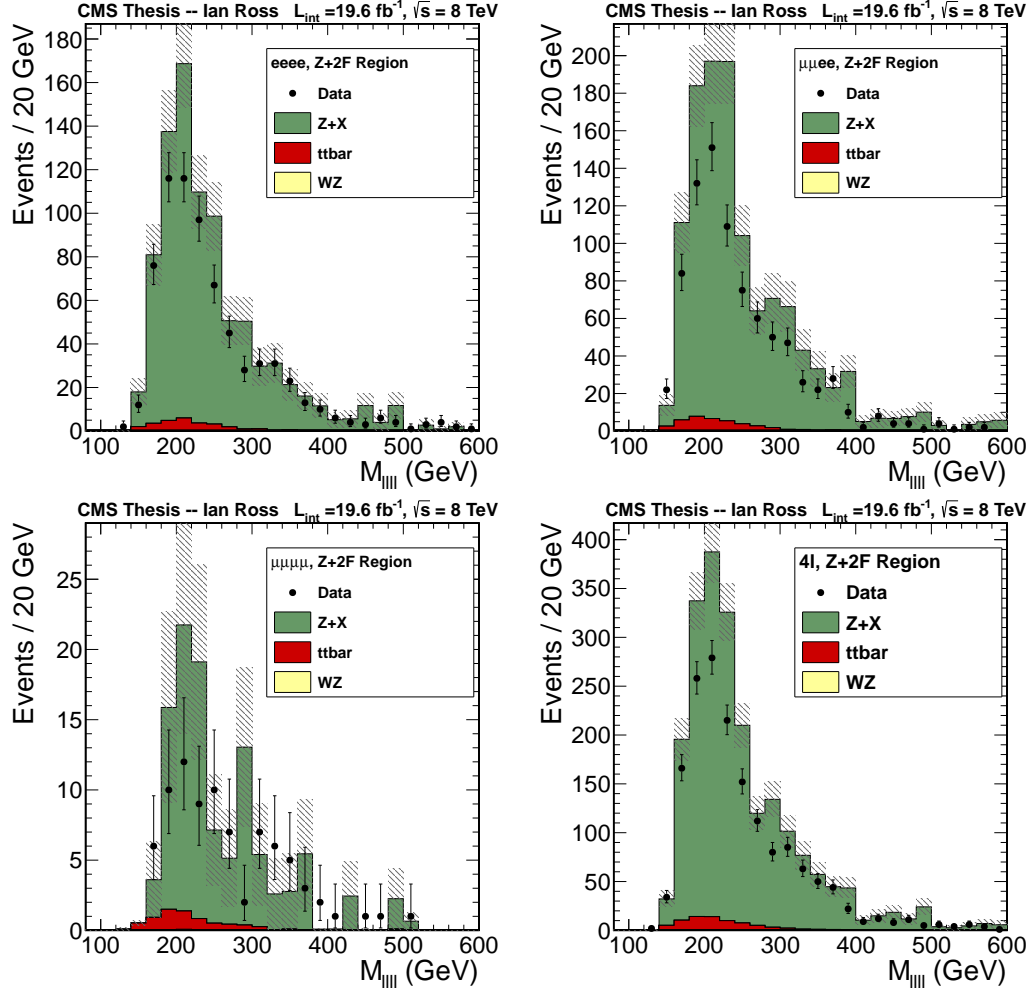


**Figure 7.6:** Background estimation region consisting of a  $Z_0$  plus two failed leptons, with the high mass requirement. Counter clockwise from top right is the  $eeee$ ,  $\mu\mu ee$ ,  $\mu\mu\mu\mu$ , and summed final states.

## 7.5 Final State Radiation Recovery

It is possible for electrons and muons produced in a  $Z$  boson decay to radiate a photon, resulting in a  $Z \rightarrow \ell\ell\gamma$  final state. Because the photons are emitted along an almost equal trajectory, the electron reconstruction process often captures these additional photons. However, it is possible that the electron reconstruction misses the radiated photons and, in addition, no such recovery is inherent to the muons. Given the criticality of precise mass measurements, a final state radiation (FSR) recovery

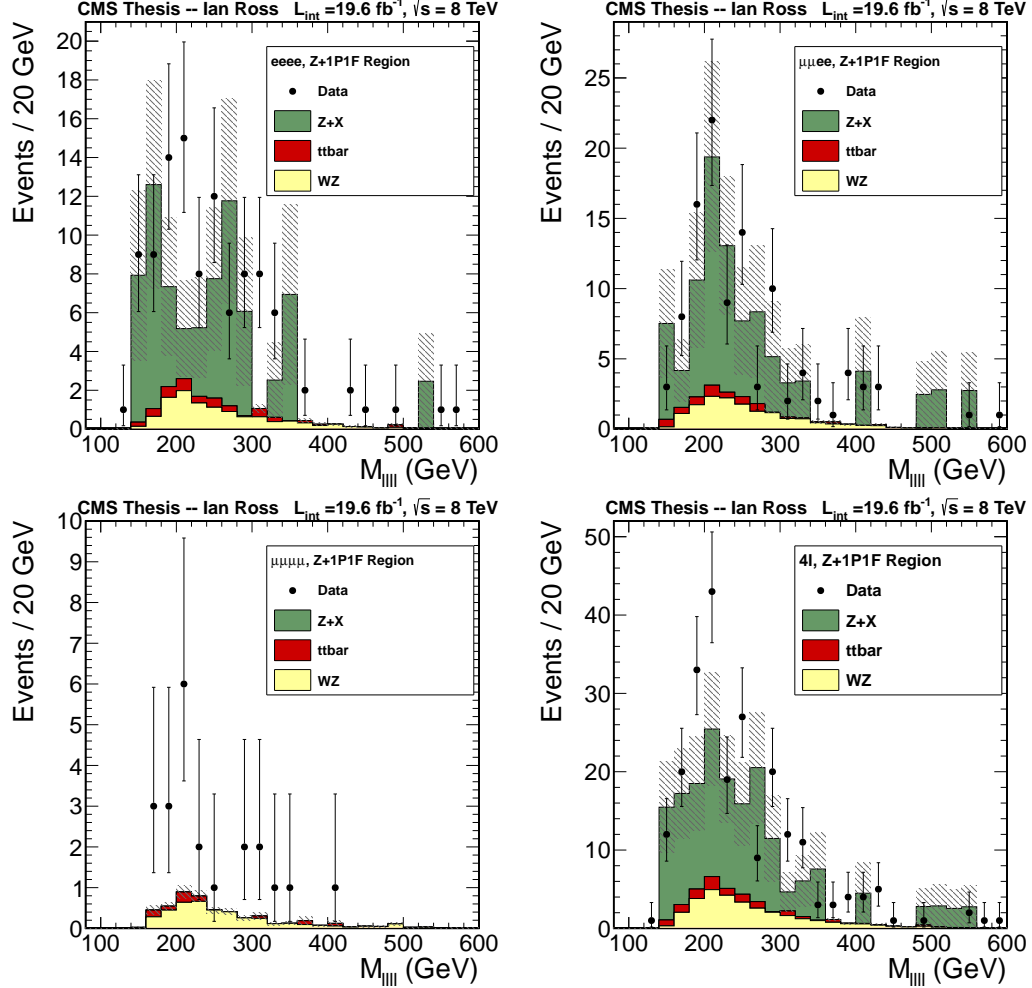


**Figure 7.7:** Background estimation region consisting of a  $Z_0$  plus one passed and one failed leptons, with the high mass requirement. Counter clockwise from top right is the  $eeee$ ,  $\mu\mu ee$ ,  $\mu\mu\mu\mu$ , and summed final states.

algorithm is implemented in order to fully reconstruct the four-momentum of the Z candidates.

The FSR recovery begins by first defining a set of FSR-candidate photons. To start, a collection of photons is built from the Particle Flow photon collection. In addition, photon candidates are built from the electromagnetic calorimeter deposits near Particle Flow muons. The photons are required to have  $p_T > 2$  GeV, within  $|\eta|$  of 2.4, and be well separated from the superclusters of any electrons passing the

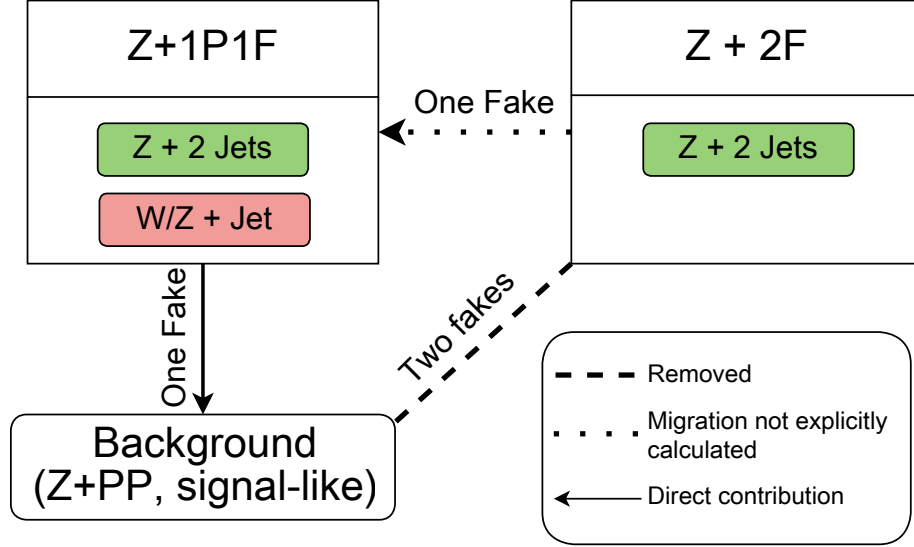


**Figure 7.8:** Diagram depicting the flow of events in the reducible background. A dotted line indicated a migration that does not explicitly enter the background estimate, a solid line indicates a positive net contribution, while a dashed line indicates a removal from the estimate. The “P” and “F” stand for additional loose leptons which pass or fail final selections, respectively.

$p_T$ , identification, and vertex compatibility requirements ( $\Delta R > 0.15$ ,  $\Delta\phi > 2$ , and  $\Delta\eta > 0.05$ ). The isolation for these photons is then computed, using a cone size of  $\Delta R < 0.3$ , with thresholds of 0.2 and 0.5 GeV on the charged and neutral+photon components.

For each photon, the nearest lepton from the Z candidate is found. If the photon is co-linear with the lepton ( $\Delta R(\ell\gamma) < 0.015$ ), then the photon is kept. If the separation between the photon and lepton is wider ( $\Delta R(\ell\gamma) < 0.5$ ), then the photon is kept if its  $p_T$  is above 4 GeV and its relative isolation is less than 1.

Finally, the list of FSR candidate photons is considered with the Z candidate objects. It is important to note that these Z candidates are built from leptons with the isolation criteria not yet applied, as the FSR photon's removal from the leptons' isolation can cause them to migrate from failing to passing the selection. With the four-momenta of the photon summed to that of the Z candidate, the photon is

considered to be a successful recovery if:

- $|M_{\ell\ell\gamma} - M_{Z_0}| < |M_{\ell\ell} - M_{Z_0}|$
- $4 < M_{\ell\ell\gamma} < 100 \text{ GeV}$

If these criteria are met, then the photon is removed from that Z candidate's leptons' isolation cones and the Z ( $\rightarrow \ell\ell\gamma$ ) object is considered to be the Z candidate.

The effects of the FSR recovery can be seen on simulated  $Z_0 \rightarrow ee$  and  $Z_0 \rightarrow \mu\mu$  peaks in Figure 7.9.

## 7.6 Kinematic Discriminant

A kinematic discriminant is introduced in order to utilize the angular differences between  $H \rightarrow ZZ \rightarrow \ell\ell\ell\ell$  and  $ZZ \rightarrow \ell\ell\ell\ell$  decays. Five angles define the angular system in the ZZ rest frame (as pictured in diagram 7.10):

- $\theta_1$  and  $\theta_2$ , the helicity angles defined in each Z's rest frame.
- $\theta^*$ , the production angle of the Z boson with respect to the beam axis
- $\Phi_1$ , the azimuthal angle between the Z1 decay plane and the Z production plane
- $\Phi$ , the angle between the Z1 and Z2 decay planes

The probability that a Higgs (or ZZ) candidate was created with invariant Z masses  $M_{Z1}$  and  $M_{Z2}$  and an angular system defined by the angles  $\vec{\Omega}$  are proportional to their respective elements:

$$P_{signal}(M_{Z1}, M_{Z2}, \vec{\Omega} | M_{\ell\ell\ell\ell}) = |ME_{signal}|^2 \quad (7.8)$$

$$P_{bkg}(M_{Z1}, M_{Z2}, \vec{\Omega} | M_{\ell\ell\ell\ell}) = |ME_{bkg}|^2 \quad (7.9)$$

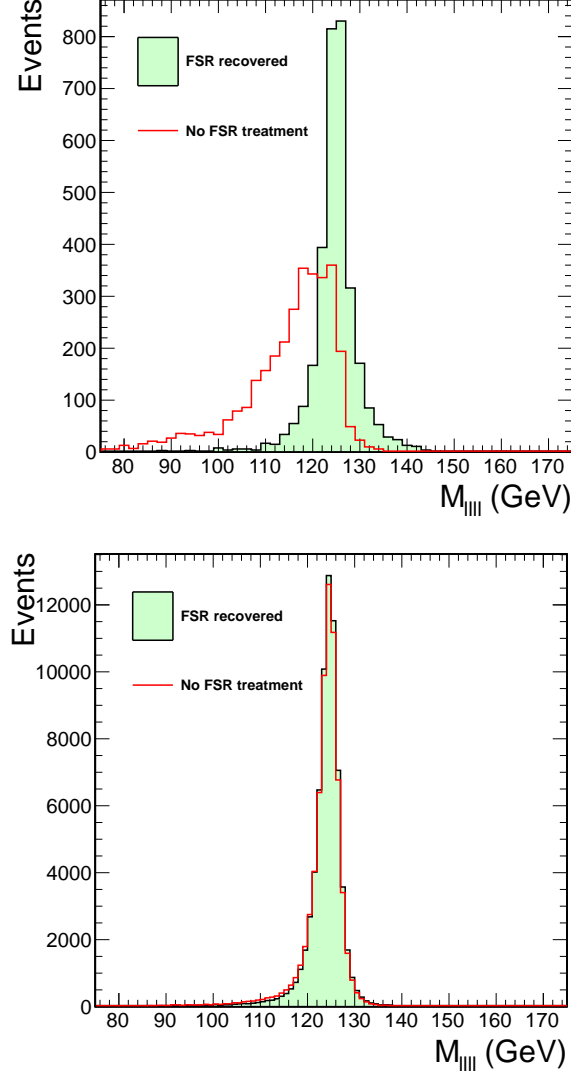


**Figure 7.9:** A simulated  $H \rightarrow 2e2\mu$  ( $m_H = 125\text{GeV}$ ) peak, with and without the FSR recovery. The FSR recover effects only a fraction ( 6% total, top) of the events, but the overall effect (bottom) is a few percent gain in resolution.

A kinematic discriminant can be built to classify events as more or less signal-like:

$$KD = \frac{P_{\text{signal}}}{P_{\text{signal}} + c \cdot P_{\text{bkg}}} = \left( 1 + \frac{c \cdot P_{\text{bkg}}}{P_{\text{signal}}} \right)^{-1} \quad (7.10)$$

This gives a continuously varying discriminant, with background-like events pushed toward 0 and signal-like events near 1.  $P_{\text{bkg}}$  is evaluated using MCFM [71], while JHUGen [72] is used to train the signal samples.

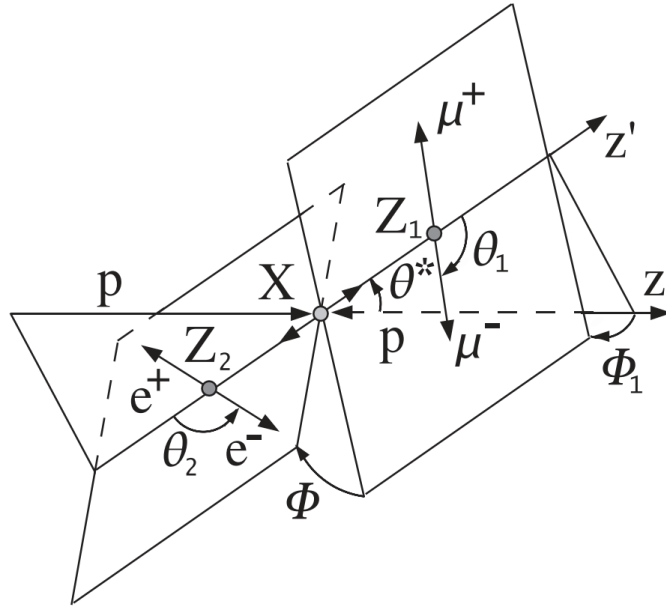


**Figure 7.10:** The angular definitions in the ZZ rest frame.

## 7.7 Final event selection

In order to build the final physics events, the selected leptons must be combined into composite Z candidates, which in term are combined into the final ZZ system. This is done by first combining same-flavor (SF), opposite sign leptons (which pass all identification criteria) into an initial Z candidate. Then the remaining leptons (which pass the loose criteria defined above) are combined into same-flavor combinations. All possible combinations of Z candidate plus SF combinations are stored from the events, allowing easy access to both signal-like events (in which the second candidate passes the tighter criteria and are of opposite sign) and background-like events (in which the second pair of leptons fail the tighter selection and/or are of the same sign).

For both of these sets of Z candidates (both those explicitly passing identification and those that have no restrictions), the FSR recovery is run. This allows the effects

of the FSR state recovery to be properly accounted for in both signal and background-like candidates.

After the FSR recovery, the isolation requirements are placed onto the first Z candidate. Then, selection criteria are applied onto the second Z candidate, sorting the ZZ candidates into signal, Z+1P1F, or Z+2F regions (for both SS and OS secondary pairs).

### 7.7.1 Candidate combinatorics and arbitration

In the  $eeee$  and  $\mu\mu\mu\mu$  final states, the ways in which to combine the opposite-sign, same flavor pairs is ambiguous. Additionally, it is possible that more than four good leptons exist, allowing multiple ZZ candidates to exist within an event. This effect, plus the asymmetric mass selections, on the Z candidates means that some arbitration must be applied. The simplest arbitration is the “best Z mass” selection, in which the  $Z_1$  is defined to be the pair whose invariant mass is closest to the nominal Z mass. Then, from the remaining possible  $Z_2$  candidates, the one with the highest scalar sum of lepton  $p_T$ s is chosen.

The background regions are treated differently. Because each of the candidates represents a possible migration into the signal region, all unique combinations are kept.

### 7.7.2 Signal selection

This analysis considers two separate set of criteria in its two separate searches. The two criteria differ only in the criteria placed on the invariant masses of the Z candidates. The Higgs search necessitates picking up  $Z\gamma^*$  contributions, so a wider

invariant mass range is allowed:

$$\begin{aligned} 40 < M_{Z_1} &< 120 \text{GeV} \\ 12 < M_{Z_2} &< 120 \text{GeV} \end{aligned} \quad (7.11)$$

In the measurements pertaining to the anomalous triple gauge couplings and ZZ differential cross sections, both  $Z_0$  bosons are required to be on-shell, eliminating the contributions from  $\gamma^*$  production:

$$\begin{aligned} 60 < M_{Z_1} &< 120 \text{GeV} \\ 60 < M_{Z_2} &< 120 \text{GeV} \end{aligned} \quad (7.12)$$

The Higgs search (the so-called low-mass criteria) and the Standard Model/triple gauge coupling measurements (the high-mass criteria) differ only in the mass requirements listed in equations 7.11 and 7.12.

## 7.8 Signal and background modelling

In the search for a Standard Model Higgs boson, the differential distribution (with respect to the four-lepton invariant mass) is factorized as:

$$\frac{dN}{dM_{\ell\ell\ell\ell}} = C_\epsilon \cdot N^{MC}(m_H) \cdot F_H(M_{\ell\ell\ell\ell}|m_H) \quad (7.13)$$

where  $C_\epsilon$  is the product of the leptonic correction factors (described in section 7.2.5),  $m_H$  is the hypothesized Higgs boson mass, and  $F_H$  is the probability density function of the Higgs mass distribution. This function is a convolution of a relativistic Breit-

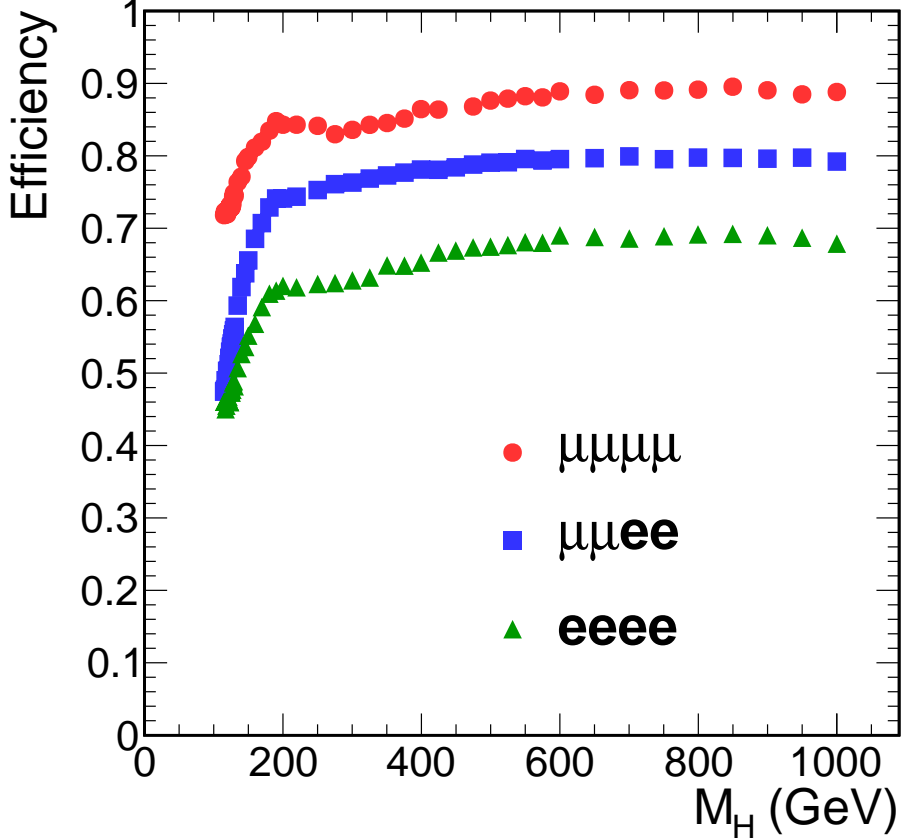


**Figure 7.11:** Final selection efficiency for each final state, as a function of the Higgs mass. Efficiency is defined as the number of selected events to the number of events produced within the geometrical and kinematic requirements of the analysis.

Wigner function <sup>1</sup> with a double Crystal Ball function <sup>2</sup>, added to account for the low- and high-side tails from bremsstrahlung effects and detector mismeasurement effects. The shape parameters are fit using the available Monte Carlo simulation samples, then a secondary fit to the shape parameters is used in extracting shape values between the generated samples. This allows a smoothly varying shape to be

---


$$\begin{aligned}
 & \frac{\Gamma_{gg}(m_{4\ell}) \cdot \Gamma_Z Z(m_{4\ell}) \cdot m_{4\ell}}{(m_{4\ell}^2 - m_H^2)^2 + m_{4\ell}^2 \cdot \Gamma^2(m_{4\ell})} \\
 & \times \begin{cases} A \cdot (B + |\xi|)^{-n_L} & \text{for } \xi < \alpha_L \\ A \cdot (B + |\xi|)^{-n_R} & \text{for } \xi > \alpha_R \\ \exp(-\xi^2/2), & \text{for } \alpha_L \leq \xi \leq \alpha_R \end{cases} \\
 & \xi = (m_{4\ell} - m_H - \Delta m_H)/\sigma_m
 \end{cases}$$

used as input across an arbitrary Higgs mass hypothesis range. A full description of the shape and its parameters is given in [73].

For a low ( $< 400 \text{ GeV}$ ) mass Higgs hypothesis, the implicit zero-width assumption used in the fitting procedure above holds valid. However, as the Higgs width becomes wider, this assumption breaks down. As a result, all cross sections and lineshapes in the high-mass Higgs hypotheses utilize the *Complex Pole Scheme (CPS)* [74]. Additionally, interference between Higgs and  $gg \rightarrow ZZ$  production causes a significant deformation in the invariant mass distribution. This is corrected (and uncertainties computed) using the scheme proposed in [75]. The uncertainties are explained in Section 7.9.

In the Higgs search, the ZZ background is treated in a way similar to the Higgs signal (Eqn.7.13). However the shape,  $F_H$ , is replaced by:

$$\begin{aligned} \frac{dN_{qq \rightarrow ZZ}}{dM_{\ell\ell\ell\ell}} &= C_\epsilon \cdot N^{MC}(m_H) \cdot (f_1 + f_2 + f_3) \\ \frac{dN_{gg \rightarrow ZZ}}{dM_{\ell\ell\ell\ell}} &= C_\epsilon \cdot N^{MC}(m_H) \cdot (f_1 + f_2) \\ f_1(m, \vec{a}) &= \left( 0.5 + 0.5 \operatorname{erf}\left(\frac{m - a_1}{a_2}\right) \right) \cdot \frac{a_4}{1 + \exp(m - a_1)/a_3} \\ f_2(m, \vec{b}) &= \left( 0.5 + 0.5 \operatorname{erf}\left(\frac{m - b_1}{b_2}\right) \right) \cdot \left( \frac{b_4}{1 + \exp(m - b_1)/b_3} + \frac{b_6}{1 + \exp(m - b_1)/b_5} \right) \\ f_3(m, \vec{c}) &= \left( 0.5 + 0.5 \operatorname{erf}\left(\frac{m - c_1}{c_2}\right) \right) \cdot \frac{c_4}{1 + \exp(m - c_1)/c_3} \end{aligned} \quad (7.14)$$

## 7.9 Systematic Uncertainties

### 7.9.1 Higgs Signal Simulation

Systematic uncertainties for the Higgs samples effect either the overall yield or the shape of the signal. Uncertainties that enter only through the yield include:

- Uncertainty on Higgs production cross section,  $H \rightarrow ZZ$ , and  $ZZ \rightarrow 4\ell$  branching ratios.
- Uncertainty on acceptance measurements
- Uncertainties on data-to-MC correction factors

while uncertainties that impact the signal shape are:

- The theoretical uncertainties in the pdf of the Higgs shape,  $F_H(M_{\ell\ell\ell\ell}|m_H)$
- Uncertainties in the modelling of detector effects within the double Crystal ball fit

The uncertainty on the Higgs production cross section arises from the PDF and  $\alpha_s$  (the strong force coupling strength) errors in addition to uncertainties in the QCD renormalization ( $\mu_R$ ) and factorization ( $\mu_F$ ) scales (which are theoretical constructs to remove divergent cross section calculations). These values, in addition to the cross sections themselves, are provided by the LHC working group [76]. Effects due to the acceptance are measured using MCFM, adjusting  $\mu_R$  and  $\mu_F$  up and down by a factor of two and calculating the total change in acceptance. These uncertainties are found to be at the 0.1-0.2% level, and are neglected. PDF and  $\alpha_s$  effects on the acceptance are measured using the PDF4LHC prescription [77], in which three different PDF sets are used ([43], [42], [44]), with the maximum differences being the final systematic effect. This is found to be a fairly flat effect across all Higgs masses, and a flat 2% systematic is applied.

Shape systematic uncertainties are measured by utilizing alternate shape hypotheses, refitting the samples, and taking the envelope of the outcomes as the systematic error.

The data-to-MC scale factors corrections, obtained from the tag and probe method outlined in Section 7.2.5, are applied on a per-lepton basis. Each lepton provides an additional weight factor that is applied when extracting the Monte Carlo yield. Uncertainties in the correction factor measurements (coming from shape and modelling uncertainties in the tag and probe process) are propagated into a final uncertainty by running, for each MC sample, a batch of 500 toy MC experiments. For each, the correction factor is extracted via a Gaussian, centered at the data/MC ratio and with a  $\sigma$  equal to the associated error. The final systematic uncertainty on the MC yields is defined to be the RMS of the distribution of these pseudoexperiments.

### 7.9.2 ZZ Simulation

Many of the systematic uncertainties on ZZ are similar to those for the Higgs signal. Uncertainties on the total yields are due primarily to the theoretical uncertainties, PDF+ $\alpha_s$  and QCD scales, and the instrumental uncertainties on the data-MC scaling.

PDF+ $\alpha_s$  uncertainties are again evaluated using the PDF4LHC method, as with the Higgs sample. The  $qq \rightarrow ZZ$  and  $gg \rightarrow ZZ$  errors are evaluated separately, and vary roughly with the square root of the  $M_{\ell\ell\ell\ell}$ :

$$\begin{aligned} qq \rightarrow ZZ : \kappa(M_{\ell\ell\ell\ell}) &= 1 + 0.0035\sqrt{M_{\ell\ell\ell\ell} - 30} \\ gg \rightarrow ZZ : \kappa(M_{\ell\ell\ell\ell}) &= 1 + 0.0066\sqrt{M_{\ell\ell\ell\ell} - 10} \end{aligned} \quad (7.15)$$

QCD scale uncertainties are treated the same way, measuring the envelope of errors resulting from scaling  $\mu_F$  and  $\mu_R$ , with uncertainties parameterized as:

$$\begin{aligned} qq \rightarrow ZZ : \kappa(M_{\ell\ell\ell\ell}) &= 1.00 + 0.01\sqrt{(M_{\ell\ell\ell\ell} - 20)/13} \\ gg \rightarrow ZZ : \kappa(M_{\ell\ell\ell\ell}) &= 1.04 + 0.10\sqrt{(M_{\ell\ell\ell\ell} + 40)/40} \end{aligned}$$

### 7.9.3 Systematic Uncertainties on Reducible Backgrounds

The uncertainties on the reducible background estimates come primarily from the limited statistics in the regions where fake rates are applied, the uncertainties in the measured fake rates, and the uncertainty in the difference in background sources while migrating between the regions. MC closure tests and OS/SS checks were conducted, but were limited by statistics. Alternate reducible BG calculations were conducted, and a conservative estimate of 30-50% was applied (depending on the final state).

### 7.9.4 Global Uncertainties in MC-driven estimates

In addition to the uncertainties outlined above, there are two global effects which impact the yield extraction from the Monte Carlo simulated samples. First, uncertainties in the measurement in the integrated luminosity were found to be 4.4% [78]. Additionally, the uncertainty on the trigger corrections (which come from tag and probe measurements) is evaluated to 1.5% [65].

## 7.10 Summary

The selection criteria for the search of a  $ZZ \rightarrow \ell\ell\ell\ell$  final state is designed to be as loose as possible in order to maximize the efficiency of this clean, though low-probability, final state. The final selection criteria on electrons, muons, and Z boson candidates are summarized in Table 7.5.

Additionally, careful consideration of systematic uncertainties, both on expected yields and shapes of signals and background, have been evaluated. These uncertainties are summarized in Table 7.6.

| Electron selection   |  |
|--|--|
| Kinematics<br>Identification<br>Isolation                          | $p_T > 7 \text{ GeV}$ , $ \eta  < 2.5$<br>MVA ID as defined above.<br>$\rho$ -corrected relative isolation $\geq 0.40$                   |
| Muon selection   |  |
| Kinematics<br>Identification<br>Isolation                          | $p_T > 5 \text{ GeV}$ , $ \eta  < 2.4$<br>(Global OR Tracker), PF Muon<br>$\rho$ -corrected relative isolation $\geq 0.40$               |
| Z Candidate Selections   |  |
| Higgs search (low-mass)<br><br>SM ZZ and aTGC analysis (high-mass) | $40 < M_{Z1} < 120 \text{ GeV}$<br>$12 < M_{Z2} < 120 \text{ GeV}$<br>$60 < M_{Z1} < 120 \text{ GeV}$<br>$60 < M_{Z2} < 120 \text{ GeV}$ |

**Table 7.5:** Summary of the selection criteria.

|                               | ggH     | VBF     | WH    | ZH     | ttH   | qqZZ    | ggZZ  |
|-------------------------------|---------|---------|-------|--------|-------|---------|-------|
| gg pdf uncertainty            | 7.2-9.2 | -       | -     | -      | 0-9.8 | -       | 10    |
| $qq/q\bar{q}$ pdf uncertainty | -       | 1.2-1.8 | 0-4.5 | 0-5.0  | -     | 5       | -     |
| QCD Scale                     | 5.5-7.9 | 0.1-0.2 | 0-0.6 | 9-1.5  | 0-8.8 | 2.6-6.7 | 24-44 |
| $H \rightarrow 4l$ BR         | 2       | 2       | 2     | 2      | 2     | -       | -     |
| CB mean parameterization      |         |         | 0.4   |        |       | -       | -     |
| CB $\sigma$ parameterization  |         |         | 20    |        |       | -       | -     |
| CB $\alpha$ parameterization  |         |         | 20    |        |       | -       | -     |
| Luminosity                    |         |         |       | 4.2    |       |         |       |
| Trigger                       |         |         |       | 1.5    |       |         |       |
| Electron efficiency scale     |         |         |       | 6.2-11 |       |         |       |
| Muon efficiency scale         |         |         |       | 1.9    |       |         |       |

**Table 7.6:** Summary of the systematic uncertainties.

# Chapter 8

## Results

The analysis presented in this analysis is split into two selection criteria, differing only by an on-shell ( $60 < M_Z < 120 \text{ GeV}$ ) requirement placed on the Standard Model ZZ production and anomalous triple gauge coupling search. The search for a Standard Model Higgs boson requires an off-shell Z boson, so for this portion of the analysis, the Z candidate invariant mass requirements are loosened to  $40 < M_{Z1} < 120$  and  $12 < M_{Z2} < 120$ .

### 8.1 Standard Model ZZ Production

Yields for the on-shell selection criteria are presented in Table 8.1. The four-lepton invariant mass for each final state is shown in Figure 8.1.

|                | eeee                      | $\mu\mu\mu\mu$             | $\mu\mu ee$                 |
|----------------|---------------------------|----------------------------|-----------------------------|
| ZZ             | $55.28 \pm 0.25 \pm 7.64$ | $77.32 \pm 0.29 \pm 10.08$ | $136.09 \pm 0.59 \pm 17.50$ |
| Z+Jets         | $2.15 \pm 0.26 \pm 0.88$  | $1.19 \pm 0.35 \pm 0.48$   | $2.35 \pm 0.34 \pm 0.93$    |
| Total Expected | $57.43 \pm 0.37 \pm 7.69$ | $78.51 \pm 0.49 \pm 10.09$ | $138.44 \pm 0.70 \pm 17.52$ |
| Observed       | 54                        | 75                         | 148                         |

**Table 8.1:** Final yields per event channel in the high-mass analysis (ZZ Production cross-section and anomalous triple gauge coupling search). Errors are statistical  $\pm$  systematic.

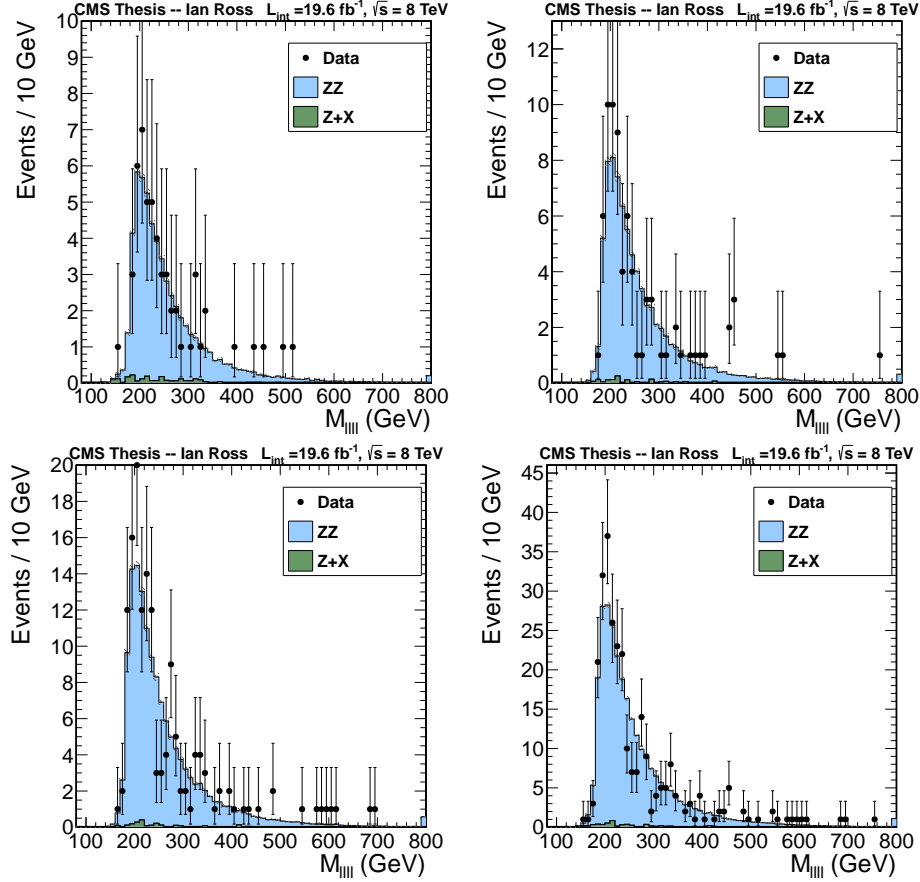


**Figure 8.1:** ZZ invariant mass for the high-mass analysis, across the full considered  $M_{eeee}$  range. Pictured are the  $eeee$ ,  $\mu\mu\mu\mu$ ,  $\mu\mu ee$ , and combined total results (upper left, upper right, lower left, and lower right respectively).

### 8.1.1 Cross section measurement

The first step of the statistical analysis is to define a likelihood function. Because we are dealing with a counting experiment in each bin, the natural basis to use is the Poisson distribution:

$$f(k; \lambda) = \frac{\lambda^k e^{-\lambda}}{k!} \quad (8.1)$$

Where  $f(k; \lambda)$  is the probability of observing  $k$  events, given an expectation of  $\lambda$ . In the case of a physics search,  $k$  can be defined as:

$$k = \mu s(\vec{\theta}_s) + b(\vec{\theta}_b) \quad (8.2)$$

where  $\mu$  is a strength modifier (interpreted as  $\sigma_{measured}/\sigma_{SM}$ ) on the expected signal,  $s$ , and  $b$  is the expected background.  $\vec{\theta}_s$  and  $\vec{\theta}_b$  are the nuisance parameters associated with the signal and background. These nuisance parameters enter the expected yields as log-normal constraints. The total likelihood, then, is the product of the Poissonian distribution, across all bins of the histogram:

$$L(\mu, \vec{\theta}_s, \vec{\theta}_b) = \prod f_i(k_i; \lambda_i(\mu, \vec{\theta}_s, \vec{\theta}_b)) \quad (8.3)$$

The ZZ production cross section is extracted via a simultaneous fit to a likelihood built from each of the final states. For the case of cross section extraction, a global counting experiment is used (meaning there is just one bin considered in Eqn. 8.3 for each final state).

By maximizing the likelihood function as a function of the signal strength modifier,  $\mu$ , one can extract the measured cross section. After removing the branching ratio of the Z decays into leptons, the ZZ production cross section is measured as:

$$\sigma(pp \rightarrow ZZ) = 7.7^{+0.5}_{-0.5}(stat.)^{+0.6}_{-0.5}(sys.) \pm 0.3(\text{lumi})\text{pb} \quad (8.4)$$

which agrees favorably with the Standard Model prediction (from MCFM [71]) of  $7.7 \pm 0.6$  pb. The cross section is also measured using each channel individually. These results are shown in table 8.2.

| Final State    | $\sigma(pp \rightarrow ZZ)$  |
|----------------|--|
| $\mu\mu\mu\mu$ | $7.3^{+0.8}_{-0.8}(stat.)^{+0.7}_{-0.6}(sys.) \pm 0.3(\text{lumi})\text{pb}$ |
| eeee           | $7.2^{+1.0}_{-0.9}(stat.)^{+0.7}_{-0.6}(sys.) \pm 0.3(\text{lumi})\text{pb}$ |
| $\mu\mu ee$    | $8.1^{+0.7}_{-0.6}(stat.)^{+0.7}_{-0.6}(sys.) \pm 0.4(\text{lumi})\text{pb}$ |
| Combined       | $7.7^{+0.5}_{-0.5}(stat.)^{+0.6}_{-0.5}(sys.) \pm 0.3(\text{lumi})\text{pb}$ |

**Table 8.2:**  $ZZ$  production cross section measurements for each of the final states considered and combined.

### 8.1.2 Unfolding

In order to remove detector effects from the differential cross sections, the distributions are *unfolded*. The procedure followed within this analysis is the iterative Bayesian method, outlined by D'Agostini [79].

The measured distribution of a variable is assumed to be a convolved mixture of the underlying “true” distribution and the smearing and distortion resulting by imperfect detector elements. Specifically, the measured distribution,  $M$ , is related to the true distribution  $T$ , through a response matrix,  $R$ :

$$M_i = \sum_j R_{ij} T_j \quad (8.5)$$

The response matrix,  $R$ , is trained with a Monte Carlo sample, passing the generated and reconstructed values from each event into the corresponding (true value, reconstructed value) bin. Bayes' theorem is then applied to the elements, using a flat prior, to give the probability of a true value from bin  $i$ , given an observation in bin  $j$ :

$$P(T_i|M_j) = \frac{P(M_j|T_i)P_0(T_i)}{\sum_{l=1}^{nbins} P(M_j|T_l)P_0(T_l)} \quad (8.6)$$

And the estimate for the number of true events in bin  $i$ , is

$$n_i = \frac{1}{\epsilon_i} \sum_{j=1}^{nbinsreco} n_j P(T_i|M_j) \quad (8.7)$$

where  $\epsilon_i$  is the overall efficiency for reconstructing an event originating in bin  $i$  and  $n_j$  is the total number of events observed in bin  $j$ . The prior probability,  $P_0$  is initially assumed to be flat. However, an iterative process is used while training, recursively updating the prior until the predicted and actual true distributions match reasonably well.

The CMS detector has, on the whole, excellent electron and muon resolution, and as a result there is a limited amount of bin-to-bin migration. A qualitative example of the unfolded vs. uncorrected distributions are shown in figure 8.3. Migrations between bins are slight overall, as are the resulting effects of the unfolding. This suggests that the overall detector resolution is excellent, in both position and momenta measurements, for the objects utilized in the analysis. Final unfolded differential distributions are presented in Figures 8.4, 8.5, 8.6, and 8.7.

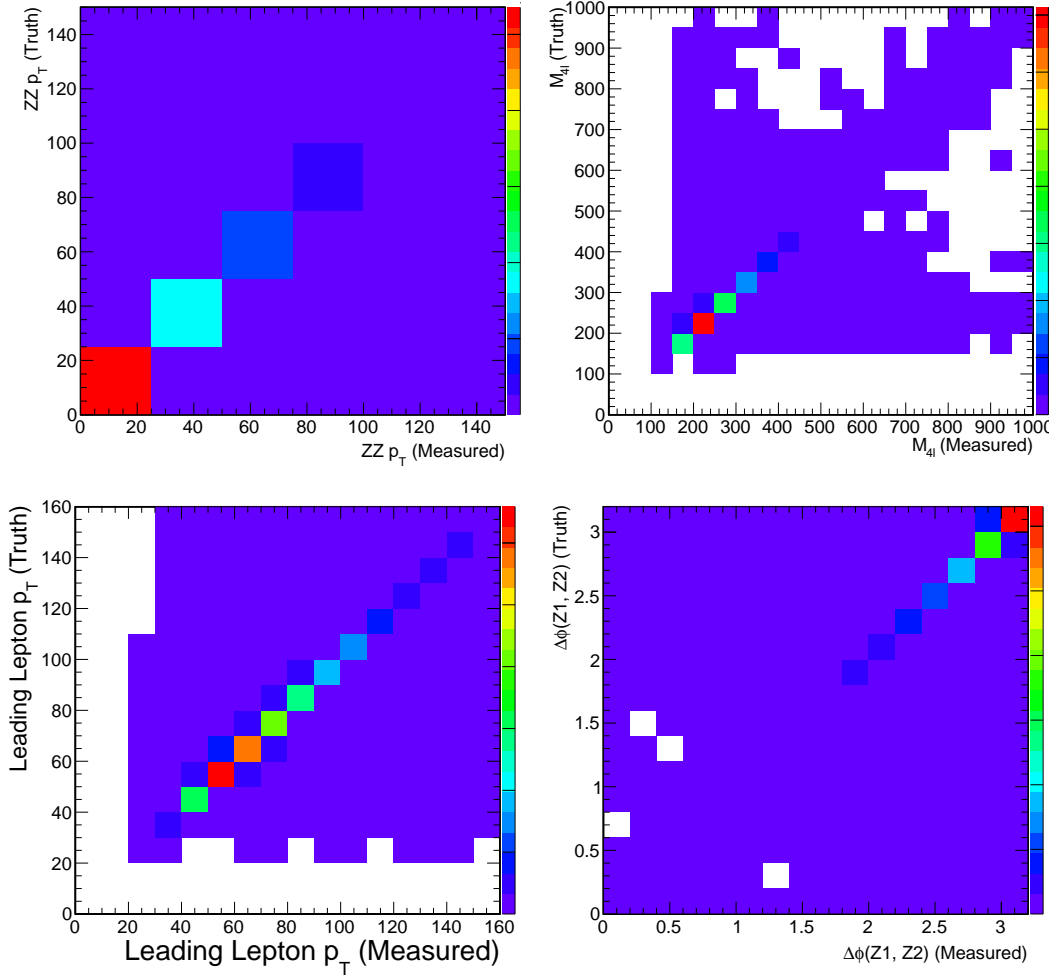


**Figure 8.2:** Example response matrices used in the unfolding process. Pictured, clockwise from the top left, are the four-lepton  $p_T$ , four-lepton mass, leading lepton  $p_T$ , and azimuthal separation between the  $Z$  bosons. The primarily diagonal nature indicates a limited number of migrations, due to the excellent detector resolutions.

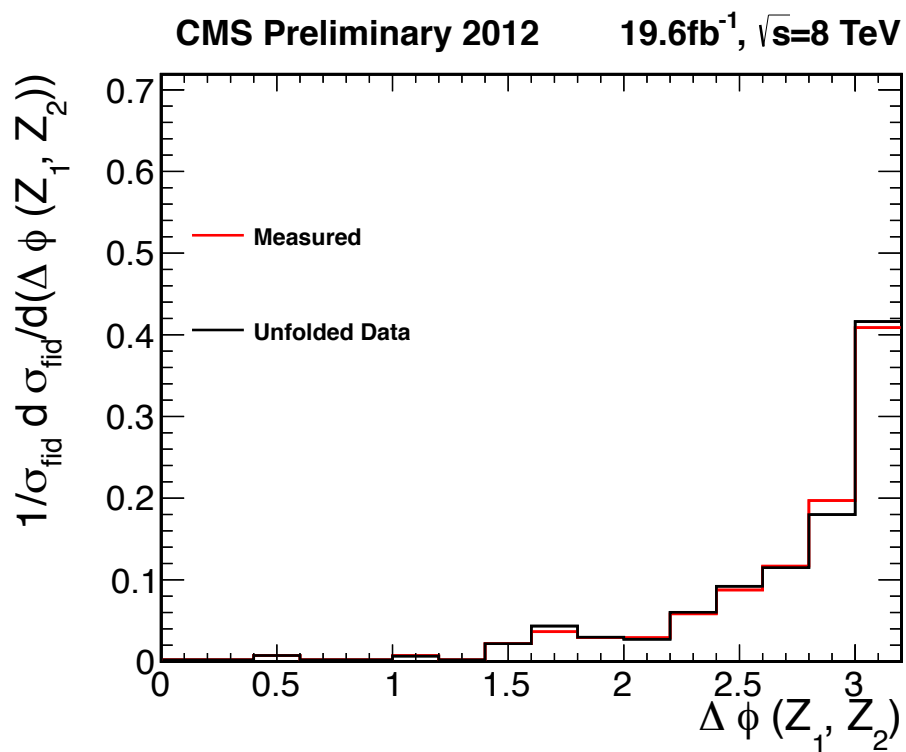


**Figure 8.3:** An example of the effects of unfolding. The  $\Delta\phi$  separation between  $Z$  candidates is relatively unchanged by the unfolding (red, measured, and black, unfolded, are nearly identical).

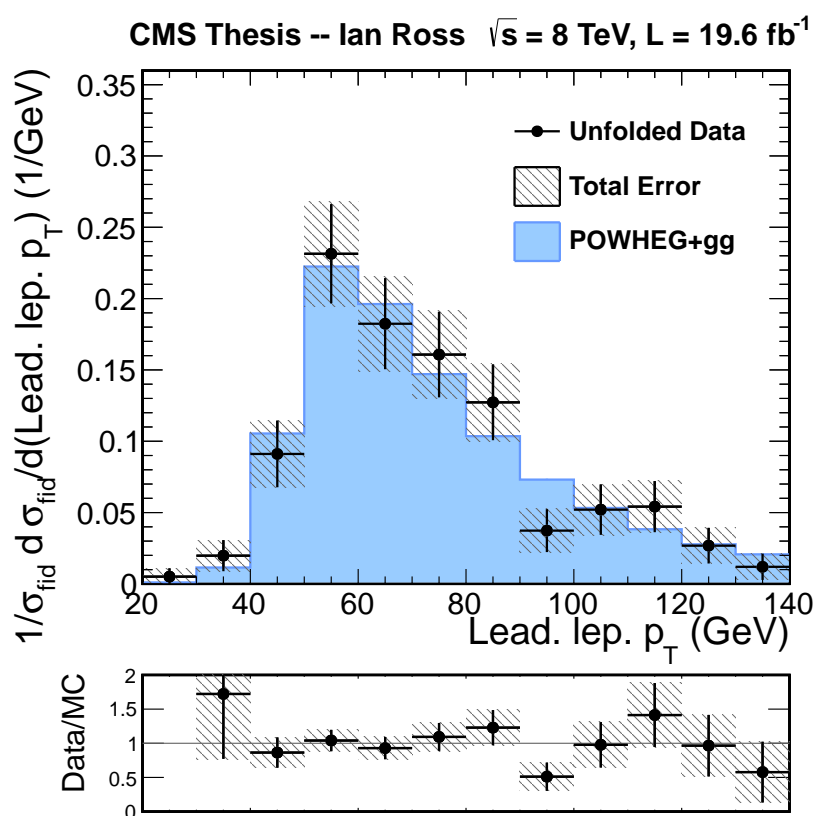


**Figure 8.4:** Unfolded distribution of the highest lepton  $p_T$ .

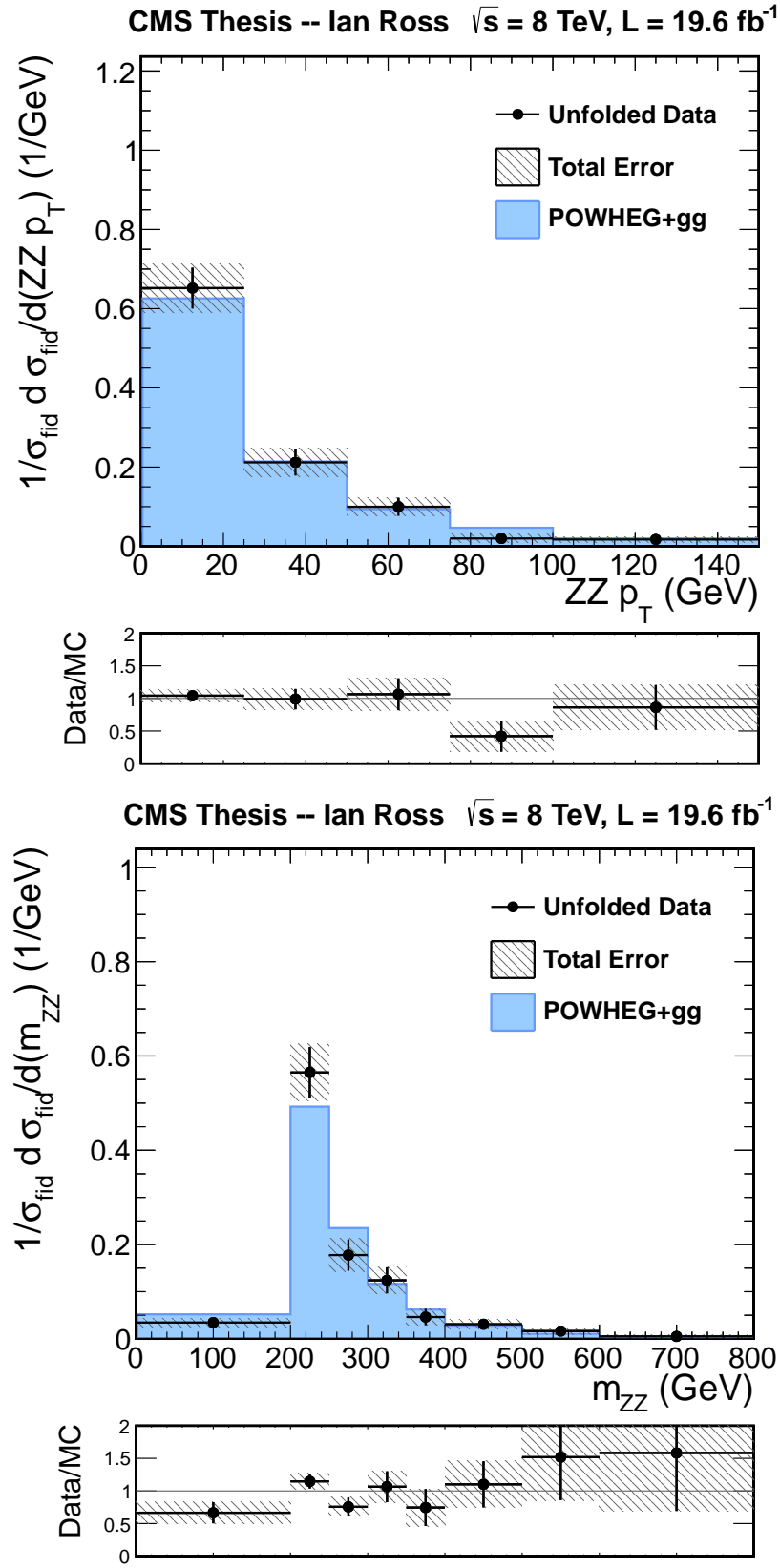


**Figure 8.5:** Unfolded ZZ kinematic variables. The ZZ system  $p_T$  (top) and  $M_{\ell\ell\ell\ell}$  (bottom).

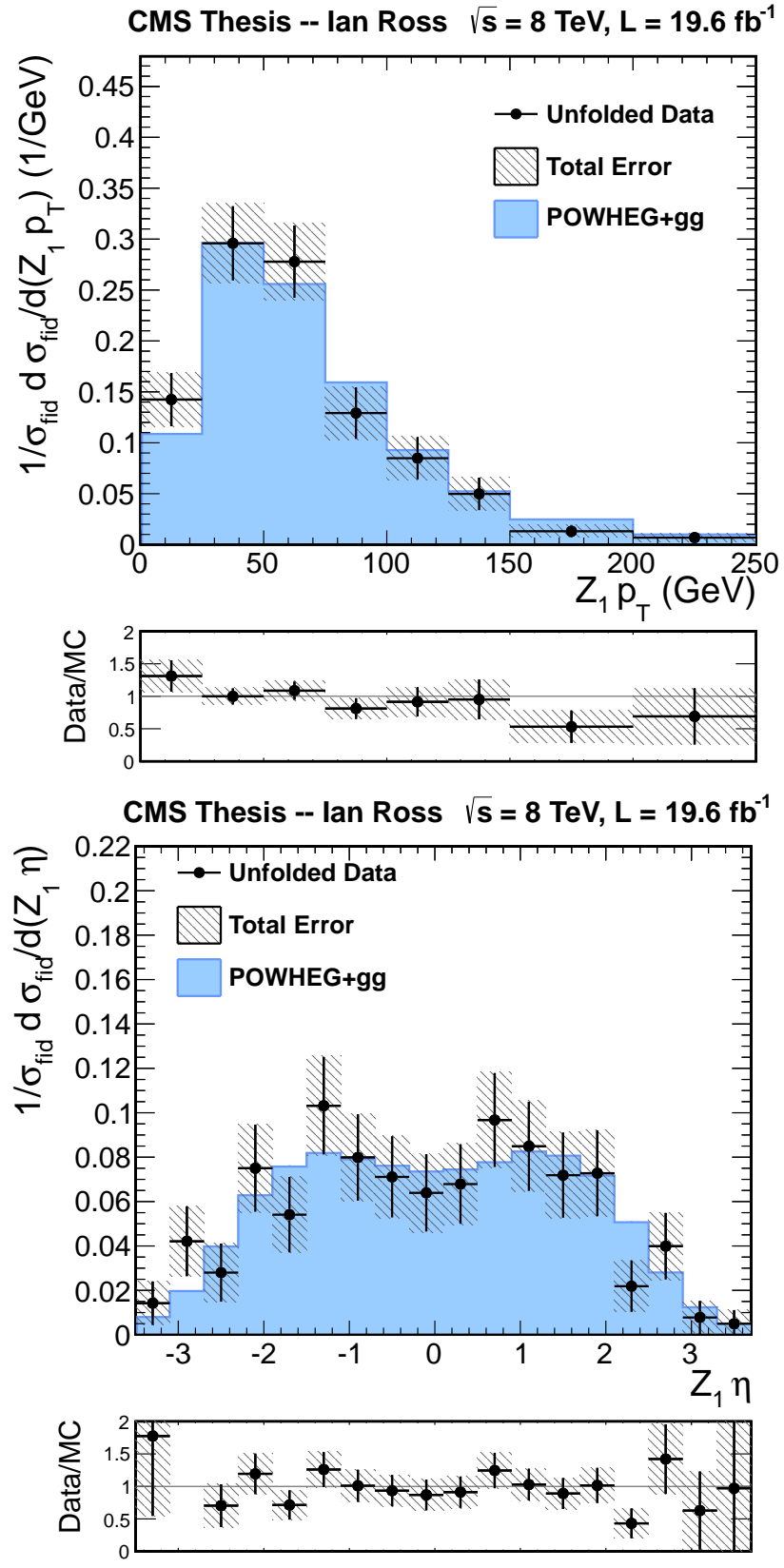


**Figure 8.6:** Unfolded leading (in  $p_T$ ) kinematic variables. The unfolded  $Z$  system  $p_T$  (top) and  $\eta$  (bottom) distributions.

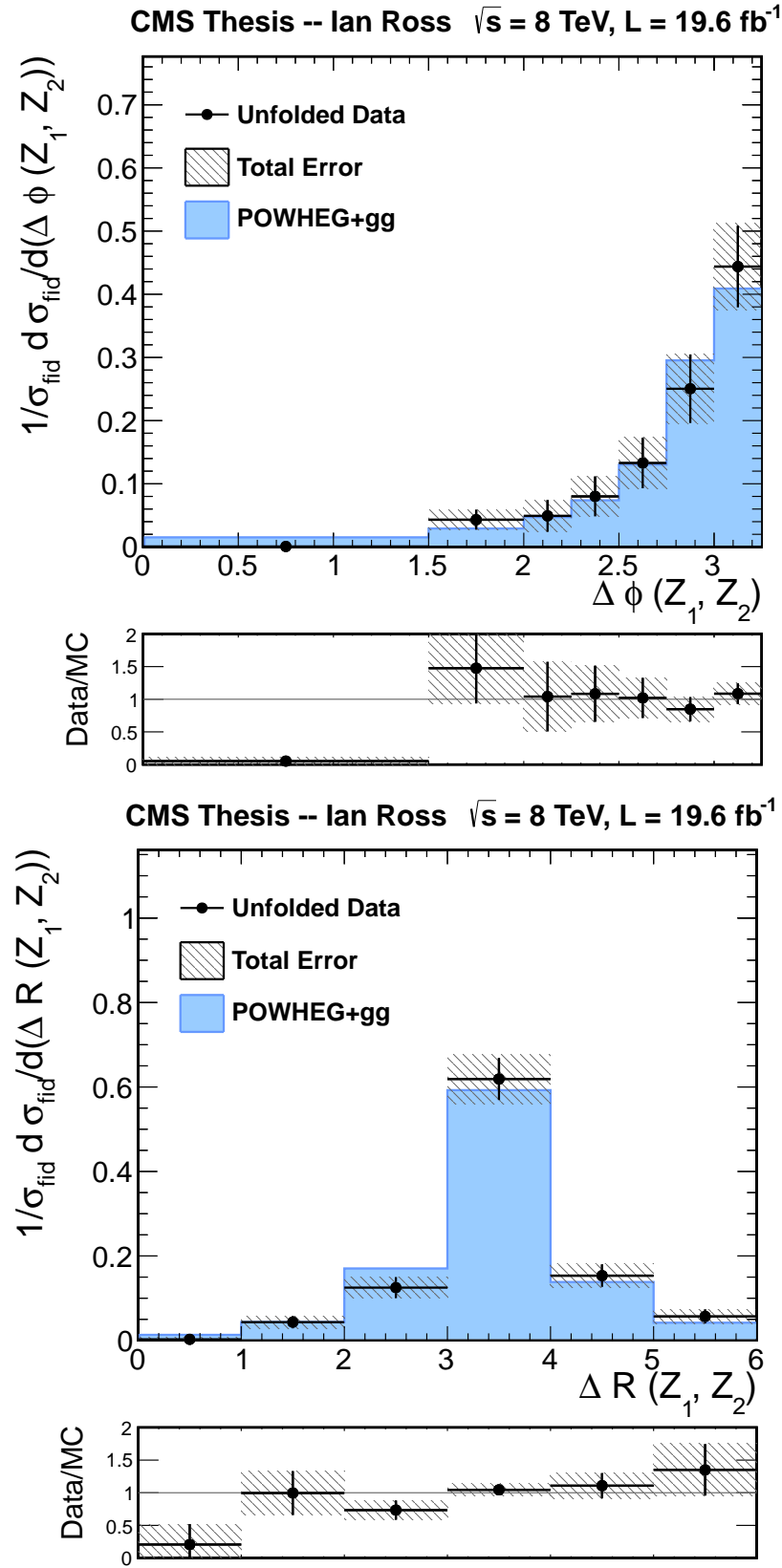


**Figure 8.7:** Unfolded distribution of the  $Z$  candidate separations,  $\Delta\phi$  top and  $\Delta R$  bottom.

## 8.2 Search for a Standard Model Higgs Boson

Overall yields for the low-mass (Higgs search) analysis are presented in Table 8.3. The observed four-lepton invariant mass across the entire mass range is presented in Figure 8.8. A significant excess is observed in the vicinity of 126 GeV, and this region is shown in finer binning in Figure 8.9.

|             | eeee             | $\mu\mu\mu\mu$    | $\mu\mu ee$       |
|-------------|------------------|-------------------|-------------------|
| H(126)      | $2.86 \pm 0.03$  | $5.49 \pm 0.05$   | $7.92 \pm 0.06$   |
| H(350)      | $11.65 \pm 0.09$ | $15.80 \pm 0.11$  | $27.89 \pm 0.15$  |
| ZZ          | $68.21 \pm 0.29$ | $101.58 \pm 0.39$ | $167.32 \pm 0.66$ |
| Z+Jets      | $6.70 \pm 0.49$  | $3.46 \pm 0.78$   | $7.82 \pm 0.80$   |
| BG Expected | 74.91            | 105.04            | 175.14            |
| Observed    | 73               | 109               | 194               |

**Table 8.3:** Final yields per event channel in the low-mass analysis (search for the Higgs boson). Errors are statistical only.

### 8.2.1 Statistical Analysis

A test statistic,  $q_\mu$ , based on the likelihood function defined in 8.3, is defined to extract upper limits:

$$\tilde{q}_\mu = -2 \ln \frac{L(\mu, \vec{\theta}_{s\mu}, \vec{\theta}_{b\mu})}{L(\hat{\mu}, \hat{\vec{\theta}}_s, \hat{\vec{\theta}}_b)} \quad (8.8)$$

where  $\hat{\theta}_{i\mu}$  are the conditional maximum likelihood estimators, and  $\hat{\mu}$ ,  $\hat{\theta}_s$ , and  $\hat{\theta}_b$  are the parameters which maximize the global likelihood. From here, probability density functions are built for signal-plus-background and background-only hypotheses. From these, p-values for the both scenarios are calculated:

$$p_\mu = P(\tilde{q}_\mu \geq \tilde{q}_\mu^{obs} | \text{signal+background}) \quad (8.9)$$

$$1 - p_b = P(\tilde{q}_\mu \geq \tilde{q}_\mu^{obs} | \text{background only}) \quad (8.10)$$

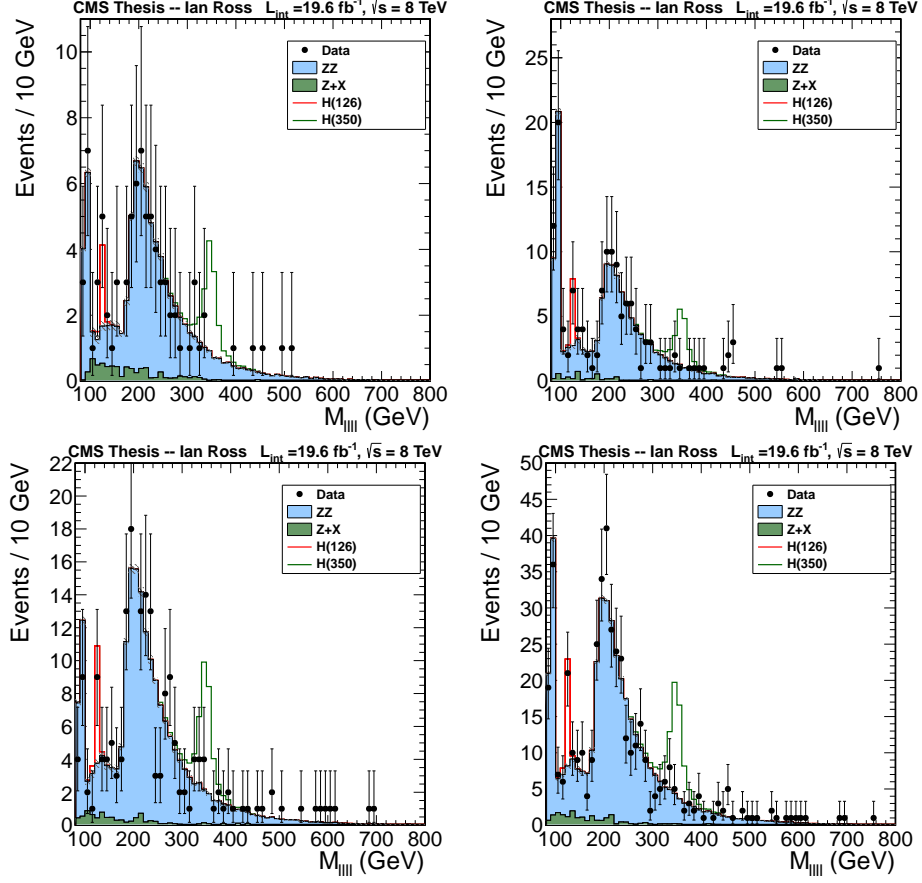


**Figure 8.8:** ZZ invariant mass for the low-mass analysis, across the full considered  $M_{\ell\ell\ell\ell}$  range. Pictured are the  $\ell\ell\ell\ell$ ,  $\mu\mu\mu\mu$ ,  $\mu\mu e e$ , and combined total results (upper left, upper right, lower left, and lower right respectively).

corresponding to the probability of observing a test statistic at least as large as that observed, given a signal-plus-background or background only hypothesis. Finally, the CLs value is defined to be the ratio between these probabilities:

$$CLs = \frac{p_\mu}{1 - p_b} \quad (8.11)$$

The CLs value has the property that, given a value of  $\mu$  and CLs value  $\leq \alpha$ , a Higgs of that signal strength is excluded at the  $1 - \alpha$  confidence level. Thus, to set a 95% confidence level upper limit, the value of  $\mu$  is adjusted until the CLs value is 0.05.

Similarly, in order to find the significance of an observation, a test statistic  $q_0$  is

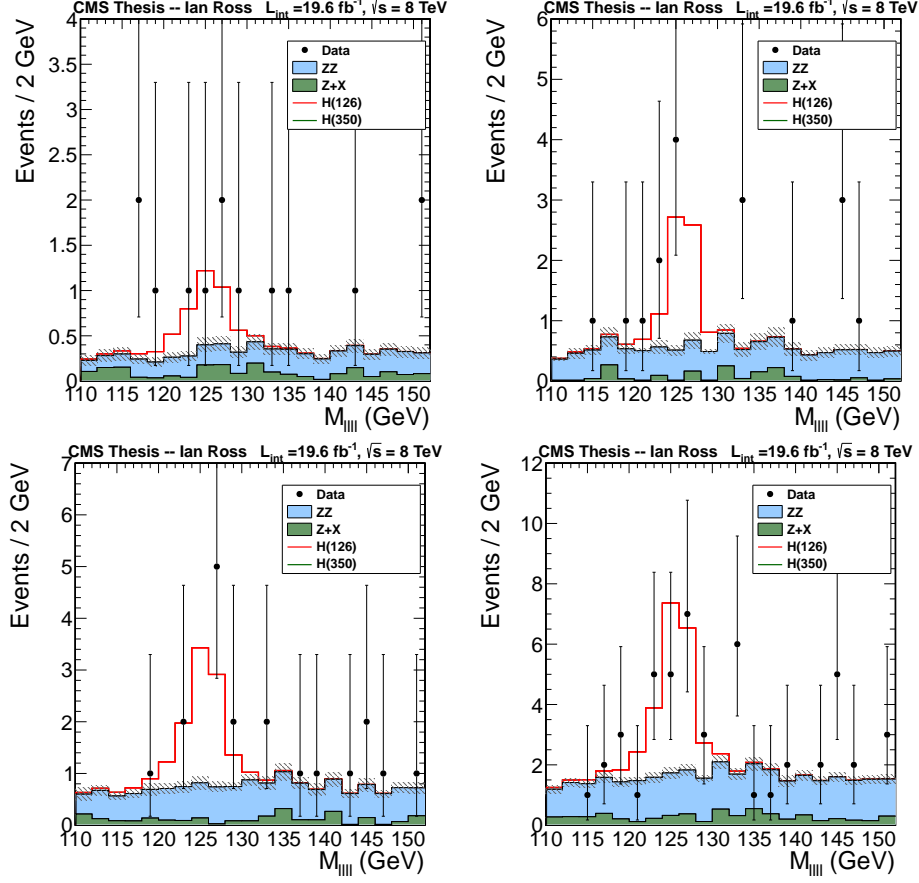


**Figure 8.9:** ZZ invariant mass including the low-mass ZZ\* analysis, zoomed to take a closer look at the excess. Pictured are the eeee,  $\mu\mu\mu\mu$ ,  $\mu\mu ee$ , and combined total results (upper left, upper right, lower left, and lower right respectively).

defined:

$$q_0 = -2 \ln \frac{L(0, \vec{\theta}_{s0}, \vec{\theta}_{b0})}{L(\hat{\mu}, \vec{\theta}_s, \vec{\theta}_b)} \quad (8.12)$$

Again, a pdf is constructed using pseudo-data and a background-only hypothesis, and a p-value for the observed test statistic is constructed:

$$p_\mu = P(q_0 \geq q_0^{obs}) \quad (8.13)$$

The corresponding significance of this p-value is taken from a normal one-sided hypothesis scenario. A full suite of tools has been developed in CMS to provide the statistical framework for the search for the Higgs boson [80].

A local p-value scan is done across the full mass range, Figure 8.11, with a maximum local significance of  $6.1\sigma$  observed at a Higgs mass of 126 GeV. 95% confidence level upper limits are calculated from 110 GeV up to 1 TeV, excluding a Standard Model Higgs boson in the ranges of 130 to 600 GeV.

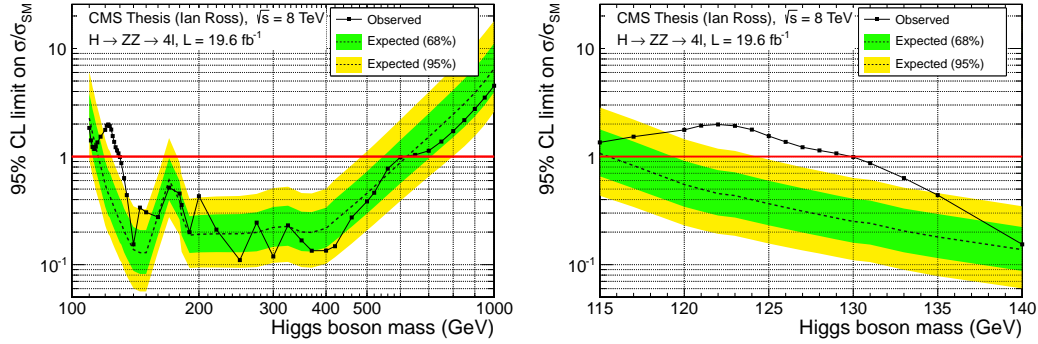


**Figure 8.10:** 95% CL Upper Limits on Standard Model Higgs production (full mass range on the left, with a low-mass scan on the right).

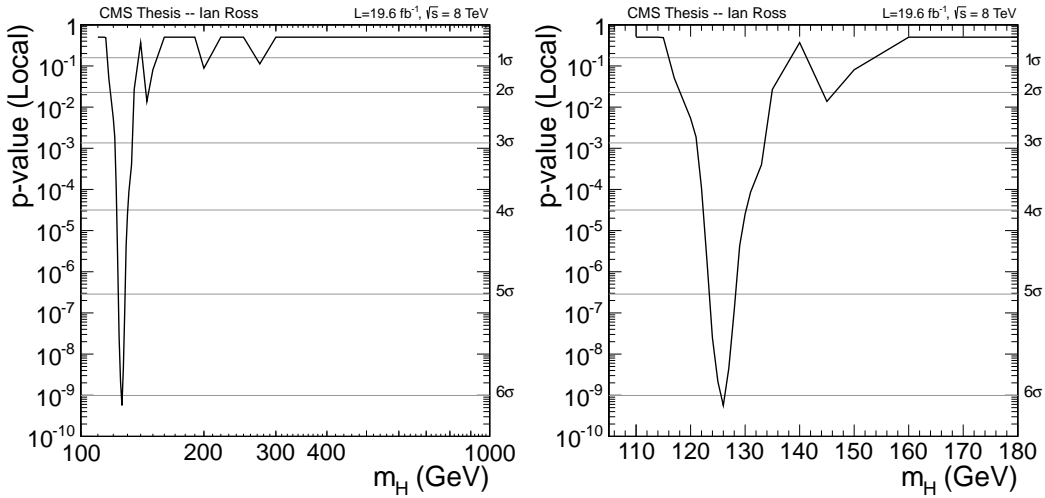


**Figure 8.11:** p-value scan for the full (left) and low (right) mass ranges.

### 8.3 Limits on anomalous triple gauge couplings

In order to set limits on the neutral triple gauge couplings, a binned counting procedure is followed. First, a  $3 \times 3$  grid of  $(f_i^Z, f_i^\gamma)$  Monte Carlo simulations are generated in SHERPA [52] and fully simulated and reconstructed. Because one of the major implications of the existence of anomalous couplings is an enhanced high-mass tail in  $M_{\ell\ell\ell\ell}$ , this variable is chosen as the discriminating variable. For each of the generated samples, the  $M_{\ell\ell\ell\ell}$  is plotted (using the same binning for all samples). Yields in intermediary points in the coupling space are interpolated bin-by-bin using a paraboloid fit to the existing samples, as Fermi's Golden Rule suggests a quadratic dependence on cross section. A likelihood for the null and alternative hypotheses is built, just like in the Higgs case outlined above. However, in the case of the triple gauge coupling limits, the CLs methodology is not used. Instead, a simple likelihood profiling is used, using Wilks' theorem to set the confidence levels. The CLs limit procedure is not used because, by definition, it will never exclude the null hypothesis. Given the presence of non-SM values of the couplings, the CLs limits give limits which have little utility.

The invariant mass of the four-lepton system contains little information about the sign of the couplings involved. The resulting likelihood scan shows this degeneracy (Figure 8.12), suggesting that only the size, but not the sign, of the couplings could be extracted from this information.

Though SHERPA is a leading-order generator, it has been shown (see Figure 8.13) that SHERPA generation (with up to one extra parton interaction) accurately reproduces the invariant mass kinematics of the NLO POWHEG generation. This gives confidence that the differences between LO and NLO in the discriminating variable ( $M_{\ell\ell\ell\ell}$ ) are slight, and SHERPA is an acceptable generator for the aTGC sample

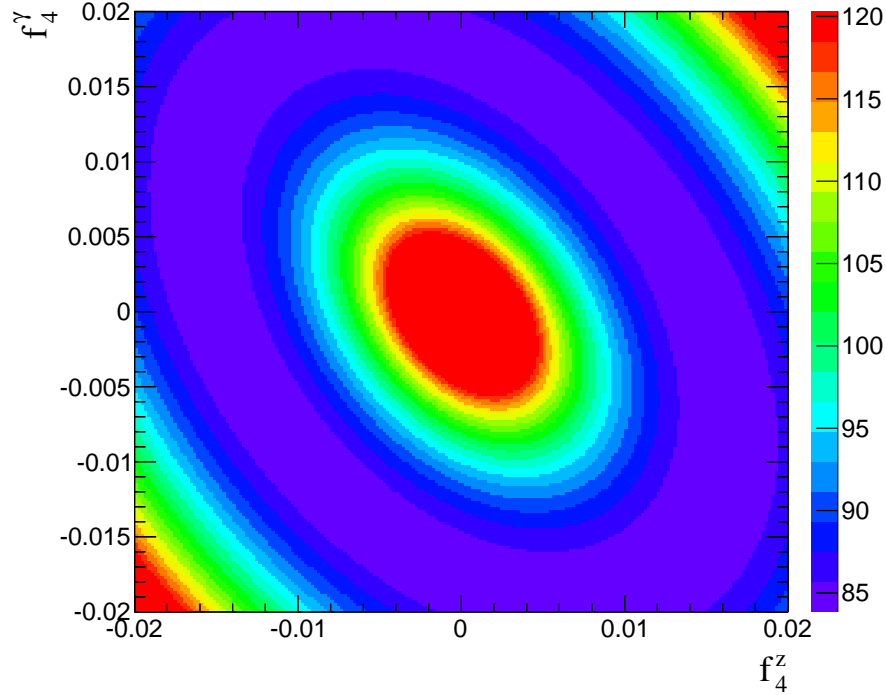


**Figure 8.12:** A qualitative likelihood scan of the  $(f_4^Z, f_4^\gamma)$  coupling space, with an aTGC signal injected. The degeneracy suggests that measurement of the sign of the couplings would be impossible using just the information from the four-lepton invariant mass.

generation.

No significant deviation from the Standard Model expectations are observed, and 95% Confidence Level upper limits are set using profile likelihood methodology. Limits are extracted for the two dimension  $(f_4^Z, f_4^\gamma)$  and  $(f_5^Z, f_5^\gamma)$  coupling spaces separately (with the other two couplings held to 0). Additionally, single-coupling limits are calculated by restricting the other couplings to 0. The two- and one-dimensional limits are depicted in Figure 8.14, and the one-dimensional limits are presented in Table 8.4.

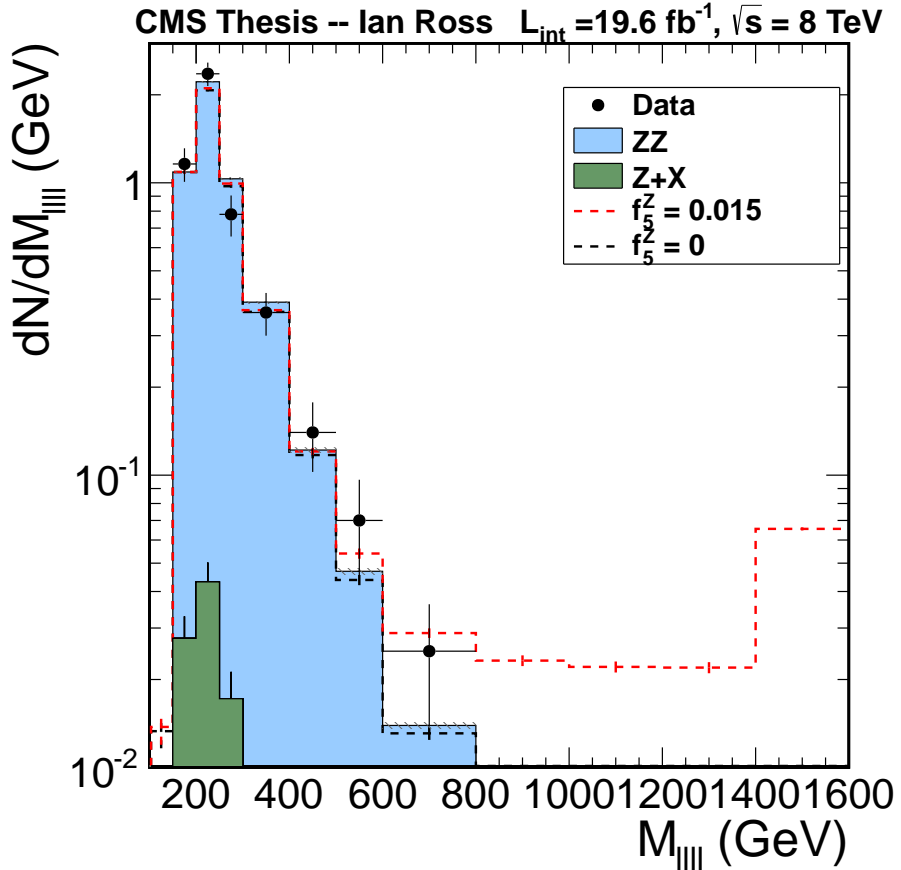


**Figure 8.13:** Comparison of the  $M_{\ell\ell\ell\ell}$  shape from Standard Model ZZ production by the LO generator SHERPA and the NLO POWHEG. Differences are slight, justifying the use of SHERPA in generating the aTGC Monte Carlo samples. The last bin contains the overflow of all higher  $M_{\ell\ell\ell\ell}$  values.

| i | $f_i^Z$                  | $f_i^\gamma$                  |
|---|--------------------------|-------------------------------|
| 4 | $-0.004 < f_4^Z < 0.004$ | $-0.005 < f_4^\gamma < 0.005$ |
| 5 | $-0.004 < f_5^Z < 0.004$ | $-0.005 < f_5^\gamma < 0.005$ |

**Table 8.4:** 1D limits on the neutral anomalous triple gauge couplings. Values are extracted by holding the other three neutral couplings to 0.

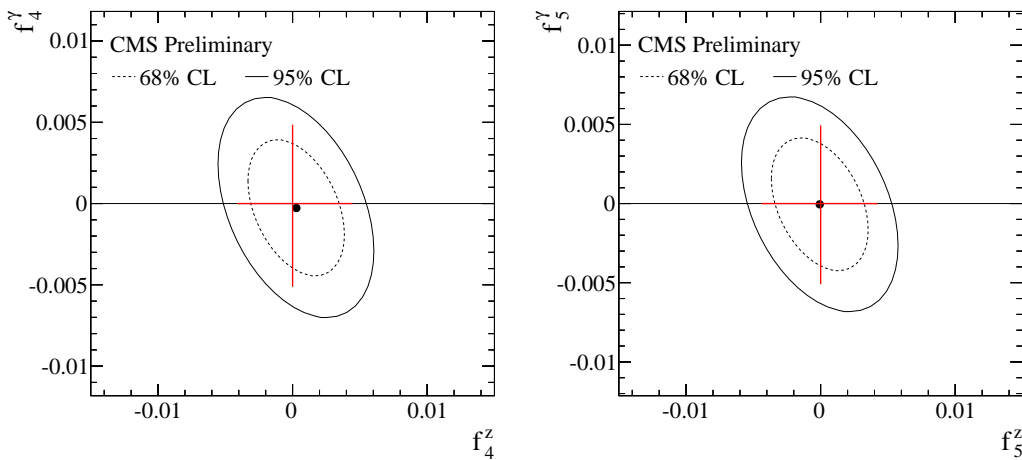


**Figure 8.14:** 2D limits on the neutral anomalous triple gauge couplings. The solid line represents the 95% confidence level on the 2D coupling, the dashed line represents the 68% confidence level, and the red lines represent the 95% confidence level limits (with the other couplings constrained to 0). The block dot represents the best-fit coupling values.

# Chapter 9

## Conclusions

### 9.1 Summary

A search for a Standard Model-like Higgs boson and anomalous neutral triple gauge couplings has been conducted at  $\sqrt{s} = 8 \text{ TeV}$ , using  $19.6 \text{ fb}^{-1}$  of pp collision data. The analysis benefits greatly from having a clean signature, allowing the usage of highly efficient reconstruction and selection algorithms while maintaining a low level of reducible background. This background was estimated using an entirely data-driven process, while the Standard Model ZZ production and Higgs signal processes were simulated using Monte Carlo methods.

The search for a Standard Model Higgs boson in the  $H \rightarrow ZZ \rightarrow \ell\ell\ell\ell$  final state resulted in a discovery of a new boson, with a  $6.1\sigma$  excess at a hypothesized Higgs mass of 126 GeV.

A search for the anomalous neutral triple gauge couplings  $f_4^{Z,\gamma}$  and  $f_5^{Z,\gamma}$  was conducted. The results are fully consistent with Standard Model behaviour, and 95% confidence level upper limits were set on the coupling strengths. The cross section for Standard Model  $ZZ \rightarrow \ell\ell\ell\ell$  production was measured from the collected data,

showing excellent agreement with theoretical calculations.

## 9.2 Future Outlook

Looking toward the future, the properties of the new boson, the differential cross sections of Standard Model ZZ production, and the continued search for anomalous triple gauge couplings will all benefit from the increased cross sections and luminosity expected from the LHC upgrades currently under way. Increases in center-of-mass energies from 8 TeV to 13 or 14 TeV along with a projected data collection of  $\sim 500 \text{ fb}^{-1}$  by the end of the decade will result in unprecedented precision in all  $(H \rightarrow)ZZ \rightarrow \ell\ell\ell\ell$  measurements.

The clean nature of the channel in addition to its fully reconstructed final state allow an excellent handle on doing further analysis of the newly discovered boson. An extension of the matrix element kinematic discriminant can be used to comb out the likely spin properties, while creating a separate category for events produced via Vector Boson Fusion (which includes a forward jet signature) can be used to measure the relative fermionic and vector boson couplings.

# Bibliography

- [1] Richard P Feynman. Mathematical formulation of the quantum theory of electromagnetic interaction. *Physical Review*, 80(3):440, 1950.
- [2] SL Glashow. Partial-symmetries of weak interactions. *Nuclear Physics*, 22(4):579–588, 1961.
- [3] Peter W. Higgs. Broken symmetries and the masses of gauge bosons. *Phys. Rev. Lett.*, 13:508–509, Oct 1964.
- [4] F. Englert and R. Brout. Broken symmetry and the mass of gauge vector mesons. *Phys. Rev. Lett.*, 13:321–323, Aug 1964.
- [5] G. S. Guralnik, C. R. Hagen, and T. W. B. Kibble. Global conservation laws and massless particles. *Phys. Rev. Lett.*, 13:585–587, Nov 1964.
- [6] The CMS Collaboration. Observation of a new boson at a mass of 125 GeV with the CMS experiment at the LHC. *Physics Letters B*, 716(1):30–61, September 2012.
- [7] The ATLAS Collaboration. Observation of a new particle in the search for the Standard Model Higgs boson with the ATLAS detector at the LHC. *Physics Letters B*, 716(1):1–29, September 2012.
- [8] John M Campbell, R Keith Ellis, and Ciaran Williams. Vector boson pair production at the LHC. *Journal of High Energy Physics*, 2011(7):18, July 2011.
- [9] Q.R. Ahmad et al. Direct evidence for neutrino flavor transformation from neutral current interactions in the Sudbury Neutrino Observatory. *Phys.Rev.Lett.*, 89:011301, 2002.

- [10] Y. Fukuda et al. Measurements of the solar neutrino flux from Super-Kamiokande's first 300 days. *Phys.Rev.Lett.*, 81:1158–1162, 1998.
- [11] F.P. An et al. Observation of electron-antineutrino disappearance at Daya Bay. *Phys.Rev.Lett.*, 108:171803, 2012.
- [12] K Hagiwara, R D Peccei, D Zeppenfeld, and K Hikasa. Probing the weak boson sector in  $e^+e^- \rightarrow W^+W^-$ . *Nuclear Physics B*, 282:253–307, 1987.
- [13] M Zralek and P C Christova. Composite z boson in the  $e^+e^- \rightarrow zz$  process. *Acta Phys. Pol. B*, 20(TPJU-89-4):739–749. 21 p, Jan 1989.
- [14] Ulrich Baur and D Rainwater. Probing neutral gauge boson self-interactions in ZZ production at hadron colliders. *Physical Review D*, 62(11):113011, 2000.
- [15] F J Hasert, H Faissner, W Krenz, J Von Krogh, D LANSKE, J MORFIN, K SCHULTZE, H WEERTS, G H Bertrand-Coremans, and J Lemonne. Search for elastic muon-neutrino electron scattering. *Physics Letters B*, 46(1):121–124, 1973.
- [16] The UA1 experient (G. Arnison et. al). Experimental observation of lepton pairs of invariant mass around 95 gev/c<sup>2</sup> at the cern sps collider. *Physics Letters B*, 126(5):398 – 410, 1983.
- [17] The L3 Collaboration The OPAL Collaboration The SLD Collaboration The LEP Electroweak Working Group The SLD Electroweak The ALEPH Collaboration, The DELPHI Collaboration and Heavy Flavour Groups. Precision electroweak measurements on the Z resonance.
- [18] The CDF Collaboration. Measurement of the forward-backward charge asymmetry of electron-positron pairs in  $\bar{p}p$  collisions at  $\sqrt{s} = 1.96$  TeV. *Phys. Rev. D*, 71:052002, Mar 2005.
- [19] V.M. Abazov et al. Measurement of the forward-backward charge asymmetry and extraction of  $\sin^2\theta_W^{eff}$  in  $p\bar{p} \rightarrow Z/\gamma + X \rightarrow e^+e^- + X$  events produced at  $\sqrt{s} = 1.96$  TeV. *Phys.Rev.Lett.*, 101:191801, 2008.
- [20] R. Barate et al. Measurement of the  $e^+e^- \rightarrow ZZ$  production cross-section at center-of-mass energies of 183-GeV and 189-GeV. *Phys.Lett.*, B469:287–302, 1999.

- [21] J. Abdallah et al. ZZ production in e+ e- interactions at  $sqrts = 183\text{-GeV}$  to  $209\text{-GeV}$ . *Eur.Phys.J.*, C30:447–466, 2003.
- [22] P. Achard et al. Z boson pair production at LEP. *Phys.Lett.*, B572:133–144, 2003.
- [23] G. Abbiendi et al. Z boson pair production in e+ e- collisions at  $sqrts = 183\text{-GeV}$  and  $189\text{-GeV}$ . *Phys.Lett.*, B476:256–272, 2000.
- [24] T. et al. Aaltonen. Measurement of  $zz$  production in leptonic final states at  $\sqrt{s}$  of 1.96 tev at cdf. *Phys. Rev. Lett.*, 108:101801, Mar 2012.
- [25] Victor Mukhamedovich Abazov et al. Measurement of the  $ZZ$  production cross section in  $p\bar{p}$  collisions at  $\sqrt{s} = 1.96$  TeV. *Phys.Rev.*, D84:011103, 2011.
- [26] R. Barate et al. Search for the standard model Higgs boson at LEP. *Phys.Lett.*, B565:61–75, 2003.
- [27] M W Grunewald. Precision electroweak measurements and constraints on the standard model. Technical Report arXiv:1012.2367. CERN-PH-EP-2010-095. FERMILAB-TM-2480-PPD. LEPEWWG-2010-01. TEVEWWG-2010-01. ALEPH-2010-001-PHYSICS-2010-001. CDF-Note-10338. DELPHI-DELPHI-2010-001-PHYS 952. L3-Note-2837. OPAL-PR-432. SLAC-PUB-14301, Dec 2010. Comments: 18 pages, Prepared from Contributions to the 2010 Summer Conferences.
- [28] CDF Group, D0 Collaborations, the Tevatron New Physics, and Higgs Working. Updated Combination of CDF and D0 Searches for Standard Model Higgs Boson Production with up to  $10.0 \text{ fb}^{-1}$  of Data. 2012.
- [29] Georges Aad et al. Measurements of Higgs boson production and couplings in diboson final states with the ATLAS detector at the LHC. 2013.
- [30] Combination of standard model Higgs boson searches and measurements of the properties of the new boson with a mass near 125 GeV. 2012.
- [31] S. Schael et al. *JHEP*, 0904:124, 2009.
- [32] J. Abdallah et al. *Eur. Phys. J. C*, 51:525, 2007.

- [33] G. Abbiendi et al. *Eur. Phys. J. C*, 32:303, 2003.
- [34] D. Abbaneo et al. A combination of preliminary electroweak measurements and constraints on the standard model. 2006.
- [35] M. Acciarri et al. *Phys. Lett. B*, 436:187, 1999.
- [36] V. Abazov et al. *Phys. Rev. Lett.*, 100:131801, 2008.
- [37] A. for the CDF Robson and D0 collaborations. Diboson physic at tevatron. 2012.
- [38] Measurement of the  $zz$  production cross section and limits on anomalous neutral triple gauge couplings in proton-proton collisions at  $\sqrt{s} = 7$  tev with the atlas detector. *Phys. Rev. Lett.*, 108:041804, 2012.
- [39] The ATLAS Collaboration. Measurement of  $ZZ$  production in pp collisions at  $\sqrt{s} = 7$  TeV and limits on anomalous  $ZZZ$  and  $ZZ$  couplings with the ATLAS detector. *Journal of High Energy Physics*, 2013(3):128, March 2013.
- [40] The CMS Collaboration. Measurement of the  $ZZ$  production cross section and search for anomalous couplings in  $2\ell 2\ell'$  final states in pp collisions at  $\sqrt{s} = 7$  TeV. *Journal of High Energy Physics*, 2013(1):63, January 2013.
- [41] Nicholas Metropolis and S. Ulam. The monte carlo method. *Journal of the American Statistical Association*, 44(247):pp. 335–341, 1949.
- [42] A.D. Martin, W.J. Stirling, R.S. Thorne, and G. Watt. Parton distributions for the LHC. *Eur.Phys.J.*, C63:189–285, 2009.
- [43] Jun Gao, Marco Guzzi, Joey Huston, Hung-Liang Lai, Zhao Li, et al. The CT10 NNLO Global Analysis of QCD. 2013.
- [44] Richard D. Ball, Valerio Bertone, Francesco Cerutti, Luigi Del Debbio, Stefano Forte, et al. Impact of Heavy Quark Masses on Parton Distributions and LHC Phenomenology. *Nucl.Phys.*, B849:296–363, 2011.
- [45] Richard D. Ball, Stefano Carrazza, Luigi Del Debbio, Stefano Forte, Jun Gao, et al. Parton Distribution Benchmarking with LHC Data. *JHEP*, 1304:125, 2013.

- [46] Bo Andersson, G. Gustafson, G. Ingelman, and T. Sjostrand. Parton Fragmentation and String Dynamics. *Phys.Rept.*, 97:31–145, 1983.
- [47] B. Webber. Parton shower monte carlo event generators. 6(12):10662, 2011.
- [48] Torbjorn Sjostrand, Stephen Mrenna, and Peter Z. Skands. PYTHIA 6.4 Physics and Manual. *JHEP*, 0605:026, 2006.
- [49] Tom Melia, Paolo Nason, Raoul Rontsch, and Giulia Zanderighi. W+W-, WZ and ZZ production in the POWHEG BOX. *JHEP*, 1111:078, 2011.
- [50] S Dittmaier, C Mariotti, G Passarino, R Tanaka, J Baglio, P Bolzoni, R Boughezal, O Brein, C Collins-Tooth, S Dawson, S Dean, A Denner, S Farrington, M Felcini, M Flechl, D de Florian, S Forte, M Grazzini, C Hackstein, T Hahn, R Harlander, T Hartonen, S Heinemeyer, J Huston, A Kalinowski, M Krmer, F Krauss, J S Lee, S Lehti, F Maltoni, K Mazumdar, S-O Moch, A Mck, M Mhlleitner, P Nason, C Neu, C Oleari, J Olsen, S Palmer, F Petriello, G Piacquadio, A Pilaftsis, C T Potter, I Puljak, J Qian, D Rebuzzi, L Reina, H Rzehak, M Schumacher, P Slavich, M Spira, F Stckli, R S Thorne, M Vazquez Acosta, T Vickey, A Vicini, D Wackerlo, M Warsinsky, M Weber, G Weiglein, C Weydert, J Yu, M Zaro, and T Zirke. *Handbook of LHC Higgs Cross Sections: 1. Inclusive Observables*. CERN, Geneva, 2011. Comments: 153 pages, 43 figures, to be submitted to CERN Report. Working Group web page: <https://twiki.cern.ch/twiki/bin/view/LHCPhysics/CrossSections>.
- [51] T. Bineth, N. Kauer, and P. Mertsch. Gluon-induced QCD corrections to  $pp \rightarrow ZZ \rightarrow \ell\bar{\ell}\ell'\bar{\ell}'$ . page 142, 2008.
- [52] T. Gleisberg, Stefan. Hoeche, F. Krauss, M. Schonherr, S. Schumann, et al. Event generation with SHERPA 1.1. *JHEP*, 0902:007, 2009.
- [53] Johan Alwall, Michel Herquet, Fabio Maltoni, Olivier Mattelaer, and Tim Stelzer. MadGraph 5 : Going Beyond. *JHEP*, 1106:128, 2011.
- [54] S. Agostinelli et al. GEANT4: A Simulation toolkit. *Nucl.Instrum.Meth.*, A506:250–303, 2003.
- [55] Paolo Azzurri. Track reconstruction performance in cms. *Nuclear Physics B - Proceedings Supplements*, 197(1):275 – 278, 2009. *jce:title*; 11th Topical Seminar on Innovative Particle and Radiation Detectors (IPRD08); *jce:title*.

- [56] Kenneth Rose. Deterministic annealing for clustering, compression, classification, regression, and related optimization problems. *Proceedings of the IEEE*, 86(11):2210–2239, 1998.
- [57] E. Chabanat and N. Estre. Deterministic annealing for vertex finding at CMS. pages 287–290, 2005.
- [58] Wolfram Erdmann. Vertex reconstruction at the cms experiment. In *Journal of Physics: Conference Series*, volume 110, page 092009. IOP Publishing, 2008.
- [59] Wolfgang Adam, R. Frhwirth, Are Strandlie, and T. Todor. Reconstruction of Electrons with the Gaussian-Sum Filter in the CMS Tracker at the LHC. 2005.
- [60] Particle-flow event reconstruction in cms and performance for jets, taus, and met. Technical Report CMS-PAS-PFT-09-001, CERN, 2009. Geneva, Apr 2009.
- [61] Matteo Cacciari, Gavin P. Salam, and Gregory Soyez. FastJet User Manual. *Eur.Phys.J.*, C72:1896, 2012.
- [62]
- [63] Byron P. Roe, Hai-Jun Yang, Ji Zhu, Yong Liu, Ion Stancu, et al. Boosted decision trees, an alternative to artificial neural networks. *Nucl.Instrum.Meth.*, A543:577–584, 2005.
- [64] Electron performance with  $19.6 \text{ fb}^{-1}$  of data collected at  $\sqrt{s} = 8 \text{ tev}$  with the cms detector. Mar 2013.
- [65] Properties of the higgs-like boson in the decay h to zz to 4l in pp collisions at sqrt s = 7 and 8 tev. Technical Report CMS-PAS-HIG-13-002, CERN, Geneva, 2013.
- [66] CMS Hgg Working Group. Updated measurements of the new higgs-like boson at 125 gev in the two photon decay channel. *CMS Analysis note*, AN-12-374.
- [67] Jan Therhaag. TMVA: Toolkit for multivariate data analysis. *AIP Conf.Proc.*, 1504:1013–1016, 2009.

- [68] Particle-flow commissioning with muons and electrons from j/psi and w events at 7 tev. Technical Report CMS-PAS-PFT-10-003, CERN, 2010. Geneva, 2010.
- [69] Jiyeon Han Arie Bodek. Improved rochester misalignment and muon scale corrections extracted for 2011a, 2011b cms data. *CMS Analysis note*, AN-12-298.
- [70] CMS HZZ4L Working Group. Updated results on the new boson discovered in the search for the standard model higgs boson in the h  $\rightarrow$  zz  $\rightarrow$  4l channel in pp collisions at s = 7 and 8 tev. *CMS Analysis note*, AN-12-367.
- [71] John M. Campbell and R.K. Ellis. {MCFM} for the tevatron and the {LHC}. *Nuclear Physics B - Proceedings Supplements*, 205206(0):10 – 15, 2010. *jce:title;Loops and Legs in Quantum Field Theory;jce:title;jce:subtitle;Proceedings of the 10th {DESY} Workshop on Elementary Particle Theory;jce:subtitle;*
- [72] Yanyan Gao, Andrei V. Gritsan, Zijin Guo, Kirill Melnikov, Markus Schulze, and Nhan V. Tran. Spin determination of single-produced resonances at hadron colliders. *Phys. Rev. D*, 81:075022, Apr 2010.
- [73] A. Drozdetskiy A. Korytov G. Mitselmakher M. Snowball P. Avery, M. Chen. A complete model of the four-lepton invariant mass distributions for h  $\rightarrow$  z z  $\rightarrow$  4l and z z  $\rightarrow$  4l events. *CMS Analysis note*, AN-11-202.
- [74] Stefano Goria, Giampiero Passarino, and Dario Rosco. The higgs-boson line-shape. *Nuclear Physics B*, 864(3):530 – 579, 2012.
- [75] Giampiero Passarino. Higgs Interference Effects in  $gg \rightarrow ZZ$  and their Uncertainty. *JHEP*, 1208:146, 2012.
- [76] S. Dittmaier et al. Handbook of LHC Higgs Cross Sections: 1. Inclusive Observables. 2011.
- [77] Sergey Alekhin, Simone Alioli, Richard D. Ball, Valerio Bertone, Johannes Blumlein, et al. The PDF4LHC Working Group Interim Report. 2011.
- [78] P. Hebda J. Hegeman D. Marlow N. Odell D. Stickland A. Zuranski A. Dabrowski, M. Grothe. Cms luminosity based on pixel cluster counting - summer 2012 update. *CMS Analysis note*, AN-12-174.

- [79] G. D'Agostini. A Multidimensional unfolding method based on Bayes' theorem. *Nucl.Instrum.Meth.*, A362:487–498, 1995.
- [80] Procedure for the lhc higgs boson search combination in summer 2011. Technical Report CMS-NOTE-2011-005. ATL-PHYS-PUB-2011-11, CERN, Geneva, Aug 2011.